Politecnico Di Milano
Department of Architecture, Built Environment and Construction Engineering

Bond durability of FRP-concrete and FRCM-masonry joints under the effect of environmental conditions

Doctoral Dissertation

By

Karrar Al-Lami

Supervisor:

Pierluigi Colombi

Co-supervisor

Tommaso D'Antino

July-2021

This page is left blank intentionally

Acknowledgment

In the beginning, the author would like to thank God for all His bounties, particularly health, knowledge, and patience

The author acknowledges Prof. Pierluigi Colombi and Prof. Tommaso D'Antino for their continuous scientific guidance and precious advice. Their valuable time and knowledge helped to finish this research successfully.

The author would like to acknowledge Prof. Reza Haghani from the Chalmers University of Technology for his contribution to the numerical model of the FRP.

The author also would like to show his sincere gratitude to the researchers and technicians with whom he cooperated. Their support and friendship were priceless. Particularly, Angelo Calabrese, Salam Al-Obaidi, Daniele Spinelli, Francesco Pillai. Furthermore, the author would like to extend his gratitude to the secretary and staff of the Architecture, Built environment, and Construction engineering department of the Polytechnic University of Milan for their great help.

This work could not be done without the Italian Ministry of Foreign Affairs and International Cooperation through MAECI scholarship, Ministry of Higher Education in Iraq, and department of Architecture, Built environment, and Construction Engineering of the Polytechnic University of Milan.

Finally, the author greatly appreciates the support of his family during his research journey.

Abstract

Fiber Reinforced Polymer (FRP) and Fiber Reinforced Cementitious Matrix (FRCM) have been increasingly adopted to repair and strengthen structural members in the last years. However, there is limited information available on their durability. The current research consists of two main parts aiming to investigate the performance of these two composites under hygrothermal and wet-dry conditions.

The first part was dedicated to studying the effect of the hygrothermal and wet-dry conditions on the CFRP-concrete joint and constituent materials (i.e., epoxy resin and CFRP strip). The hygrothermal condition was composed of continuous immersion in water at 38 ± 2 ^{o}C; however, the wet-dry condition comprised of 50 cycles with 6 hours of immersion in water followed by 18 hours of drying at 50 ^{o}C for each cycle. In total, eighty-two specimens were tested in this part of the research. Digital image correlation technique was also utilized to determine strain profile, cohesive material law, and subsequently, fracture energy of the CFRP-concrete interface. A two-dimensional finite element model was also utilized to calibrate the obtained cohesive material laws so they could be implemented in any numerical model aimed to evaluate the durability of the reinforced concrete structures externally bonded with CFRP. The results of this part of the research indicated some visible and mechanical changes in the performance of the epoxy resin. Furthermore, the failure mode of the CFRP-concrete joints exposed to wet-dry cycles was changed from a cohesive debonding in the concrete substrate to an adhesive debonding in the interface. However, the load-carrying capacity of the joint was not significantly influenced.

The second part of the research focused on investigating the effect of the wet-dry condition on the FRCM-masonry joints. Forty specimens were tested in this part of the dissertation. The specimens were prepared of three types of FRCM composites, which are made of carbon, PBO, and AR-glass textiles, and one type of Steel Reinforced Grout (SRG) composite. Both FRCM and SRG composites were externally bonded to masonry blocks. The specimens were exposed to 50 wet-dry cycles. Subsequently, the performance of the joints was evaluated using single-lap shear tests. The result of this part of the research implied some changes in the failure mode where it was changed for

some specimens from a debonding failure within the matrix-fiber interface to a debonding within the matrix-substrate interface. Furthermore, the average bond capacity of all composites was affected in different ranges. The last section of this part of the research was dedicated to analytically simulate the behavior of the FRCM-masonry joints using a trilinear cohesive material law. The model has accurately simulated the behavior of the carbon and PBO FRCM-masonry joints that developed a debonding failure in the matrix-fiber interface.

Sommario

Negli ultimi anni, i materiali compositi a matrice organica (FRP) ed inorganica (FRCM) sono stati adottati sempre più spesso per il consolidamento di strutture esistenti. Tuttavia, le informazioni disponibili sulla loro durabilità sono attualmente limitate. Allo stato attuale, la ricerca inerente questo tema è articolata in due filoni principali, mirati allo studio delle prestazioni di questi materiali in ambiente umido ed in condizioni cicliche umido-secco.

La prima parte di questa tesi si è concentrata sullo studio dell'effetto dei condizionamenti in ambiente umido e di cicli umido-secco sulle prestazioni di polimeri fibrorinforzati in carbonio (CFRP) e sull'aderenza tra CFRP e supporti in calcestruzzo. A tal fine sono stati sottoposti a condizionamento in ambiente umido campioni in calcestruzzo rinforzati con materiale composito, immergendoli in acqua a 38 ± 2 °C. Il trattamento in condizioni cicliche umido-secco invece comprendeva 50 cicli da 24 ore ciascuno, suddivisi in 6 ore di immersione in acqua seguite da 18 ore di essiccazione a 50 °C. Successivamente al condizionamento i campioni sono stati testati secondo la modalità di prova *single-lap shear test*. In totale, i campioni testati in questa parte della ricerca sono stati 82. La tecnica *digital image correlation* è stata utilizzata per determinare la deformazione del campione, la legge del materiale coesivo e, successivamente, l'energia di frattura dell'interfaccia CFRP-calcestruzzo. È stato inoltre utilizzato un modello bidimensionale agli elementi finiti per calibrare le leggi coesive dei materiali ottenute, in modo che potessero essere implementate in modelli numerici volti a valutare la durabilità di applicazioni di tipo CFRP su elementi strutturali in cemento armato. I risultati di questa parte della ricerca hanno indicato effetti dei condizionamenti sulle prestazioni della resina epossidica. Inoltre, è stata riscontrata un'alterazione nella modalità di crisi dei giunti CFRP-calcestruzzo esposti a cicli umido-secco, passata da una crisi per distacco distacco coesivo nel substrato di calcestruzzo a un distacco all'interfaccia composito-substrato. Tuttavia, la capacità aderente del giunto non è stata influenzata in modo significativo.

La seconda parte della ricerca si è concentrata sullo studio dell'effetto di cicli umido-secco sull'aderenza di compositi a matrice inorganica, applicati a supporti in muratura. Quaranta campioni sono stati testati in questa parte della tesi. Campioni in muratura di mattoni laterizi sono stati rinforzati esternamente con tre diversi compositi FRCM ed un composito

di tipo Steel Reinforced Grout (SRG). I compositi FRCM includevano rispettivamente un tessuto in fibra di carbonio, uno in fibra PBO ed uno in fibra di vetro resistente agli alcali (AR). I campioni sono stati esposti a 50 cicli umido-secco. Successivamente, le prestazioni dei giunti composito-muratura sono state valutate mediante prove di distacco *single-lap shear test*. L'evidenza sperimentale ha mostrato un'alterazione della modalità di crisi del rinforzo a seguito del condizionamento. In particolare, per alcuni campioni si è passati da una crisi di aderenza all'interfaccia matrice-tessuto, esibita da campioni non condizionati, a un distacco all'interfaccia tra matrice e substrato. Inoltre, la capacità media di aderenza di tutti i compositi analizzati è stata influenzata significativamente dal condizionamento. Infine, il comportamento dei giunti FRCM-muratura testati sperimentalmente è stato simulato analiticamente, utilizzando una legge materiale coesiva trilineare. Il modello sviluppato ha dimostrato di approssimare accuratamente il reale comportamento dei giunti in fibra di carbonio e PBO FRCM caratterizzati da una crisi di aderenza all'interfaccia matrice-tessuto.

Table of contents

List of Figures

List of Tables

Nomenclature

b_f	Width of the bonded CFRP strip
b^*	Width of a single fiber bundle (yarn)
CC	Continuous condensation
CFRP	Carbon Fiber Reinforced Polymer
CML	Cohesive Material Law
D	scalar variable utilized by Abaqus to define damage evolution law
d^*	Diameter of a single fiber bundle
DIC	Digital Image Correlation testing method
D_{ms}	Debonding failure in the matrix-substrate interface
D_{mf}	Debonding failure in the matrix-fiber interface
E_f	Elastic modulus of the fiber
FDZ	Fully Debonded Zone
FRCM	Fiber Reinforced Cementitious Matrix
FRP	Fiber Reinforced Polymer
f_r	Flexural strength of the matrix
f_f	Textile tensile strength
g	Global slip
G_F	Interfacial fracture energy
$\overline{G_F}$	Average interfacial fracture energy
GFRP	Glass Fiber Reinforced Polymer
k_1	slop of the elastic branch of the trilinear CML
k_2	slop of the softening branch of the trilinear CML
k_s	Interfacial elastic shear stiffness of the CFRP-concrete interface

K_{ss}	Ascending linear elastic part of the traction-separation law for the case of the normal component
K_{ss}	Ascending linear elastic part of the traction-separation law for the case of the shear component
ℓ	Bonded length of the FRCM composite
l_{eff}	Effective bond length
$MD_{mf}D_{ms}$	mixed debonding failure in the matrix-substrate interface and matrix-fiber Interface
$MD_{mf}R$	Mixed failure of debonding in the matrix-fiber interface followed by fiber rupture
p	Matrix–fiber contact perimeter of a single yarn
P^*	Peak-load value
$\overline{P^*}$	average peak load value
$P_b{}^*$	Peak load per unite width
$\overline{P_b}^*$	Average peak load per unite width
P_{cpty}	Load-carrying capacity of the CFRP-concrete joint
$\overline{P_{cpty}}$	Average load-carrying capacity of the CFRP-concrete joint
$P_{est}^{\varepsilon_{max}}$	Load-carrying capacity estimated based on the $\varepsilon_{\max}$
$P_{est}^{G_F}$	Load-carrying capacity estimated based on the G_F
P_{est}^{num}	Load-carrying capacity estimated based on the numerical model
PBO	Polyparaphenylene Benzobisoxazole
s	Interfacial slip
s_o	Equivalent interracial slip at τ_{max}
s_f	Equivalent interracial slip at τ_f
s_F	Slip measured at the free end of the FRCM composite

SFZ	Stress-Free Zone
SRG	Steel Reinforced Grout
STZ	Stress-Transfer Zone
t^*	Thickness of a single fiber bundle (yarn)
t_f	Thickness of the fiber
t_n	Traction in a direction purely normal to the interface
t_n^o	The peak value of the traction in a direction purely normal to the interface
$\bar{t}_n$	Normal traction components predicated by the elastic traction-separation behavior without damage consideration
t_s	Traction in the shear direction
t_s^o	Peak value of the traction in a purely shear direction
$\bar{t}_n$	Shear traction components predicated by the elastic traction-separation behavior without damage consideration
T_g	Glass transition temperature
TRC	Textile Reinforced Concrete
WD	Wet-dry cycles
WI	Water immersion
wt.%	weight percentage
ε_f	Ulltimate strain of textile fiber
ε_{max}	Maximum recorded strain on the CFRP strip or debonding strain
ε_{yy}	Longitudinal strain measured on the CFRP strip
ε^{num}	strain estimated numerically on the CFRP strip
δ_n	separation in a direction normal to the interface
δ_s	separation in a direction parallel to the interface

σ^*	Ultimate stress
$\bar{\sigma}^*$	Averge ultimate stress
σ_{deb}	Debonding stress
σ_f	Strength of the conditioned specimens
σ_{fu}	Strength of the reference or unconditioned specimens
τ	Interfacial shear stress
τ_{max}	Maximum interfacial shear stress
τ_f	Residual frictional shear stress

Chapter 1: Introduction

1.1 Problem statement

Repairing and strengthening structures have been increased because of the need to maintain and improve inherited buildings and infrastructure. Finding an efficient and economical technology is one of the challenges facing researchers these days. In the last few decades, Fiber Reinforced Polymer (FRP) and Fiber Reinforced Cementitious Matrix (FRCM) have been widely used for retrofitting concrete, steel, and masonry structures (Abid & Al-lami, 2018; Cabral-fonseca et al., 2018; T. D'Antino, Carloni, Sneed, & Pellegrino, 2014). One of the most common retrofitting techniques is externally bonded FRP and FRCM. Nonetheless, each one of these methods has its advantages and disadvantages.

FRP has been adopted in the application of aerospace and aircraft manufacturing for a long time. Nevertheless, FRP has gained greater attention in civil engineering applications in the last four decades (Bakis et al., 2003; Elarbi, 2011). FRP is known for its high strength-to-weight ratio, high stiffness-to-weight ratio, and high corrosive resistance. Nowadays, FRP is used to enhance the flexural strength of beams, slabs, and girders (Abid & Al-lami, 2018). It is also utilized to improve the shear and torsion strength of the beams. Columns are also strengthened by wrapping FRP around them to increase the confinement of the concrete core (Al-Khafaji, 2016). Despite its numerous advantages, FRP has some drawbacks, such as lack of ductility and serviceability (Kouris & Triantafillou, 2018; Micelli, Mazzotta, Leone, & Aiello, 2015; Pekmezci, Arabaci, & Ustundag, 2019). Moreover, organic resins used to prepare FRP composites can produce toxic fumes when exposed to fire. They may also lose their mechanical properties at a temperature close to their glass transition temperature, which is for epoxy resins commonly adopted in FRPs in the range of 45 °C to 82 °C (ACI Committee 440.2R-8, 2008; Ferrier, Rabinovitch, & Michel, 2016; J. P. Firmo, Correia, Pitta, Tiago, & Arruda, 2015).

FRCM was proposed as an alternative to FRP to overcome some drawbacks of the organic resin. Despite its lower mechanical properties, it is commonly used for retrofitting historical buildings made of masonry and concrete due to its compatibility with construction materials (Franzoni, Gentilini, Santandrea, Zanotto, & Carloni, 2017). It consists of fabric textile embedded in an inorganic matrix. The textile can be made of carbon, polyparaphenylene benzobisoxazole (PBO), Alkali-Resistant (AR) glass, or basalt (Al-Lami, D'Antino, & Colombi, 2020; T. D'Antino, Pisani, & Poggi, 2018; Koutas, Tetta, Bournas, & Triantafillou, 2019). The inorganic matrices can be cement-based, lime-based, or geopolymers (Bencardino, Condello, & Ashour, 2017; Donnini, 2019; Franzoni, Gentilini, Santandrea, & Carloni, 2018). When steel fibers are organized in cords and bonded with an inorganic matrix, the composite is referred to as Steel Reinforced Grout (SRG). In comparison with FRP, FRCM and SRG have better fire resistance and vapor permeability.

One of the reasons that hinder the wide adoption of FRP and FRCM composites is the incomplete information on the long-term performance of these composites. Therefore, more studies are needed to light the shadow about the durability and efficiency of these composites.

1.2 Advantages and Disadvantages of the FRP and FRCM composites

1.2.1 Advantages

For a long time, civil engineers have been searching for alternatives to steel to reduce the high cost of maintaining damaged structures due to corrosion. FRP and FRCM composites have proven their efficiency in repairing and strengthening deteriorated structures. The use of these composites has helped the contractors and companies to facilitate the installation process and reduce the application period. Moreover, they have high strength, high stiffness, low specific weight, non-corrosive nature, fatigue resistance, and excellent durability in different environments (Kong & Frangopol, 2003).

1.2.2 Disadvantages

Despite their numerous advantages over conventional steel, FRP and FRCM composites have several disadvantages that have to be considered cautiously, such as high initial cost of materials, uncommon design method, lack of long-term performance record. In addition, they are characterized by an elastic behavior; the lack of yielding can lead to less ductile structures unless this behavior is considered in the design stage (Elarbi, 2011). These materials are also vulnerable to be damaged from impact or vandalism. FRP is also susceptible to fire unless it was covered with some protective materials. Although FRP and FRCM are not corrosive materials, they are not immune to environmental effects and could suffer degradation after a long period of exposure to moisture and temperature. This disadvantage is relatively crucial because there is limited information available on the effect of the hygrothermal and wet-dry conditions on these composites and especially FRCM. Therefore, this research is intended to fill this gap.

1.3 Research objectives

Despite the numerous studies dedicated to investigating the mechanical properties of FRP and FRCM composites, there is limited information available on the durability of these composites. Out of the numerous environments to which a structure is expected to be exposed, moisture and temperature are the most common. Studies (Sen, 2015; Tuakta & Büyüköztürk, 2011) have also reported that hygrothermal (combined effect of moisture and temperature) and wet-dry conditions can have a crucial influence on the performance of the infrastructures externally reinforced with FRP. Furthermore, after an extensive review of the literature on FRCM composites, a lack of knowledge about the behavior of FRCM-masonry joints under the effect of wet-dry condition was noticed (Al-Lami et al., 2020). These reasons were the motivation to investigate the durability of the CFRP-concrete joints and FRCM-masonry joints under the effect of hygrothermal and wet-dry conditions. The current dissertation was dedicated to:

- Evaluate the effect of the hygrothermal condition on the mechanical properties of the epoxy resin and Carbon FRP (CFRP) composite.
- Investigate the effect of the hygrothermal condition on CFRP-concrete joints

- Investigate the effect of wet-dry cycles on CFRP-concrete joints
- Evaluate the effect of wet-dry cycles on FRCM-masonry joints
- Numerically and analytically investigate the performance of CFRP-concrete and FRCM-masonry joints, respectively.

1.4 Scope of the thesis

This dissertation is aiming to investigate the effect of hygrothermal and wet-dry condition on FRP and FRCM composites. It consists of two parts.

The first part is dedicated to studying the durability of CFRP consistent materials and bond durability of CFRP-concrete joints. Specimens are exposed to two environmental conditions, namely hygrothermal and wet-dry. The former condition involves complete immersion of specimens in water at 38±2ºC for 500 h, 1000 h, and 1500 h. The latter condition includes exposing CFRP-concrete joints to 50 wet-dry cycles. Four types of tests are performed, namely uniaxial test on epoxy resin specimens, uniaxial test on CFRP coupons, pull-off test, and direct shear single-lap test. In total, 84 tests are performed in this part of the research. Furthermore, digital image correlation technique is utilized to determine the strain profile along with the CFRP-concrete interface and the effect of the conditioning environment on the bond characteristics. Subsequently, the performance of the CFRP-concrete joint is simulated numerically.

The second part is dedicated to investigating the durability of FRCM and SRG composites. It includes 40 specimens of three types of FRCM composites (carbon, PBO, and glass) and one SRG composite type. They are bonded to masonry blocks. The specimens are exposed to 50 cycles of wet-dry. After that, direct shear single-lap tests are performed to evaluate the bond degradation between the composite and masonry substrate. Finally, the behavior of the FRCM-masonry joint is analytically modeled using a trilinear bond-slip model

1.5 Thesis outline

The current thesis consists of five chapters. Most of the results and information presented were either published in scientific journals or under review.

The second chapter presents an extensive review of the durability of the FRP, FRCM, and SRG composites. It is divided into two sections. The first section focuses on the durability of the epoxy resin, FRP composite, and the bond between FRP composite and concrete substrate. Since the current research is intended to investigate the effect of the hygrothermal and wet-dry conditions on the bond durability of the CFRP composites, most of the reviewed literature focuses on the effect of moisture and temperature on the FRP. The second section of the chapter focuses on the durability of inorganic matrices, composites, and bonds between FRCM composites and different substrates. Because the available information on the effect of the moisture and temperature on the durability of FRCM and SRG composites is quite limited, the presented literature is expanded to include the effect of other conditions such as alkaline, saline, and freeze-thaw conditions. Furthermore, the literature results are compared to have a deep understanding of the durability of FRCM composites.

The third chapter is dedicated to evaluating the effect of the hygrothermal condition on the durability of the epoxy resin, CFRP composite, and bond between CFRP composite and concrete substrate. Furthermore, the effect of wet-dry condition on the CFRP-concrete joint is evaluated in this chapter. A full description of the utilized materials is provided. Conditioning environments and mechanical characterization of the constituent materials are also discussed. The effect of the hygrothermal condition on the constituent materials is discussed and presented. Methods utilized to investigate the bond durability of the CFRP-concrete joint are also discussed. A detailed discussion about Digital Image Correlation (DIC) technique is presented. In addition, the effect of the hygrothermal condition and wet-dry cycles on the fracture energy of the CFRP-concrete joint is evaluated. The last part of this chapter is dedicated to numerically simulate the behavior of the CFRP-concrete joint under the effect of hygrothermal and wet-dry conditions using the commercial software, Abaqus. A full description of the model geometry, material properties, load condition, and boundary conditions are presented. The method utilized to

model the contact interface between the CFRP strip and concrete prism is explained in detail. After that, the result of the numerical model is compared with the experimental result in terms of load-slip response, load-carrying capacity, debonding strain, and strain distribution on the CFRP strip.

The fourth chapter concentrates on the effect of the wet-dry cycles on the bond durability of the FRCM and SRG composites. A full description of the utilized materials is provided. Since there is no standard method to perform wet-dry cycles, this chapter presents the criteria utilized to propose that condition. The effect of the wet-dry cycles on specimen shape (i.e., deformation of the specimens), failure mode, and bond capacity is presented and discussed in detail. In the last part of the chapter, the behavior of the FRCM-concrete joint is modeled using a trilinear bond-slip model (Tommaso D'Antino, Colombi, Carloni, & Sneed, 2018). A whole discussion of the model is provided. The method utilized to evaluate the effective bond length is also presented. Subsequently, the analytically estimated load-slip response is compared to the experimentally measured response.

The last chapter (conclusion) presents the achieved objectives of the research. Besides, the main findings of the thesis are highlighted. Finally, suggestions for future research are proposed.

Chapter 2: State of Art

2.1 Introduction

Externally bonded fiber-reinforced polymer (FRP) composites have become a valid solution for strengthening and retrofitting existing reinforced concrete (RC) structures due to their advanced mechanical properties (Abid & Al-lami, 2018; Pendhari, Kant, & Desai, 2008). Although FRP can sufficiently enhance the strength of the unreinforced masonry structures, some drawbacks hindered its comprehensive implementation for retrofitting historic masonry structures, such as low vapor permeability and irreversibility (difficulty to detach FRP from masonry substrate) (Kouris & Triantafillou, 2018). Since FRP has been extensively used to strengthen RC structures, the current research has been dedicated to studying the durability of CFRP-concrete joints and constituent materials.

Durability is defined as the capacity to resist cracking, oxidation, chemical degradation, and delamination during a specific duration under a specific load and environmental conditions (Karbhari et al., 2003). Like any bonded assembly, the durability performance of externally bonded FRP is highly dependent on the resistance of the constituent materials and the bond established between FRP and substrate. Several factors can affect FRP-concrete joints, such as concrete surface preparation, workmanship relating to its installation, the severity of environmental conditions, and others (Abid & Al-lami, 2018; Sen, 2015; Yalim, Kalayci, & Mirmiran, 2008). The concrete surface to which FRP is bonded should be in good condition and relatively rough to provide good bonding strength (Serbescu, Guadagnini, & Pilakoutas, 2013). Both sandblasts and mechanical abrading can be used to improve surface roughness. Moreover, the system should be installed by workers who have enough knowledge adequately trained. Combined effects of various environmental conditions can also seriously affect the bond performance leading to premature failure. Multiple studies have reported the effect of various environmental conditions on the durability of the bond between FRP and concrete focusing mainly on freeze-thaw cycles (Choi, Gartner, Etten, Hamilton, & Douglas, 2012; Lopez de Murphy & Krishnawamy, 2006), alkaline environments (Cromwell, Harries, & Shahrooz, 2011; Uomoto, Mutsuyoshi, Katsuki, & Misra, 2002), salt and

moisture (M. A. G. Silva & Biscaia, 2008), dry heat (Ferrier et al., 2016; J. P. Firmo et al., 2015; Robert, Wang, Cousin, & Benmokrane, 2010), and moisture (Frigione, Aiello, & Naddeo, 2006; A. Zhou, Büyüköztürk, & Lau, 2017). However, some studies (Sen, 2015; Tuakta & Büyüköztürk, 2011) have reported the significant effect of hygrothermal and wet-dry conditions on the bond performance of the CFRP-concrete joint; consequently, they were intensively studies in this research.

2.2 Durability of FRP composite

2.2.1 Effect of temperature and moisture on epoxy resin

The effect of the hygrothermal condition on the epoxy resin can be attributed to series of interrelated actions of the temperature and moisture. Elevated temperature can accelerate the degradation processes that can occur in the polymers, such as oxidation, mechanical creeps, and fatigue. However, moisture absorption can alter the physical, chemical, and mechanical properties of epoxy resin. Some of these changes can be reversed after drying such plasticization (Tuakta & Büyüköztürk, 2011), which could increase the free volume in the cross-link chain and subsequently reduce the glass transition temperature (T_g). Other are irreversible changes such as hydrolysis, cracking and crazing (Maljaee, Ghiassi, & Lourenço, 2017).

Numerous studies have been performed to investigate the effect of thermal exposure on the mechanical properties of different types of adhesive. However, most of these studies were focused on the hot-curing epoxy resin (i.e., cured at elevated temperature with artificial heating). The information available on the effect of the temperature on cold-curing epoxy resin, which is mainly used in civil engineering applications, is limited (Savvilotidou, Vassilopoulos, Frigione, & Keller, 2017). Results indicated that change in the mechanical properties depends on the type of the polymeric resin, exposure temperature, types of the applied stress, and exposure period (Cabral-fonseca et al., 2018; Savvilotidou et al., 2017). Ferrier et al. (Ferrier, Rabinovitch, & Michel, 2015) investigated the effect of low temperature (down to -30^{o}C) and high temperature (up to 100^{o}C) on the mechanical properties of the epoxy resin. Tensile test was performed based on the ISO527 standard (International Standard Organaziation ISO & 527-1, 2012). T_g of the investigated resins was ranging between 76^{o}C and 90^{o}C. Test results showed that the

tensile strength of the resin was significantly decreased at a temperature of 50 ^{o}C. Moreover, at temperatures of 80 ^{o}C and 100 ^{o}C, the resins lost their stiffness. The results also indicated a significant reduction in the tensile strength of the resins at a low temperature of -20 ^{o}C and -30 ^{o}C, respectively. Silva et al. (P. Silva et al., 2016) investigated the effect of the thermal cycles (ranging between -15 ^{o}C and 60 ^{o}C) on the commercial epoxy adhesive used for the FRP strengthening of the concrete members. Rustles indicated that thermal cycles could stimulate post-curing of the epoxy leading to an increase in the tensile strength by 31%, elastic modulus by 15%. In addition, T_g was increased from 44 ^{o}C to 59 ^{o}C.

Moisture diffusion into the organic polymer can cause reversible changes (plasticization and swelling), vanishing after drying, and irreversible changes (hydrolysis and cracking) (Cabral-fonseca et al., 2018; Sen, 2015; Shrestha, Ueda, & Zhang, 2015). These changes can affect the thermoplastic, chemical, and mechanical properties of the resin. The changes in the properties of the epoxy resin are often linked to the moisture content ratio (Maljaee, Ghiassi, Lourenço, & Oliveira, 2016). Several studies have investigated moisture diffusion in epoxy. Moreover, some models were proposed to simulate water absorption by the molecules (Grave, Mcewan, & Pethrick, 1998; Soles & Yee, 2000).

Water can be classified into free water within the free volume (voids) of the epoxy and combined water with an epoxy network by hydrogen bonds (Maxwell & Pethrick, 1983). According to some studies (Adamson, 1980; VanLandingham, Eduljee, & Gillespie, 1999), free water molecules do not cause dimensional changes in the polymer. Nevertheless, the combined water (bound water) can disrupt the inter-chain hydrogen bonding causing polymer swelling and plasticization.

Zhou and Lucas (J. Zhou & Lucas, 1999a) investigated water interaction with three types of epoxy resins. It was concluded that there are two types of the combined water (bound water) based on bond complexity and strength. Type I bound water works as a plasticizer. This type has lower activation energy and can be removed easily. It is also responsible for the reversible degradation mechanism. Nonetheless, type II bound water has higher activation energy; thus, it is more difficult to be removed. This type of water is responsible for the irreversible degradation mechanism. The effect of the hygrothermal

environment on the T_g of the epoxy resin was also investigated by the authors (J. Zhou & Lucas, 1999b). It was concluded that Type I and Type II bound water can affect T_g differently. Type I bound water can interrupt initial Van der Waals inter-chain force and hydrogen bond, leading to an increase in chain segment mobility; consequently, decreasing T_g. However, Type II bound water can form a secondary crosslink network leading to an increase in T_g in the water-saturated epoxy resin. Consequently, the change in the T_g of a specific epoxy resin can be attributed to the conflicting effect of these two types of waters.

The reduction in the T_g and the deterioration in the mechanical properties of the epoxy resin due to the moisture have been investigated by several researchers, as summarized in Table 2-1. It can be reported that exposure to moisture can increase the ductility and reduce the elastic modulus and tensile strength of the epoxy resin. However, using different types of epoxies and adopting different aging conditions with various temperatures as a means of accelerating diffusion mechanism make it challenging to run a comprehensive comparison.

Table 2-1: Summary of the studies on the durability of epoxy resin

Authors	Materials	Exposure conditions	Conclusions
Maljaee et al. (Maljaee et al., 2017)	Epoxy resin	• WI at 20 °C; 9 months • Hygrothermal cycles: 90% RH; 2 h at 10°C and 2 h at 50°C; 6 h/cycle; 960 cycles	• IW: T_g decreases with time until 7 months, followed by a slight increase • Cycles: T_g shows an initial increment, followed by a plateau
Maljaee et al. (Maljaee et al., 2016)	Epoxy resin	• Hygrothermal cycles: 2 h at 10°C 60% RH and 2 h at 50°C 90% RH; 6 h/cycle; 960 cycles	• Maximum degradation occurred within the first 120 cycle • Tensile strength and elastic modulus were reduced by 26% and 18% after 960 cycle
Shrestha et al (Shrestha et al., 2015)	3 types of epoxies resin	• WI at 20°C; 2-24 months • WD for 3-18 months: 7 days WI at 20 °C and 4 days dry at 20 °C & (50-55%) RH	• Specimens were dried for more than a month before measuring the T_g; thus, the reduction in the T_g was less than 5% after 24 months of conditioning. • IW & WD: no clear trend in the tensile strength and elastic modulus. They were fluctuating along the exposure periods. • WD: no reduction in the tensile strength while elastic modulus reduced by 4, 6, 11% depending on the epoxy type.
Blackburn et al. (Blackburn, Tatar, Douglas, & Hamilton, 2015)	6 types of epoxies resin	• WI at 30 °C and 60 °C; 12 weeks • CC: 100% RH at 30 °C and 60 °C; 8 weeks	• Higher rate of water absorption at 60 °C than at 30 °C • Insignificant variation in Tg for 30 °C; • Increase of Tg for 60 °C (post-cure effect)
Goglio and Rezaei (Goglio & Rezaei, 2014)	Epoxy resin	• CC: 100% RH at 50 °C; 5 weeks	• Decrease in tensile properties, with 75% reduction in the strength and 20% in the elastic modulus
Yang et al. (Yang, Xian, & Karbhari, 2008)	Epoxy resin	• WI at 23 °C, 38 °C, and 60 °C; 24 months	• A slight decrease in Tg at 23 °C (plasticization) • More expressive decrease in Tg at 38 °C and 60 °C • Significant reduction in tensile properties, more pronounced at the higher temperature; after 24 months: reduction in tensile strength of 43%, 44%, 69% and reduction in elastic modulus of 36%, 40%, 68%, at 23 °C, 38 °C and 60 °C

Silva et al. (P. Silva et al., 2016)	Epoxy resin	• WI at 20 °C; 480 days	• Decrease of Tg • Significant reduction of tensile properties: 38% in tensile strength and 53% in elastic modulus
Lettieri and Frigione (Lettieri & Frigione, 2012)	Epoxy resin	• CC: 55%, 75% and 100% RH at 23 °C; 28 days • WI at 23 °C; 28 days	• Exposure time was insufficient to achieve saturation • Decrease of Tg (plasticization) • Reduction in flexural modulus: 8% (CC55), 5% (CC75), 13% (CC100) and 15% (IW)
Frigione et al (Frigione et al., 2006)	3 types of epoxy resin	• WI at 23 °C; 28 days and until saturation	• Short immersion time: decrease in Tg (plasticization) followed by an increase at longer immersion time (additional cross-linking) • Flexural modulus decreases at the initial stages of immersion followed by a slight increase at longer immersion times, reaching a constant value after one month • Reduction at the saturated stage in flexural strength (between 9% and 18%) and in flexural modulus (between 17% and 36%)
Cabral-Fonseca et al. (Cabral-fonseca et al., 2018)	3 types of epoxy resin	• WI at 23 °C, 40 °C, and 60 °C; 18 months • CC: 100% RH at 40 °C; 18 months	• Different behavior of each adhesive • General reduction of Tg • Decrease in tensile properties for one of the adhesives: reduction in tensile strength (44%, 39%, and 60%) and in elastic modulus (48%, 15%, and 58%) at 23 °C, 40 °C and 60 °C • Decrease in flexural properties for one of the adhesives: reduction in flexural strength (41%, 36%, and 60%) and in flexural modulus (10%, 11%, and 45%) at 23 °C, 40 °C and 60 °C
Lin and Chen (Lin & Chen, 2005)	Epoxy resin	• CC: 85% RH at 85 °C; until saturation	• After moisture absorption: reduction of the tensile strength (30%) and elastic modulus (29%) • After drying: recover the strength and the elastic modulus to 90%

Sciolti et al. (Stefania, Mariaenrica, & Antonietta, 2010)	3 types of epoxy resin	• WI at 23°C for 27, 29, and 31 weeks	• Reduction in the Tg depending on the epoxy type • Reduction in the tensile strength and elastic modules with various values depending on the epoxy type
Benzarti et al. (Benzarti, Chataigner, Quiertant, Marty, & Aubagnac, 2011)	2 types of epoxy resin	• CC: 95% RH at 40°C; 265 and 206 days	• Tg for one of the epoxies was decreased. However, it is increased for the other one. • Reduction in the tensile strength and elastic modulus.
Au et al., (Au, Büyüköztürk, Asce, Büyüköztürk, & Asce, 2006)	2 types of epoxies	• WI in 23 and 50 °C for 4 and 8 weeks	• Reduction in the value of the T_g ranging (3-7°C) depending on the exposure conditions and epoxy type. • Reduction in the tensile strength and elastic modulus.

WI: water immersion, CC: continuous condensation, WD: wet-dry cycles

2.2.2 Effect of temperature and moisture on FRP

The effect of the temperature on the FRP composite may vary depending on the constituent materials of the composite, such as the type of fiber and matrix. Generally, exposure to low temperature (sub-zero temperature) can cause matrix hardening, matrix micro-cracking, and fiber-matrix bond degradation (Karbhari et al., 2003). Nonetheless, exposure to a temperature higher than the curing temperature can stimulate the post-curing effect first and after that thermal degradation (Karbhari et al., 2003). Kabhari et al. (Karbhari, Rivera, & Zhang, 2002) investigated the effect of the low temperature (-10 ^{o}C) and freeze-thaw cycles (between -10 ^{o}C and 23 ^{o}C) in the presence of the moisture on the mechanical properties of the Glass FRP (GFRP). Results showed that though the low temperature can cause matrix stiffening and a slight increase in the strength and stiffness, exposure to freeze-thaw cycles can accumulate the damage leading to a reduction in the performance. Firmo et al. (João P. Firmo, Correia, & Bisby, 2015) reported that exposing FRP composites to an elevated temperature close to their T_g can reduce their elastic modulus and tensile strength. In addition, it can cause a chemical decomposition of the polymeric matrix, which in its turn can accelerate the other degradations mechanism such as water and chemical diffusion. Table 2-2 reports the finding of some other studies on the effect of the temperature on the FRP composites.

During their lifetime, FRP composites are also exposed to moisture from the surrounding environment. Theoretically, moisture can disrupt the fiber, matrix, and fiber-matrix interface. Moisture can firstly affect the polymer matrix itself by inducing reversible and irreversible changes which can affect properties of the polymer structure, as discussed in section 2.2.1. Moisture can also affect the fibers especially the ones made of glass by etching the fiber surface causing flaws that can reduce the strength of the fibers (Cabral-fonseca et al., 2018). Nonetheless, studies have shown that moisture does not have a significant effect on carbon fiber (Saadatmanesh, Tavakkolizadeh, & Mostofinejad, 2010; Stefania et al., 2010). On the fiber-matrix level, the moisture-wicking phenomenon, which is the movement of the liquid through tiny spaces within the fabric due to the molecular forces between the liquid and the fabric's internal surfaces, allows moisture to move through the small voids to settle along the fiber-matrix interface causing deleterious

effects on the fiber-matrix bond (Cabral-fonseca et al., 2018). Matrix cracking can exacerbate the situation by providing more space for moisture absorption and movement. Moreover, epoxy swelling induced by moisture absorption can cause internal stresses leading to fiber debonding from the matrix.

Experimental studies have reported contradicted results on the effect of moisture on the FRP. Some studies have observed a decrease in the mechanical properties of the FRP (Abanilla, Karbhari, & Li, 2006; Abanilla, Li, & Karbhari, 2005). However, others detected an increase in the stiffness (Stefania et al., 2010) or even an insignificant effect (Kafodya, Xian, & Li, 2015). Some researchers assumed that since moisture uptake can usually affect matrix's properties, matrix-dominated properties such as interlaminar shear strength are more sensitive to moisture-induced degradation than other properties (Ramirez, Carlsson, & Acha, 2008; Sethi & Ray, 2015; Woo & Piggott, 1987). Although there are reasonable numbers of researchers who have investigated the effect of moisture on the FRP, they failed to identify a direct correlation between moisture content (Helbling, Abanilla, Lee, & Karbhari, 2006) and degradation level. Table 2-2 presents some of the studies dedicated to investigating the effect of moisture on the FRP.

In conclusion, moisture absorption by FRP is influenced by numerous factors such as type of fiber, type of matrix, FRP condition (cracked, uncracked), and environmental conditions (thermal effect).

Table 2-2: Effect of temperature and moisture on the FRP

Authors	Materials	Exposure conditions	Conclusions
Cromwell et al. (Cromwell et al., 2011).	Prefabricated CFRP strips and in-situ prepared CFRP and GFRP sheets	• Dry heating at 60 ^{o}C for 1000 and 3000 h • CC: 100% RH at 38 °C; 10000 h	• Regarding the first condition, results indicated an increase in the tensile strength and elastic modulus of CFRP strips (5% and 6%, respectively). Similarly, for CFRP fabric, tensile strength and elastic modulus were increased by 19% and 18%, respectively. However, for the GRFP fabric, its strength was reduced by 6% since the exposed temperature was greater than its T_g (45 ^{o}C). it is worth noting that T_g for the CFRP fabric was 52 ^{o}C. • Regarding the second condition, tensile strength and elastic modulus of the CFRP strips were increased by 15 % and 6%, respectively. Similarly, for the CFRP fabric, its tensile strength and elastic modulus were slightly increased by 8%and 5%, respectively. However, regarding the GFRP fabric, its strength was reduced by 3%; yet its elastic modulus was not affected.
Hawileh et al. (Hawileh, Abu-Obeidah, Abdalla, & Al-Tamimi, 2015)	In-situ prepared CFRP and GFRP	• Elevated temperature of 25, 100, 150, 200, 250, and 300 ^{o}C for 45 minutes then left to cool down for 24 h before testing	• Elastic modulus and tensile strength of the CFRP and GFRP coupons were continuously decreased as the temperature increased. • At the temperature of 100 ^{o}C, the elastic modulus and tensile strength of the CFRP sheets were reduced by 6% and 14%, respectively. However, the elastic modulus and tensile strength of the GFRP sheets were reduced by 7% and 10%, respectively.
Benzarti et al. (Benzarti, Chataigner, et al., 2011)	Pre-cured CFRP	• CC: 95% RH at 40 °C; 4 months	• Aging conditions did have a significant effect on the CFRP stiffness
Maljaee et al. (Maljaee et al., 2016)	In-situ prepared GFRP	• Hygrothermal cycles: 2 h at 10°C 60% RH and 2 h at 50°C 90% RH; 6 h/cycle; 960 cycles	• Most of the degradation occurs within the first 240 cycle • Tensile strength was reduced by 21%. However, the elastic was not affected by the aging conditions.

Abanilla and Karbhari (Abanilla et al., 2005)	CFRP fabric (six layers)	• WI at 23 °C, 38 °C, and 60 °C; 100 weeks	• Coefficient of diffusion increases with temperature • Deterioration in tensile properties with time and temperature: tensile strength reduction (32%, 39% and 42%) and elastic modulus reduction (12%, 22% and 27%) at 23 °C, 38 °C and 60 °C • Degradation in the flexural properties with time and temperature: flexural strength decrement (31%,40%, and 54%) and flexural modulus (9%, 16%, and 28%) at 23 °C, 38 °C and 60 °C • Tg decreased as a function of time and temperature (highest degradation at the highest temperature)
Abanilla et al. (Abanilla et al., 2006)	CFRP fabric (six layers)	• WI at 23 °C, 38 °C, and 60 °C; 100 weeks	• Reduction in short beam shear strength with time and temperature (26%, 46% and 50% at 23 °C,38 °C, and 60 °C) • Decreased in in-plane shear strength with time and temperature (18%, 31% and 48% at 23 °C, 38°C, and 60 °C) • Increase in the interlaminar fracture toughness with time
Sciolti et al. (Stefania et al., 2010)	In-situ prepared CFRP and GFRP	• WI at 23 °C; 29 weeks	• CFRP: decrease in the tensile strength (30%) and increase in the elastic modulus (32%) • GFRP: reduction of the tensile strength (31%) and increase of elastic modulus (8%)
Kafodya et al. (Kafodya et al., 2015)	Prefabricated CFRP	• WI at 25 °C; 20 weeks • Strained (30% and 50%) and unstrained samples in bending	• Moisture increase linearly with time. • No effects on tensile strength and modulus • Obvious deterioration in short beam strength (22%, 28% and 29% at 0%, 30% and 50% strain)

2.2.3 Effect of temperature and moisture on FRP-concrete joint

The bond between the epoxy resin and the concrete substrate is established by first mechanical interlocking and second chemical interaction (Blackburn et al., 2015; Cabral-fonseca et al., 2018; J Tatar, Weston, Blackburn, & Hamilton, 2013). The mechanical interlocking is formed by flowing the resin into the holes and pores of the concrete. Although the nature of the chemical bond is not fully understood, it is believed that it is formed by hydrogen bonds between epoxy and hydrated cement (Blackburn et al., 2015; Cabral-fonseca et al., 2018; Djouani, Connan, Delamar, Chehimi, & Benzarti, 2011). Bond degradation is a complicated process that finally leads to FRP debonding from the concrete substrate.

Temperature influences the mechanical properties of the epoxy resin more than the fibers themselves. Consequently, since the resin plays a crucial role in stress transfer within the fiber and between the fiber and concrete substrate, it is expected that the bond between the FRP composite and concrete substrate is the first parameter influenced by temperature increase. Studies (Blontrock, 2003; Cromwell et al., 2011; Ferrier et al., 2015; J. P. Firmo et al., 2015) showed that temperatures lower than T_g might have a limited effect on the bond strength where it may stimulate the beneficial post-curing effect in some cases. Temperatures approaching or exceeding the T_g can be harmful to the bond strength. Ferrier et al. (Ferrier et al., 2015) reported that increasing the temperature from 20^{o}C to 60^{o}C and 80^{o}C can reduce the bond strength by 38% and 70%, respectively. It is worth noting that Ferrier et al. used a resin with T_g of 76^{o}C. Researchers have also reported that exposing CFRP-concrete joint to a high temperature may also increase the effective bond (J P Firmo, Correia, Pitta, Tiago, & Arruda, 2015; Leone, Matthys, & Aiello, 2009).

Studies showed that not only high temperature could have a harmful influence on the bond strength, but also low temperature (lower than water freezing temperature). Results revealed that decreasing the temperature from 20 to -40 can reduce the bond strength by 5% (Ferrier et al., 2015). Table 2-3 reports the result of some studies regarding the effect of temperature on the bond behavior of the CFRP-concrete joint.

Moisture is another factor that could influence the bond of the FRP-concrete joint. Moisture penetration to the interface can accelerate the debonding process by three

means: (i) moisture can soften the epoxy via plasticization as discussed in section 2.2.1; (ii) epoxy swelling stimulated by moisture absorption can create internal stress in the interface leading to cracking and debonding; (iii) moisture can reduce the mechanical interlocking (Sen, 2015). Table 2-3 presents some of the studies that investigated the effect of moisture on the FRP-concrete interface. It can be noticed that degradation of the bond strength depends on the exposure periods, temperature, materials, test method, and specimens' configurations.

Finally, it is worth mentioning that most of the studies available in the literature have been conducted in laboratories and involved accelerated aging conditions. Considerably few studies have investigated the effect of the outdoor exposure environment (M. I. Kabir, Shrestha, et al., 2016; Nishizaki & Kato, 2011). Kabir et al. (M. I. Kabir, Shrestha, et al., 2016) studied the effect of outdoor exposure environment of Sydney, Australia on the bond strength of the CFRP bonded to a concrete prism. Exposure conditions included 5-35^{o}C temperature, 4-100% RH and 1-33 MJm^{-2} solar and for 2-18 months. Results indicated a 15.2% reduction in the bond strength after 6 months of exposure. However, the reduction in the bond strength was decreased to 8.6% after 18 months, implying that it can retrieve part of its strength. This fluctuating behavior in the bond strength was attributed to the conflicting effect of the outdoor environments on the concrete strength and epoxy resin strength. Nishizaki and Kato (Nishizaki & Kato 2011) investigate the effect of the outdoor environments on the CFRP-concrete joint made of four types of CFRP sheets using a pull-off test. Exposure periods were up to 14 years. Results indicated a reduction in the pull-off strength ranging between 65% and 76%; nonetheless, the failure mode was always a cohesive failure within the concrete substrate.

Table 2-3: effect of temperature and moisture on the FRP-concrete joints

Authors	Materials	Exposure conditions	Conclusions
Ferrier et al. (Ferrier et al., 2015)	• CFRP sheets bonded with epoxy resin • CFRP strips bonded with epoxy adhesive	• The first system was exposed to a high temperature between 40°C and 80°C. In addition, it was exposed to a low temperature down to -40°C. • The second system was exposed to high temperature up to 120°C and low temperature down to -20°C	• The bond strength of the first system was reduced by 38% and 70% when the temperature was increased to 60°C and 80°C, respectively. Besides, the bond strength was also decreased by 5% when the temperature was decreased to -40°C. The failure mode of the first system was shifted from a cohesive failure in the concrete substrate into an adhesive failure within the substrate • The bond strength of the second system was decreased by 16% and 30% when the temperature was increased to 50°C and 100°C, respectively. Bond strength was also decreased by 40% when the temperature was decreased to -20°C.
Firmo et al. (J. P. Firmo et al., 2015)	• CFRP strips bonded with epoxy adhesive	• Steady-state: specimens were heated to a predefined temperature (20 °C, 55 °C, 90 °C, 120 °C), then they were loaded until failure • Transient state: specimens were loaded to a percent of the strength at the ambient temperature (25%, 50%, 75%); after that, they heated until failure	• Changing the exposure condition from the steady-state to the transient state did not have a significant effect on the results. • Increasing the exposure temperature caused a considerable reduction in the bond strength and stiffness • The effective bond length of the conditioned specimens was increased in comparison with the reference specimens.
Mikami et al. (Mikami, Wu, & Elarbi, 2015)	• CFRP sheet bonded with epoxy resin	• Thermal cycles (50, 100, and 250): 2 hours cycle 15 minutes of ramp-up (from 25 °C to 100 or 180 °C) followed by 75 minutes constant temperature and finally 30 minutes ramp down to 25 °C.	• 11% reduction in the pull-off strength after 250 cycles at temperature 100°C. The reduction in the pull-off strength was increased to 50% when the temperature was increased to 180 °C for the same number of cycles.
Au and Büyüköztürk (Au	• Prefabricated CFRP laminate	• WI at 23 and 50°C for 2-8 weeks	• Reduction in the flexural toughness

& Büyüköztürk, 2006)			• Reduction in the bond strength fracture toughness
Dai et al. (Jian-guo Dai, Yokota, Iwanami, & Kato, 2010)	• Wet layup CFRP sheets with 2 types of epoxies	• WD for 8, 14, and 24 months: 4 days immersion in seawater for 4 days at 60°C and 3 days drying at lab temperature	• Results of the three-point bending test were dependent on the type of epoxy. For one type, flexural strength and ductility slightly increased for 8 and 14 months. However, they were decreased after 24 months. • For the second type of epoxy, flexural strength decreased for all the exposure periods; yet, the ductility was not affected.
Benzarti et al. (Benzarti, Chataigner, et al., 2011)	• Prefabricated CFRP laminate and wet layup sheet	• CC at 95% RH at 40°C	• Increase in the bond strength within 10-15% based on the single-lap shear test • 60% reduction in the pull-off strength of the laminate • 25% increase in the pull-off strength of the sheet
Lai et al. (Lai, Kou, Poon, Tsang, & Lai, 2009)	• Prefabricated CFRP	• WI for 50 weeks at 25, 40 and 60°C	• Bond strength was decreased by 8% at 40°C and 21% at 60°C based on the single-lap shear test • Adhesive failure for the case of 40°C and 60°C
Kabir et al. (M. I. Kabir, Shrestha, et al., 2016)	• Wet layup CFRP sheet	• WD cycles for 18 months: 1 week at 95% RH and 1-week drying	• No clear trend in the behavior of the bond strength • Failure mode was shifted from a cohesive failure within the concrete substrate into adhesive within the interface.
Shrestha et al. (Shrestha et al., 2015)	• Wet layup CFRP sheet and 3 types of epoxies	• WI at 20°C • WD cycles for 3-18 months: 7 days immersed in water at 20°C and 4 days drying at 20°C	• Both conditioning environments has a similar effect of a small reduction in the bond strength (1-12%) for both aging conditions • Failure mode was shifted from a cohesive within the concrete substrate into an adhesive within the interface or a mixed-mode
Tuakta et al. (Tuakta & Büyüköztürk, 2011)	• Prefabricated CFRP laminates	• WI at 23°C and 50°C for 1-8 weeks	• Testing the specimens in a wet condition after exposure to WI environments shows a significant reduction in the peel and shear toughness and the

		• WD at 23°C and 50°C: 2-8 cycles a week, 2-8 cycles in 2 weeks, and 2-4 cycles in 3 weeks	degradation was higher for the more extended exposure periods and higher temperature. • Drying the specimens after conditioning allowed them to regain a part of their bond strength • For WD cycles, degradation of the peel and shear toughness was increasing with increasing the number of cycles and the conditioning temperature.
Ceroni et al. (Ceroni, Bonati, Galimberti, & Occhiuzzi, 2018)	• Wet layup CFRP sheet	• WI at 23°C, 30°C and 40°C for 4-74 days • All the tests were conducted in an environment-controlled room to perform the test in an environment similar to the one that the specimens were exposed to	• Continuous reduction in the bond strength with the proceeding of the aging period. • The higher the aging temperature is, the higher bond deterioration is obtained. Furthermore, utilizing higher aging temperatures can produce the same degradation level but with a shorter period. • Drying the specimens after conditioning allowed them to reverse part of the deleterious effect.

2.3 Durability of FRCM composite

The durability of FRCM composites depends on the long-term behavior of their components (matrix and fiber textile) and of the interfaces between them. The durability of each component and the matrix–fiber and composite–substrate interfaces is discussed in the following subsections based on the studies available in the literature. Results are presented in term of retained (or residual) strength ratio, which is defined as the ratio σ_f/σ_{fu} between the strength σ_f of the conditioned specimens (i.e., exposed to the conditioning environment) and the strength σ_{fu} of the unconditioned specimens.

2.3.1 Durability of FRCM matrices

The inorganic matrix employed in FRCM composites is generally cement-based or lime-based, although other types can be found in the literature, see, e.g. (Pekmezci et al., 2019; Yin, Jing, Yin, & Wang, 2019). This section focuses on the durability of cement-based and lime-based matrices. In the figures presented in this section, the blue color indicates cement-based matrix, whereas the orange color indicates lime-based matrix.

Exposing FRCM matrices to freeze-thaw cycles may influence its durability. For example, the water present within the matrix's voids may freeze when exposed to low temperatures, increasing its volume by 9% (Colombo, Colombo, & Di Prisco, 2015). Consequently, it may crack the matrix if the internal stresses exceed its tensile strength. However, research available regarding freeze-thaw of FRCM composites did not generally report the specimens' moisture content. Figure 2-1 illustrates the effect of the freeze-thaw cycles on the retained cracking (tensile) strength of various FRCM matrices evaluated using the uniaxial tensile test on FRCM (Arboleda, 2014; Pekmezci et al., 2019) and Textile Reinforced Concrete (TRC) coupons. All specimens exposed to less than 100 cycles showed an enhancement of the matrix cracking strength. However, a large scatter of the result was observed (Colombo et al., 2015). Moreover, Colombo et al. (Colombo et al., 2015) reported a continuous increase in the matrix tensile strength from 50 to 100 cycles, whereas De Munck et al. (De Munck et al., 2018) observed a reduction for 100 cycles. The difference in the obtained results is ascribed to the different performances of the adopted matrices. Colombo et al. (Colombo et al., 2015) utilized a

high-strength cementitious matrix (average cubic compressive strength and flexural strength equal to 97.5 MPa and 13.6 MPa, respectively), whereas De Munck et al. (De Munck et al., 2018) used a cement-based matrix with average cubic compressive strength and flexural strength of 29.6 MPa and 5.0 MPa, respectively. Researchers indicated that concrete with high strength is less vulnerable to freeze-thaw cycles due to its low permeability (Lomboy, International, & 2009, n.d.; Sun, Zhang, Yan, & Mu, 1999), which can explain the better performance of the matrix with the highest compressive and tensile strength. In addition, the range of temperature and the length of the freeze-thaw cycles utilized by Colombo et al. (Colombo et al., 2015) were shorter and smaller, respectively, than those adopted by De Munck et al. (De Munck et al., 2018). However, after 100 cycles, Figure 2-1 shows that the retained matrix cracking strength decreased due to the development of microcracks (Colombo et al., 2015; De Munck et al., 2018). Yin et al. (Yin et al., 2019) used a four-point bending test to study the combined effects of freeze-thaw cycles (−18 °C to 5 °C with 3 h cycle length) and saline environment (5 wt. % NaCl) on the cracking strength of TRC composites. Results of this study are not reported in Figure 2-1 because it considers the effect of the saline environment. The retained cracking strength was 0.98, 0.91, and 0.86 after exposure to 50, 70, and 90 cycles, respectively. Similarly, it can be noticed that the conditioning environment did not have a significant effect on the small number of cycles. However, the degradation gradually increased with increasing the number of cycles. The degradation developed with 90 cycles was slightly higher than the one reported by De Munck et al. (De Munck et al., 2018) with a similar number of cycles (100 cycles). This difference between the two studies can be attributed to (i) the presence of the sodium chloride that may increase the degradation process rate and (ii) the test method employed (four-point bending test vs. uniaxial tensile test).

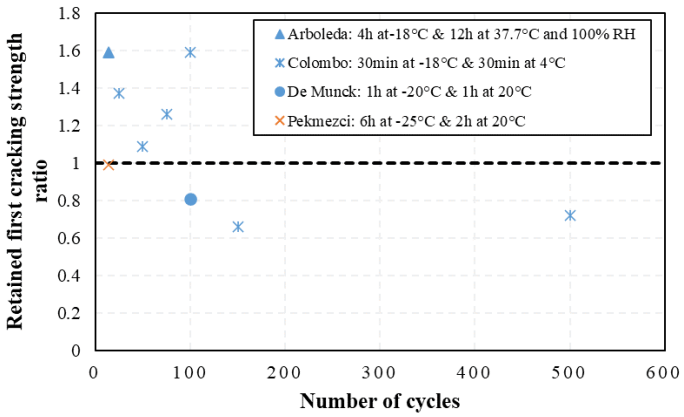

Figure 2-1: Effect of freeze-thaw cycles on the matrix tensile strength (blue marker = cement-based matrix, orange marker = lime-based matrix).

Chlorides and sulfates can interact with some components of the matrix, such as calcium hydroxide ($Ca(OH)_2$) and aluminum oxide (Al_2O_3), leading to a reduction of the matrix durability (Arboleda, 2014). Figure 2-2a shows the effect of continuous immersion in a saline solution (seawater or 3.5 wt. % of NaCl) on the retained strength of the FRCM matrices. Nobili et al. (Nobili, 2016) and Donnini et al. (Donnini, 2019) used a three-point bending test of lime-based matrix specimens according to EN 1015 (EN 1015-11, 2019). Arboleda (Arboleda, 2014) investigated the cracking strength of cement-based FRCM coupons using uniaxial tensile tests. The results showed that though Nobili et al. (Nobili, 2016) used a lower aging temperature than Donnini et al. (Donnini, 2019), the degradation of the matrix was higher (up to 60%, see Figure 2-2). This controversial finding might be ascribed to the difference in the porosity and mechanical properties of the matrices investigated by the two researchers. A matrix with high porosity, such as a natural lime-based matrix, could be more affected by saline environments than hydraulic lime or cementitious matrices (Donnini, 2019). Further studies are needed to relate the physical nature of the FRCM matrices with their durability in various environmental conditions. Arboleda (Arboleda, 2014) reported a remarkable increase in the cracking strength of the cement-based matrix. This result was not significantly affected even when the exposure period was extended to 3000 h.

Figure 2-2b shows the effect of wet-dry cycles in saline solutions on the retained strength of the matrices. Regarding the cementitious matrix, Yin et al. (Yin et al., 2019) performed 12 h of wetting in a saline solution (5 wt. % of NaCl) followed by 12 h of drying at room temperature on TRC coupons with cement-based matrix, which was subsequently tested using a four-point bending test. The results showed that the matrix flexural strength progressively decreased with increasing the number of cycles. Regarding the lime matrix, Donnini (Donnini, 2019) reported similar residual flexural strengths for specimens subjected to continuous immersion and wet-dry cycles, showing a percentage reduction of approximately 10%.

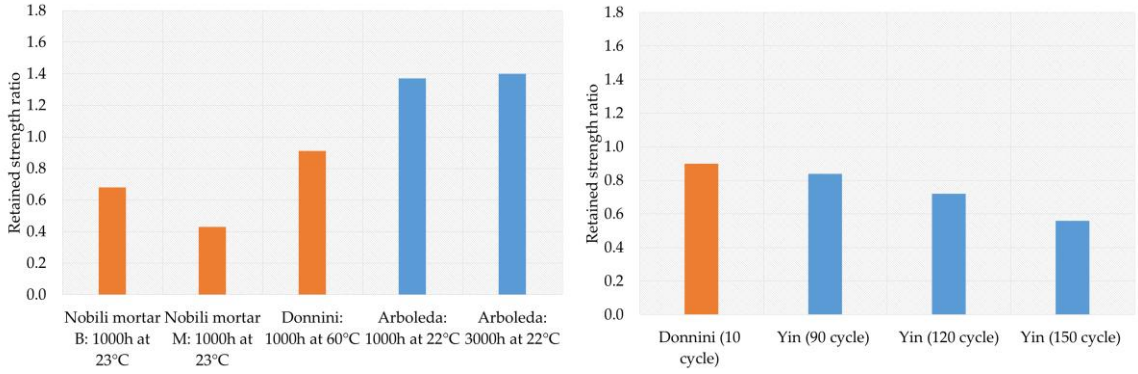

(a) *(b)*

Figure 2-2: Effect of saline environments on the matrix tensile strength: (a) continuous immersion and (b) wet-dry cycles (blue bin = cement-based matrix and orange bin = lime-based matrix).

Alkali-aggregate chemical reaction, which is the reaction between the potassium and sodium oxide (K_2O and Na_2O) of the cement and the reactive silica (SiO_2) present in some types of aggregate, may affect glass micro-fibers (if present) dispersed within the matrix (Arboleda, 2014). The effect of matrix immersion in alkaline solution on the flexural (Nobili, 2016) and uniaxial tensile strength (Arboleda, 2014) is presented in Figure 2-3. It can be noticed that the retained flexural strength of the lime-based matrix decreased to approximately 55%, whereas the retained tensile strength of the cement-

based matrix was not significantly affected (a slight increase, lower than 10%, was observed).

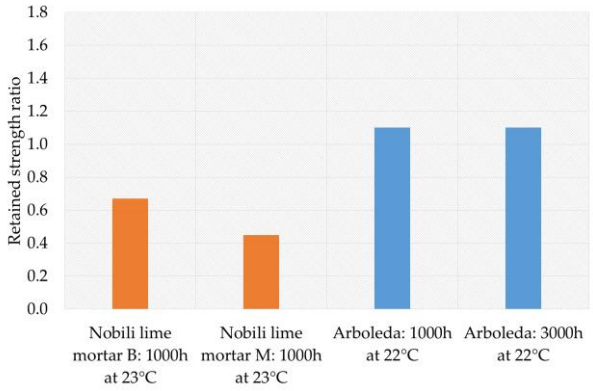

Figure 2-3: Effect of the alkaline environment on the matrices (blue bin = cement-based matrix and orange bin = lime-based matrix).

Finally, exposing matrix to a conditioning environment containing deionized water, which is a common condition used to study the performance of GFRP reinforcing bars (T. D'Antino et al., 2018), can improve the performance of the cement-based matrix if it is followed by an appropriate drying period due to the resumption of the hydration process (Ceroni et al., 2018; Donnini, 2019). Table 2-4 presents some studies on the performance of the FRCM matrix under various environments

Table 2-4: effect of various conditions on the FRCM matrix

Authors	Materials	Exposure conditions	Tests	Results in term of the average retained strength	Comments
Arboleda (Arboleda, 2014)	• Cement-based matrix	• CC: 100% RH at 37.7°C for 1000-3000 hour • FT: 20 cycles with 4 hours at -18°C and 12 hours at 37.7°C and 100% RH • Saline: (seawater) • Immersion in alkaline solution [$Ca(OH)_2$, KOH, NaOH] with pH>12	• Visual inspection of the coupon surfaces with 5x magnification lenses • Uniaxial tensile test on FRCM coupon	• CC: at 1000h and 3000h was 1.56 and 1.34, respectively. • FT: 1.59 • Saline: at 1000 and 3000h was 1.37 and 1.4, respectively. • Alkaline: it was 1.1 for both1000 h and 3000 h	• Results reported represents the first cracking strength measured by the uniaxial tensile test on the FRCM coupon • No surface degradation for all conditioning environments except in the case of the FT cycles where small scaling was detected
Colombo et al., (Colombo et al., 2015)	• Cement-based matrix	• FT (ASTM C666, 2015) (25-500 cycle): 30 min at +4, 30 min at -18 and cooling/heating rate was11°C/h	• Uniaxial tensile test on the TRC coupon	• FT: The retained strength at (25, 50, 75, 100, 150, and 500) cycle was (1.37, 1.09, 1.26, 1.59, 0.66 and 0.72) respectively.	• No clear detrimental effects, but the improvement was noticed sometimes in the first cracking strength for small number cycles (up to 100 cycles) • Reduction in the first cracking strength was noticed for the higher number of cycles (150-500 cycle)
Yin et al. (Yin et al., 2019)	• Cement-based matrix	• Combined effect of FT (50, 70, and 90	• Four-point bending test	• Retained first cracking	• Similar to the results reported by Colombo et

		cycles with 3 hours cycle length and a temperature range between -18°C to 5°C) and saline environment (5 wt% NaCl)		strength after exposure to 50, 70, and 90 cycles were equal to 0.98, 0.91, and 0.86, respectively	al. (Colombo et al., 2015), there are no significant effects for the small number of cycles. Nonetheless, the degradation increase with increasing the number of cycles.
Ceroni et al., (Ceroni et al., 2018)	• Fiber-reinforced cement-based matrix with a polymeric portion of 4%	• WI at the 23ºC for 5-28 days	• bending test (CEN, 2011) • Compressive test • Three specimens for each condition	• Retained flexural and compressive strength after 28 days of WI was 0.67 and 0.74, respectively.	• Obvious reduction in the compressive and tensile strength of matrix tested in a wet condition after 5 and 28 days of being immersed in water. However, this reduction can be reversed or even changed into an increase in the compressive and tensile strength by drying the specimens after been exposed to WI condition
De Munck et al., (De Munck et al., 2018)	• Cement-based matrix	• FT: 100 cycles with a temperature range of (-20 to 20) (BS EN 12467, 2004) • Heat-rain (HR) of 50 cycles: heating to 60ºC within 15 min and maintained for 45 min then cooled with water immersion in 15ºC.	• Uniaxial tensile test on FRCM coupon • Crack width and crack spacing via DIC	• The Average retained first cracking strength for the specimens exposed to FT was 0.81 • The Average retained first cracking strength for the specimens exposed to HR was 0.7	• Pronounced reduction in the first cracking strength for all the aging conditions. • Increasing in the number of cracks and reduction in the spaces between them at the early stages of loading due to environmental conditioning • A noticeable reduction in the uncracked

		• Combined effect of the two previous environments with 100 cycle FT followed 50 cycle heat-rain		• Average retained first cracking strength for the specimens exposed to the combined effect of FT and HR was 0.6	stiffness is attributed to microcracks initiated during the aging period.
Donnini (Donnini, 2019)	• Lime based matrix	• WI: tap water at 60ºC for 1000h • Immersion in saline solution (3.5% NaCl) at 60ºC for 1000h • WD 10 cycles (960h): 2 days immersion in saline solution (3.5% NaCl) at 60ºC and 2 days drying at 60ºC	• Flexural test • Compressive test	• WI: Small Increment (1.03 and 1.06) in the retained flexural and compressive strength, respectively. • The retained flexural and compressive strength after continuous immersion in saline solution became 0.91 and 1.08, respectively. • WD cycles in saline solution: slight decrement in the flexural and compressive strength of 0.9 and 0.95	• It is believed that the first two conditions stimulate the resumption of the curing process. However, the wet-dry cycle interrupted the curing process; besides, it is promoted salt penetration and accumulation within the matrix's voids.

Nobili (Nobili, 2016)	• Matrix B: rich in hydrated lime and pozzolan • Matrix M: air-hardening lime, pozzolan, and marble sand	• Immersion in alkaline solution (Sodium bicarbonate, pH=10) for 1000 hour • Immersion in saline solution (3.5% sodium chloride) for 1000 hour	• Three-point bending test	• Alkaline: retained strength was decreased for matrix B and M to become 0.67 and 0.45, respectively. • Saline: like the previous condition, retained strength was also decreased to become 0.68 and 0.43 for matrix B and M, respectively.	• Obvious reduction in the load capacity, especially for matrix M in both aging environments
Pekmezci et al., (Pekmezci et al., 2019)	• Lime based matrix	• FT: 14 cycles of 2 hours in water at 20^{o}C and 6 hours at -25^{o}C in the freezer	• Uniaxial tensile test on matrix and FRCM coupon	• Reduction in the retained tensile strength of the matrix to become 0.63 • Retained first cracking strength of the FRCM coupon was 0.99 after exposure showing no signs of degradation	• Pronounced reduction in the deformation capacity of the matrix

2.3.2 Durability of fibers

Textiles used in FRCM can be made of carbon, AR-glass, PBO, aramid fibers, and steel (in the case of SRG). Although carbon fiber showed good durability (Benzarti, Chataigner, et al., 2011; Williams Portal, Flansbjer, Johannesson, Malaga, & Lundgren, 2016), it has a high cost in comparison with other fibers such as AR-glass or basalt. Basalt fiber is often compared to E-glass and AR-glass due to the similarities in the chemical structure (Scheffler et al., 2009; Williams Portal et al., 2016). Limited results on the durability of PBO fibers employed in the civil engineering field can be found in the literature. AR-glass fiber is commonly used in civil engineering applications due to its availability and low cost. For these reasons, more results are available regarding the durability of AR-glass fiber than other types of fiber. In the figures presented in this section, the blue color indicates tests at room temperature, whereas the orange color indicates tests at a temperature equal to 60 °C.

To the author's best knowledge, there is no information available on the effect of the freeze-thaw cycles on the long-term behavior of fiber textiles employed in FRCM composites. Similarly, no results were found regarding the effect of sulfate exposures.

The retained tensile strength of AR-glass textiles subjected to hygrothermal environments reported by different research groups is shown in Figure 2-4. Portal et al. (Williams Portal et al., 2016) reported no difference in the tensile capacity after 10 days of conditioning at 20 °C. However, Hristozov et al. (Hristozov, Wroblewski, & Sadeghian, 2016) reported a 15% reduction after 21 days of aging. When the aging temperature was raised to 60 °C, both Portal et al. (Williams Portal et al., 2016) and Hristozov et al. (Hristozov et al., 2016) noticed an apparent reduction in the strength, higher than 60%. Nonetheless, Donnini (Donnini, 2019) did not report a significant change in the textile tensile capacity at the same temperature (i.e., 60 °C). This conflict in the obtained results may be attributed to the difference in the coating materials of the fibers used by each research group. The fiber used by Portal et al.(Williams Portal et al., 2016) and Hristozov et al. (Hristozov et al., 2016) was coated with 20% of styrene-butadiene resin (SBR) and vinyl ester, respectively, whereas the fiber used by Donnini (Donnini, 2019)

was coated by polyvinyl alcohol (PVA). In addition to the effect of coating, the difference in the textile layout and the number of fiber filaments in each yarn may also have influenced the results.

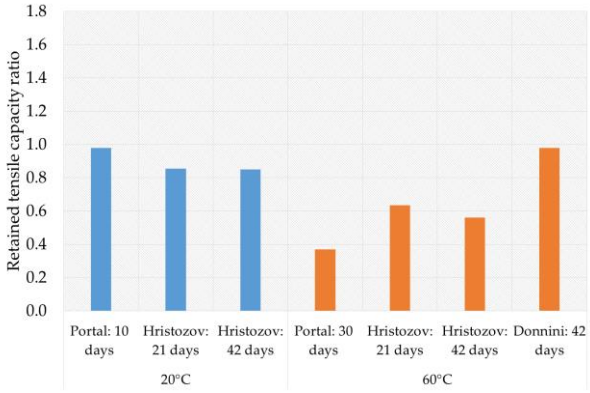

Figure 2-4: Retained tensile capacity of AR-glass exposed to hygrothermal environments (blue bin = room temperature and orange bin = temperature equal to 60 °C).

Figure 2-5 presents the retained tensile capacity of AR-glass fibers immersed in seawater (3.5 wt. % of NaCl) for 1000 h (~42 days). At room temperature (ranging between 20 °C and 23 °C), Nobili et al. (Nobili, 2016) and Hristozov et al. (Hristozov et al., 2016) reported a minor degradation of the tensile capacity. However, the degradation increased up to 40% when the conditioning temperature was raised to 60 °C.

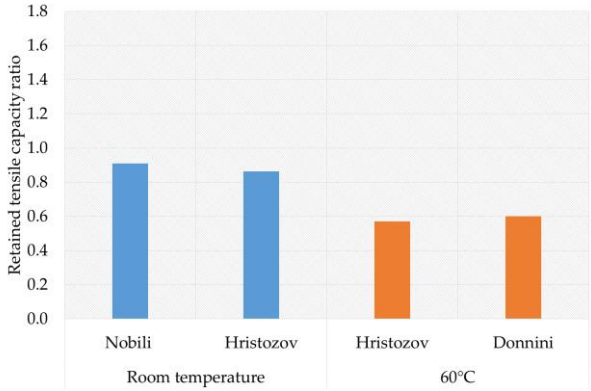

Figure 2-5: Retained tensile capacity of AR-glass immersed in seawater (blue bin = room temperature and orange bin = temperature equal to 60 °C).

The effect of the alkaline solution on the tensile capacity of AR-glass textiles is presented in Figure 2-6. At room temperature, different levels of degradation were reported depending on the alkalinity of the solution, exposure period, and fiber coating materials (Nobili, 2016; Scheffler et al., 2009; Williams Portal et al., 2016). The degradation level increased with increasing the alkalinity and the exposure period. Furthermore, when the conditioning temperature was raised to 60 °C, the degradation level was increased, especially in the case of Portal et al. (Williams Portal et al., 2016), where the material completely failed (dissolved) before performing the tensile test (these results are not shown in Figure 2-6 for this reason). Butler et al. (Butler, Mechtcherine, & Hempel, 2009, 2010) studied the durability of the AR-glass embedded in three different types of cementitious matrices with different levels of alkalinity. Since the textiles were not immersed in an alkaline solution as in previous studies, results are not included in Figure 2-6. It was implied that increasing the conditioning period can increase the reduction in tensile strength of the textiles. Furthermore, FRCM coupons made with a high alkalinity matrix developed a brittle failure, as going to be discussed in Section 2.3.3.

It should be noted that the accelerated aging environments considered to study the durability of glass fibers represent highly harsh conditions that are never present in real applications. Therefore, detailed investigations on the effect of these harsh conditions on the fiber coatings, which protect the fiber from external attacks, should be carried out to correctly understand the results obtained.

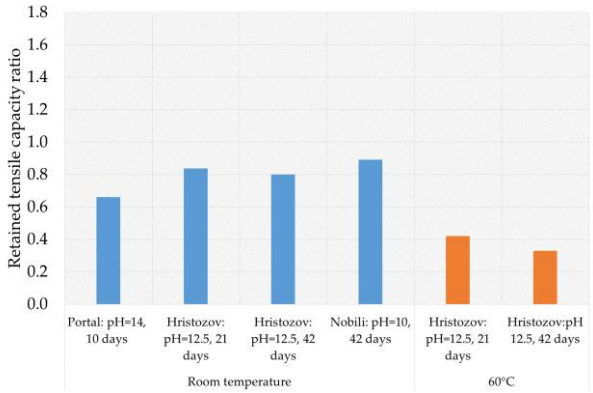

Figure 2-6: Retained tensile capacity of AR-glass exposed to alkaline environments (blue bin = room temperature and orange bin = temperature equal to 60 °C).

Regarding the durability of steel cords employed in SRG composites, unlike the numerous studies on the corrosion of galvanized steel rebar in concrete (Fayala, Dhouibi, Nóvoa, & Ben Ouezdou, 2013; Roventi, Bellezze, Giuliani, & Conti, 2014; Yadav, Nishikata, & Tsuru, 2004), there is limited research addressing the corrosion of steel cords embedded in an inorganic-matrix (Franzoni et al., 2018). The performance of steel fibers can be highly dependent on the environment and duration of the exposure. For instance, a prolonged exposure period to an environment containing chloride ions can cause strong steel corrosion. Franzoni et al. (Franzoni et al., 2017) investigated the performance of the steel SRG-masonry joints under wet-dry cycles exposed to a saline solution containing an 8% weight ratio of $Na_2SO_4 \cdot 10H_2O$. In this study, steel fiber did not show significant changes. However, in another study by the same authors (Franzoni et al., 2018), steel fibers were corroded when 2 wt. % of NaCl was added to the same solution, and the number of cycles was increased from 4 to 6.

The limited number of results available in the literature indicates that further studies are needed to gain a deeper understanding of the long-term behavior of the steel cords under various environments. Finally, more information about the studies discussed in this section can be found in Table 2-5.

Table 2-5: effect of the various environments on different types of fibers

Authors	Materials	Exposure conditions	Tests	Results in term of the average retained strength	Comments
Donnini (Donnini, 2019)	• AR-glass coated with PVA (polyvinyl alcohol)	• Immersion in saline solution (3.5% NaCl) at 60°C for 1000h • WD 10 cycles (960h): 2 days immersion in saline solution (3.5% NaCl) at 60°C and 2 days drying at 60°C • WI tap water at 60°C for 1000h	• Uniaxial tensile test on single fiber yarn • Scanning electron microscopy (SEM)	• Saline: average retained tensile strength of the specimens exposed to continuous immersion and WD cycles in saline solutions decreased to become 0.6 and 0.36, respectively. • WI: retained tensile strength was not affected (0.98)	• Reduction in the ultimate strain for both cases of the saline environments • Modulus of elasticity was not significantly affected by all the environments.
Hristozov et al. (Hristozov et al., 2016)	• Unidirectional glass fabric impregnated in vinyl ester resin	• WI in distilled at 20, 50, and 60°C for 500, 1000, 2000, and 3000h. • Saline (3.5 wt.% of NaCl) at 20, 50 and 60°C for 500, 1000, 2000, and 3000h • Alkaline (pH= 12.5): at the	• Uniaxial tensile test based on the ASTM D638 (ASTM D638-03, 2004)	• WI: retained tensile strength was decreased from (0.85) at 500h and 1000h to 0.64 and 0.56, respectively, when the temperature increased from 20°C to 60°C. • Saline: retained tensile strength	• The tensile strength of the glass fiber is sensitive to both the temperature and exposure period of the water, where it decreases continuously when the temperature and the exposure period increase. • Similar to the previous condition, increasing the aging temperature

		same temperature and exposure periods of the previous conditions		was decreased from 0.86 to 0.57 when the exposure temperature increased from 20ºC to 60ºC • Alkaline: retained tensile strength from 0.84 and 0.8 at 500h and 1000h to 0.42 and 0.33 when the temperature increased from 20ºC to 60ºC.	and the exposure period can have an apparent harmful effect on the tensile strength of the fiber aged in saline or alkaline solutions.
Nobili (Nobili, 2016)	• AR-glass impregnated (coated) with a polymeric resin	• Immersion in alkaline solution (Sodium bicarbonate, pH=10) for 1000 hour • Immersion in saline solution (3.5% sodium chloride) for 1000 hour	• Uniaxial tensile test on the fiber fabric	• Alkaline: retained strength was 0.89 • Saline: retained strength was 0.91	• Although the high scatter in the results, a minor degradation in the tensile strength was observed.
Portal et al. (Williams Portal et al., 2016)	• AR-glass fiber • Basalt fiber • Carbon finer	• Alkali resistant based on the ISO 10406-1 (ISO 10406-1): immersion in alkaline solution (0.8% of NaOH	• Uniaxial tensile test on single yarn • Visual inspection	• WI: retained strength was decreased from 0.98 to 0.39 when the temperature increased from	• Based on the visual inspection, carbon fibers did not show any significant changes. Besides, it showed an

	and 2.24% of KOH) pH= 14 for 5-30 days at 60°C. • WI in deionized water at 60°C for 30 days was inspected • Immersion in the alkaline solution for 10 days at 20°C • WI in deionized water for 10 days at 20°C.	•	10°C to 60°C and the exposure period increased from 10 to 60 days. • The retained strength of the AR-glass after exposing to an alkaline environment for10 days in the lab temperature was 0.66	increment in tensile strength and stiffness. • Both AR-glass and basalt fibers aged in the first condition environment showed a significant degradation, especially after 10 days of aging. Degradation included changes in the color, coating, and loss of physical strength. Besides, all the specimens failed during the aging process before performing the uniaxial tensile test. • Regarding the second aging condition (WI), both AR-glass and basalt fibers experienced changes in color and coating separation. Moreover, they had physical strength reduction; yet, they did not fail during the conditioning. • Basalt fiber exposed to the 3rd aging condition experienced minor color change, slight cover separation, and

					physical strength reduction. • AR-glass exposed to the 3rd condition developed a wavy deformed shape; yet, it preserved enough physical strength. • The 4th aging condition had the least effects on the AR-glass
Butler et al. (Butler et al., 2010)	• AR-glass fiber • Three types of matrices (M_1, M_2, M_3) with different level of alkalinity	• Aging period: 28-360 days • M_1 concrete: low alkalinity reduced from pH = 12.4 at mixing to pH= 11.8 after 1 year. • M3 concrete: high alkalinity of pH=12.7 M2 concrete: with a medium level of alkalinity ranging between M1 and M3	• Uniaxial tensile test on FRCM coupons reinforced with 5 layers of textile Pull-out test	• Retained tensile strength of the FRCM coupon made of matrix M_1, M_2, and M_3 after 360 days was 0.97, 0.62, and 0, respectively.	• Continuous decrement in the ultimate strength and strain with the proceeding of the aging periods for all the concrete types • The deterioration was evident in the case of the M_3 matrix, where all the aged specimens developed a completely brittle failure with no multiple cracks referring to dramatic corrosion of the AR-glass fiber within the concrete matrix.

2.3.3 Durability of the matrix–fiber interface

The effectiveness of externally bonded reinforcements depends on the stress transfers between its components and between the reinforcements and the substrate. When a single layer of fiber is employed, externally bonded FRCM composites have two primary interfaces, i.e., the matrix-fiber interface and the matrix-substrate or composite substrate interface (Christian Carloni, D'Antino, Sneed, & Pellegrino, 2018). Although the long-term bond behavior of the various interfaces of an inorganic-matrix composite should be studied with bond tests, some studies available in the literature derived information on the effect of various environmental factors on the matrix–fiber interface from a uniaxial tensile test of composite coupons (Arboleda, 2014; Colombo et al., 2015; Nobili, 2016). In particular, the degradation of the matrix–fiber interface was assessed by direct observation using scanning electron microscopy (SEM) (De Munck et al., 2018) or evaluated by studying the differences in the load response of control and conditioned specimens that can be explained by the matrix–fiber bond behavior.

Bond in the FRCM composites is mainly established by mechanical interlocking between fibers and matrix. However, unlike FRP-concrete interface that losses its stress transfer mechanism after debonding, debonded FRCM composites attain a residual strength due to friction among the fibers of a single filament on one side and between fibers and matrix on the other side (T. D'Antino et al., 2014). In this section, the effect of various environments on the matrix-fiber bond behavior, either directly studied with bond tests or derived by uniaxial tensile tests, as discussed, whereas the durability of the composite–substrate interface is discussed in Section 2.3.4.

Figure 2-7 presents the effect of freeze-thaw cycles on the ultimate strength of FRCM coupons comprising different types of textiles. Colombo et al. (Colombo et al., 2015) investigated the effect of freeze-thaw cycles on uncracked specimens and on specimens cracked by applying a uniaxial tensile load 20% higher than the cracking load. It can be noticed that the retained ultimate strength of the uncracked specimens progressively decreases with increasing the number of cycles until it reaches 0.8 at the end of 500 cycles. However, cracked specimens showed fluctuating results, and a clear trend could not be identified. Arboleda (Arboleda, 2014) reported a slight increment (approximately

10%) in the ultimate strength of PBO-FRCM coupons, whereas the ultimate strength of carbon-FRCM coupons did not change significantly. Pekmezci et al. (Pekmezci et al., 2019) reported a slight reduction (approximately 16%) in the case of a biaxial fabric. De Munck et al. (De Munck et al., 2018) reported a slight reduction (approximately 16%) in the ultimate strength of TRC coupons with AR-glass fibers after 100 cycles. Anyhow, freeze-thaw cycles had a slight effect on the coupon ultimate strength, being the variation always lower than 20%.

Yin et al. (Yin et al., 2019) utilized a pull-out test to investigate the combined effect of freeze-thaw cycles (−18 °C to 5 °C with 3 h cycle duration) and saline environments (5 wt. % of NaCl) on the matrix–fiber bond capacity. The obtained results are not presented in Figure 2-7 since the authors considered the effect of saline solution and used a different test setup. However, Yin et al. (Yin et al., 2019) reported the insignificant effects of the aging condition.

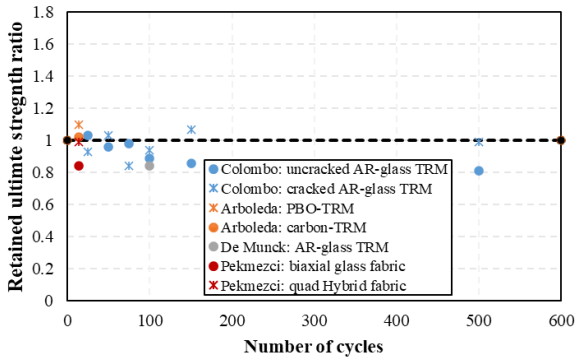

Figure 2-7: Effect of freeze-thaw cycles on the retained ultimate strength of composite coupons.

The effect of saline environments on the matrix-fiber bond behavior was investigated by immersing FRCM coupons in saline solutions (seawater or 3.5 wt. % of NaCl) and observing the variation of the ultimate strength, which was attributed to the degradation of the matrix-fiber interface (Arboleda, 2014; Nobili, 2016).

Figure 2-8 shows the retained ultimate strength of FRCM coupons immersed in saline solutions for different periods. Arboleda (Arboleda, 2014) reported an increase in the retained ultimate strength of carbon and PBO FRCMs. This increment (larger than 40%)

was attributed to the continuous hydration of the matrix, which may improve the matrix–fiber bond behavior, leading to high ultimate strengths. Nobili et al. (Nobili, 2016) observed a slight reduction (less than 20%) of the retained ultimate strength of FRCM including glass fibers and lime-based matrix. It should be noted that a significant scatter was observed among the results, which indicates the need to perform a large number of tests to make sold conclusions.

Yin et al. (Yin et al., 2019) investigated the effects of wetting in a saline solution (5 wt. % of NaCl) and drying at room temperature on the bond behavior between a cementitious matrix and a hybrid glass-–carbon textile, using a pull-out set-up. Since the effect of drying is considered, these test results are not reported in Figure 2-8. However, no significant difference in the maximum pull-out load was observed after 90 and 120 cycles. Nevertheless, a specific degradation was observed after 150 cycles due to the crystallization of the salt that affected the matrix-fiber interface.

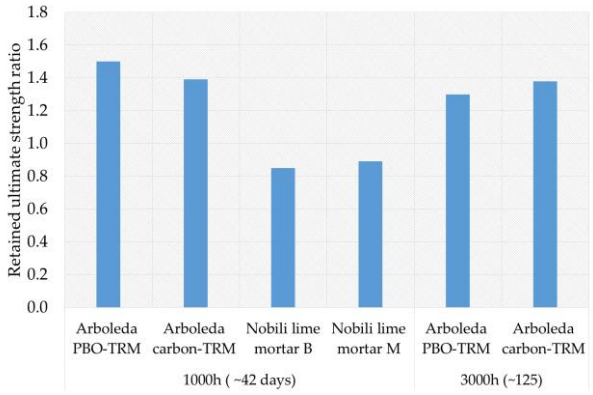

Figure 2-8: Effect of immersion in saline solutions on the retained ultimate strength of fabric-reinforced cementitious matrix (FRCM) coupons.

The effect of moisture and wet-dry cycles on the bond capacity can be controversial. For not entirely hydrated matrix, they can be beneficial due to the continuation of the hydration process (Ceroni et al., 2018; Franzoni et al., 2017). However, it should be noted that the continuation of the hydration process can cause densification of the matrix next to the multi-filament yarn with the penetration of hydration products to the voids among the filaments, which may lead to reduce the matrix–fiber bond properties (De Munck et al.,

2018). More studies are needed to identify the dominant effect among these two competing factors.

For a completely hydrated matrix, moisture and wet-dry cycles may not directly affect the bond behavior. However, they may damage the fibers (e.g., corrosion of steel cords or swelling of glass fibers (Donnini, 2019; Franzoni et al., 2018)) and the matrix (i.e., expansion of water within the pores) and subsequently lead to a decrease of the matrix–fiber bond properties (Ceroni et al., 2018; Franzoni et al., 2018).

The stress transfer between the fiber and matrix can also be influenced by the alkalinity of the matrix, as mentioned in Section 2.3.2. Butler et al. (Butler et al., 2009, 2010) utilized pull-out tests and uniaxial tensile tests to investigate the effect of the matrix alkalinity on the bond between cement-based matrices and AR-glass fibers. Specimens were aged in a humid chamber at 40 °C and 99% RH. One year of this condition was assumed to be equal to 50 years of exposure to the middle European climate. Three cementitious matrices with different levels of alkalinity and hydration kinetics were employed. The low alkalinity matrix (M1) had a pH of 12.4 at the mixing time, which gradually reduced to 11.8 after 1 year. The pH of the high alkalinity matrix (M3) was 12.7. For the medium alkalinity matrix (M2), the pH value was between M1 and M3. The results of unconditioned specimens showed that the maximum pull-out force of specimens made with a high alkalinity matrix (M3) was higher than the others due to the fast hydration process and homogeneous structure of calcium silicate hydrate (CSH) phase close to the fiber. However, an opposite trend was observed after aging. Figure 2-9a shows the behavior of the maximum pull-out force, which progressively decreased with the proceeding of the aging period. The reduction was higher for specimens with matrix M2 than with matrix M1. Results of specimens with matrix M3 are not shown in Figure 2-9a because they failed at the formation of the first crack without slippage of the fibers within the matrix.

The retained ultimate strength of corresponding FRCM coupons subjected to uniaxial tensile test is shown in Figure 2-9b. The behavior observed is consistent with that of pull-out tests, with the exception that the ultimate strength of the coupons made with matrix

M1 increased after 30 days of aging due to the continuation of the matrix hydration process.

Finally, all the studies discussed in this section are summarized in Table 2-6.

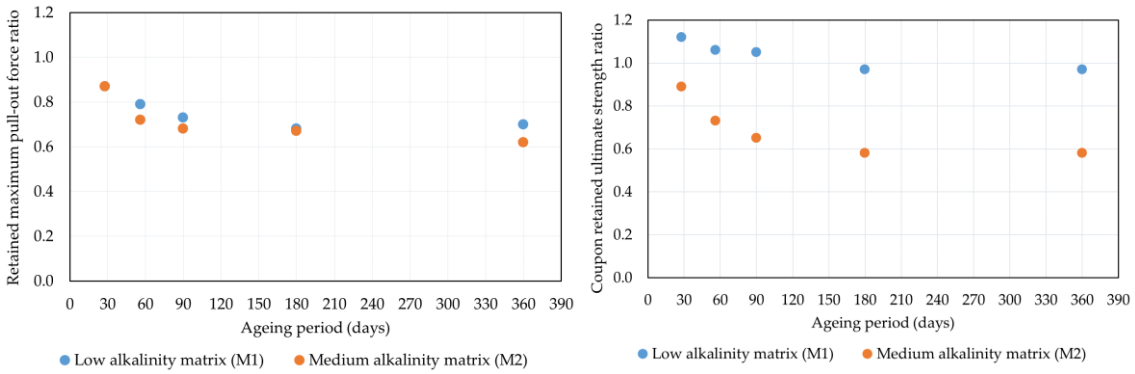

(a) *(b)*

Figure 2-9: Effect of the matrix alkalinity on the (a) maximum pull-out force and (b) ultimate tensile strength of the FRCM coupons tested by Butler et al.(Butler et al., 2009, 2010).

2.3.4 Durability of the composite–substrate interface

Being employed as externally bonded reinforcements, FRCM can be deboned at the composite-substrate interface. However, a limited number of studies dedicated to investigating the durability of the composite–substrate bond are available in the literature.

Sulfate attack can reduce the adhesion between the composite and substrate, degrading the composite–substrate interface (Donnini, 2019; Franzoni et al., 2017). Salt crystallization within the interface can also reduce the bond capacity and shift the failure from the matrix-fabric interface to the composite-substrate interface (Donnini, 2019; Franzoni et al., 2018). Figure 2-10 shows the effect of sulfate attack on the load-carrying capacity of FRCM-masonry joints subjected to direct-shear tests. Donnini et al. (Donnini, 2019) exposed FRCM–masonry joints with an AR-glass textile and a lime-based matrix to 10 wet-dry cycles in saline solution of sodium chloride (3.5 wt. % of NaCl) at 60 °C. After conditioning, the specimens failed at the composite–substrate interface, and the load-carrying capacity was reduced. Franzoni et al. (Franzoni et al., 2017) studied an

SRG composite made of a lime-based matrix and steel cords externally bonded to masonry blocks. They found that four wet-dry cycles in a saline solution containing 8 wt. % of sodium sulfate decahydrate ($Na_2SO_4 \cdot 10H_2O$) followed by drying at 60 °C did not have a significant effect on the load-carrying capacity. Besides, all the specimens developed interlaminar failure characterized by fiber slippage from the internal layer of the matrix, which remained bonded to the substrate. However, when 2 wt. % of sodium chloride (NaCl) was added to the same solution, and the number of cycles increased to 6, the load-carrying capacity decreased.

Finally, the reduction in the bond capacity and shifting of the failure mode to the composite–substrate interface require a high salt accumulation and crystallization within the interface, which may depend on the porosity of the matrix and the radius of the pores. For instance, a matrix with a pores radius bigger than the radius of substrate pores will allow the solution to pass through it. Consequently, the effect of sulfate and saline attack on the interface may not be as significant as its effect on the fibers and matrix (Franzoni et al., 2017). However, this hypothesis needs to be confirmed by using matrices with different porosity and pore sizes.

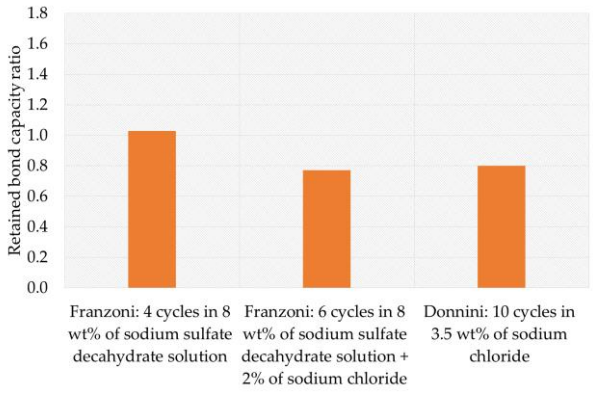

Figure 2-10: Effect of sulfate attack on the load-carrying capacity of steel-reinforced grout (SRG)–masonry (Franzoni et al., 2018, 2017) and FRCM–masonry (Donnini, 2019) joints.

Table 2-6: Effect of the aging environments on the FRCM coupons and FRCM-substrate

Authors	Materials	Exposure conditions	Tests	Results in term of the average ultimate retained strength	Comments
Colombo et al., (Colombo et al., 2015)	• AR-glass FRCM made of cementitious matrix	• FT (ASTM C666, 2015) (25-500 cycle): 30 min at +4, 30 min at -18 and cooling/heating rate was11^{o}C/h	• Uniaxial tensile test on the TRC coupon	• Retained ultimate tensile strength of the coupons exposed to 25, 50, 75, 100, 150 and 500 cycle was 1.03, 0.96, 0.98, 0.89, 0.86, and 0.81, respectively.	• No significant reduction within the few cycles.
De Munck et al., (De Munck et al., 2018)	• AR-glass FRCM made with a cementitious matrix	• FT: 100 cycles with a temperature range of (-20 to 20) (BS EN 12467, 2004) • Heat-rain (HR) of 50 cycles: heating to 60^{o}C within 15 min and maintained for 45 min then cooled with water immersion in 15^{o}C. • Combined effect of the two previous environments with 100 cycle FT	• Uniaxial tensile test on FRCM coupon	• Retained ultimate tensile strength of the specimens exposed to FT was 0.84 • Retained ultimate tensile strength of the specimens exposed to HR was 0.58 • Retained ultimate tensile strength of the specimens exposed to the combined effect	• The reduction in the ultimate tensile strength was attributed to the formation of the precipitates of the hydration process.

		followed 50 cycle heat-rain		of FT and HR was 0.73	
Arboleda (Arboleda, 2014)	• PBO FRCM made with cementitious matrix • Carbon FRCM made with cementitious matrix	• CC: 100% RH at 37.7°C for 1000-3000 hour • FT: 20 cycles with 4 hours at -18°C and 12 hours at 37.7°C and 100% RH • Saline: (seawater) • Immersion in alkaline solution [$Ca(OH)_2$, KOH, NaOH] with pH>12	• Uniaxial tensile test on FRCM coupon	• FT: retained ultimate tensile strength of the FRCM made of PBO fiber was 1.1 • Saline: retained ultimate tensile strength of the PBO FRCM after 1000h of exposure was 1.5; however, this value became 1.3 when the exposure period increased to 3000h • The retained ultimate tensile strength of the FRCM made of carbon was increased by 13% in CC and alkaline environments.	• Results are characterized by an obvious scatter value. Consequently, a one-way ANOVA analysis was performed. • The results of ANOVA analysis showed that CC and Alkaline environments did not have a significant effect on the FRCM composite made of PBO. The results of the ANOVA analysis showed that retained strength of the FRCM made of the carbon was not significantly affected by the FT and Saline environments.
Pekmezci et al., (Pekmezci	• FRCM coupons made of biaxial	• FT: 14 cycles of 2 hours in water at 20°C and 6 hours	• Uniaxial tensile test on FRCM coupon	• Retained ultimate strength for the coupons	• Comparing the results of the two systems showed that

et al., 2019)	glass fabric and lime-based matrix • FRCM coupons made with quad axial hybrid fabric and lime matrix	at -25°C in the freezer		made of the biaxial glass fabric was 0.84. • The retained ultimate strength of the coupons made of the hybrid fabric was 0.99	using biaxial fabric has Improved the tensile strength more than the quad axial hybrid fabric. However, exposing both systems to the FT cycles led the first system to lose part of its strength. This difference in performance was attributed to the configuration of the fabric used in each system.
Butler et al. (Butler et al., 2010)	• AR-glass fiber • Three types of concrete (M_1, M_2, M_3) with different level of alkalinity	• Aging period: 28-360 days • M_1 concrete: low alkalinity (reduced from pH = 12.4 at mixing to pH= 11.8 after 1 year). • M3 concrete: high alkalinity of pH=12.7 • M2 concrete: with a medium level of alkalinity ranging between M1 and M3	• Pull-out test	• Retained maximum pull-out forces for matrix M_1 at period of 28, 56, 90, 180 and 360 are 0.87, 0.72, 0.68, 0.67 and 0.62, respectively. • Retained maximum pull-out forces for matrix M_2 at the same periods are 0.87, 0.72, 0.68, 0.67 and 0.62	• Results of the reference specimens indicated a pronounced increment in the bond strength between the fiber filaments and M_2 and M_3 matrices. However, exposing the specimens to aging environments leads to a pronounced reduction in the maximum load, especially in the case of M_3, where some specimens developed a brittle failure within the

					fiber with the proceeding of the aging process.
Nobili (Nobili, 2016)	• AR-glass FRCM coupon made with matrix B (rich in hydrated lime and pozzolan) • AR-glass FRCM coupon made with matrix M (air-hardening lime, pozzolan, and marble sand)	• Immersion in alkaline solution (Sodium bicarbonate, pH=10) for 1000 hour • Immersion in saline solution (3.5% sodium chloride) for 1000 hour	• Uniaxial tensile test on FRCM coupon	• Alkaline: retained ultimate strength of the coupons made of matrix B and M is 0.89 and 0.90, respectively. • Saline: retained ultimate strength of the coupons made of matrix B and M is 0.85 and 0.89, respectively.	• Reduction in the ultimate tensile strength for the system made of the matrix B • Failure mode was shifted from fiber rapture in the control specimens to fiber slippage within and delamination within the matrix-fiber interface for the conditioned specimens.
Yin et al., (Yin et al., 2019)	• FRCM coupons made of hybrid fabric (carbon bundles were warp and E-glass bundles as weft) impregnated with epoxy resin. • The matrix used to make the TRC coupons was a cement-based matrix	• Combined effect of FT (50, 70, and 90 cycles with 3 hours cycle length and a temperature range between -18°C to 5°C) and saline environment (5 wt% NaCl)	• Pull-out test	• Retained ultimate pull-out strength after exposing to 50, 70, and 90 cycles was1.0, 0.98, and 0.99, respectively	• No apparent effects on the pull-out strength

Ceroni et al., (Ceroni et al., 2018)	• PBO FRCM made of cementitious matrix	• WI at 23°C for 5, 9, 40, and 74 days • WI at 30°C for 9 and 74 days • WI at 40°C for 4 days • CC at 30°C for 9 days	• Three-point bending test on small concrete beams strengthened with FRCM. Tests were done in an environment-controlled room with the same temperature and humidity specimens exposed to	• 1st condition: 0.57, 0.77, 0.96 and 1.12 respectively. • 2nd condition: 0.6 and 1.014 • 3rd condition: 0.73 • 4th condition: 0.72	• Reduction in the bond strength for the short exposure periods; yet, as the exposure period was increased, the reduction in the bond strength decreased. Moreover, for more extended aging periods (74 days), the bond was improved.
Donnini et al., (Donnini, 2019)	• AR glass FRCM and masonry substrate • Lime based matrix	• WI: tap water at 60°C for 1000h • Immersion in saline solution (3.5% NaCl) at 60°C for 1000h • WD 10 cycles (960h): 2 days immersion in saline solution (3.5% NaCl) at 60°C and 2 days drying at 60°C	• Single-lap shear test on FRCM bonded to a masonry substrate	• WI: average ultimate retained strength was 0.89 • Saline: 0.71 • WD: 0.8	• For WI: failure was developed in the matrix-fiber interface. • Saline: failure occurs within the glass fiber out of the bonded part. • WD: Failure was developed in the matrix-substrate interface.
Franzoni et al., (Franzoni et al., 2018, 2017)	• SGR composite made of lime-based matrix and steel cords bonded to a	• WD: 4 cycles of 2 days of partial immersion in a saline solution (8% wt of	• Single-lap shear test on masonry substrate	• 1st aging condition: 1.03 • 2nd aging condition: 0.98	• All the specimens exposed to the 1st and 2nd aging conditions developed a failure

masonry substrate	$Na_2SO_4.10H_2O$) and 2 days drying in a ventilated oven at 60ºC. • WD: 4 cycles of 2 days immersion in deionized water and 2 days drying in a ventilated oven at 60ºC • WD: 6 cycles of days partially immersed in saline solution (2% wt of NaCl and 8% wt of $Na_2SO_4.10H_2O$) at 20ºC and 3 days drying with ventilated oven at 60ºC • WD: 6 cycles similar to the previous condition; yet, denoised water was used for drying instead of the saline solution •	• 3rd aging condition: 0.73 • 4th aging condition: 0.78	within the matrix-fiber interface (between the internal layer of the matrix and fiber). • Most of the specimens exposed to the 3rd and 4th aging condition developed a mixed failure mode in the matrix-fabric interface and matrix-substrate interface. However, one specimen exposed to the 4th aging condition developed a brittle failure in the matrix-substrate interface only. •

Chapter 3: Durability of CFRP-concrete joints under the effect of water and temperature

The literature reviewed in the second chapter revealed that more studies are needed to have a deeper understanding of the durability of the CFRP. This chapter contains two main parts. The first one focused on the effect of the hygrothermal environment on the bond durability of the CFRP-concrete joints and constituent materials. However, the second one is dedicated to evaluating the effect of the wet-dry cycles on the durability of the CFRP-concrete joints.

3.1 Conditioning environments

Two conditioning environments were utilized in this chapter. The first condition was a hygrothermal environment and utilized to evaluate the durability of the CFRP-concrete joints and constituent materials (CFRP coupons and epoxy resin specimens). The second condition was wet-dry cycles and utilized to investigate the durability of the CFRP-concrete joints.

3.1.1 Hygrothermal condition

In this condition, the specimen was immersed in water at 38 ± 2 ºC. The exposure temperature was chosen based on the recommendations of Blackburn et al. (Blackburn et al., 2015), CNR_DT_200 (CNR, 2013)c, and ACI 440.2R-08 (ACI Committee 440.2R-8, 2008). Blackburn et al. (Blackburn et al., 2015) recommended performing accelerated aging by water immersion at the maximum temperature expected in the field, whereas ACI 440.2R-08 specifies a maximum service temperature equal to Tg-15°C. Since the glass transition temperature of the resin used in this study was Tg = 58°C (Sika, 2017a), an exposure temperature of 38 ± 2^{o}C was selected. Water immersion was adopted instead of a humid environment to increase the aging rate (Ceroni et al., 2018; Jovan Tatar & Hamilton, 2016). It should be noted that water immersion may provide aging conditions different from those of humid environments, but it is generally assumed to induce more degradation than exposure to humid environments (T. D'Antino et al., 2018). Blackburn et al. (Blackburn et al., 2015) recommended eight weeks (i.e., 1344 h) of aging to balance

the competing effect between post-cure and plasticization. Nevertheless, three exposure periods of 500, 1000, and 1500 hours are inspected in the current study to have a clear understanding of the aging effect. These exposure periods were selected by decreasing and increasing of 500 hours of the minimum exposure period (i.e., 1000 hours) recommended by the American acceptance criteria (International Code Council (ICC), 2014) and Italian initial type testing procedure (CSLLPP, 2015) for FRP composite.

3.1.2 Wet-dry cycles

Generally, there is no standard method to perform wet-dry cycles. Most of the studies in the literature (M. I. Kabir, Ph, et al., 2016; Shrestha et al., 2015; M. A. G. Silva & Biscaia, 2008; Tuakta & Büyüköztürk, 2011) have adopted lab tests to determine the period required to moisturize and dry the specimens. For instance, Kabir et al. (M. Kabir, Samali, & Shrestha, 2016) performed wet-dry cycles composed of 1 week of wetting at 95% RH followed by 1 week drying at the room environment (20-23 ^{o}C) on CFRP strips externally bonded to concrete prisms. Shrestha et al. (Shrestha et al., 2015) did 7 days of immersion in water followed by 4 days of drying at room temperature (20 ^{o}C).

In the current research, a specific system was manufactured to perform wet-dry cycles, as shown in Figure 3-1a. The system is composed of two water containers. One of them was placed inside a drying chamber while the other one was left outside the chamber in the lab environment at 25 ^{o}C. The two containers were connected by two pumps to transfer the water between them, which was tap water. The pumps were controlled using timers to open them and close them at a specific time of the day. The specimens were placed in the container inside the chamber (Figure 3-1a).

In the current research, the specimens were exposed to 50 wet-dry cycles that were chosen to simulate the bond performance of CFRP strip externally bonded to the intrados of a bridge that gets wet twice a year by floods during the life span of the CFRP strip, which is estimated to be 25 years. It is worth mentioning that other standards like EN 12467 (BS EN 12467, 2004) have also recommended performing 50 cycles to investigate the durability of the fiber-cement sheets. Each cycle consisted of 6 hours of immersion in water followed by 18 hours of drying. The length of the wetting and drying periods was

selected after performing some tests to determine the period required to moisturize and dry them (see section 4.2 for more details).

The relative humidity inside the chamber was fixed to 50% during the wetting phase to speed the moisturizing process and 20% during the drying phase to speed the drying process. The temperature of the chamber was ranging between 25 ^{o}C during the wetting phase and 50^{o}C during the drying phase, as shown in the red curve of Figure 3-1b. The temperature in the container where the specimens were placed was also monitored using a thermocouple and shown with a blue curve line of Figure 3-1b. It can be noticed that the temperature inside the container was higher than the temperature in the chamber during the wetting phase since the specimens were still warm from the drying phase; however, the reverse is valid during the drying phase because they were still wet.

The drying temperature (i.e., 50 ^{o}C) was selected to satisfy three criteria: (1) it is relatively high that it can accelerate the drying process and allow to perform more cycles with a shorter period; (2) it is lower than T_g of the epoxy resin (T_g= 58 ^{o}C); (3) it can simulate the temperature found in the façade of the actual building due to the solar radiation, the temperature of the surfaces can reach to 40-60 ^{o}C in the European climate during summer and in some extreme cases to 80^{o}C (Franzoni et al., 2017; Luque, Ruiz-Agudo, Cultrone, Sebastián, & Siegesmund, 2011).

(a)

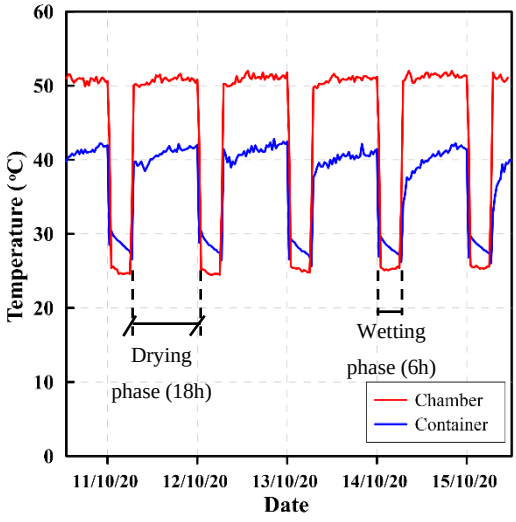

(b)

Figure 3-1: wet-dry condition (a) system used to perform the condition, (b) wet-dry cycles

3.2 Mechanical characterization of constituent materials

This part of the experiment investigates the effect of hygrothermal aging on the mechanical characteristics of the epoxy resin and CFRP coupon. It consists of two groups. The first group has twenty dumbbell-shaped specimens of epoxy resin, while the second group consisted of twenty rectangular CFRP coupon specimens. Out of these twenty

specimens, five were used as control specimens while the remaining were exposed to the hygrothermal condition, five specimens for each exposure period.

3.2.1 Epoxy resin

Two components epoxy resin (Sika, 2017a) was used in this study. T_g was 58^{o}C, as reported by the manufacturer. Dumbbell shape specimens were made by pouring the resin inside a plastic mold that was made using a laser cutting machine. The mold surface was covered with oil to ensure ease of removal of the specimens and not damaging the mold. Since the thickness of the dumbbell specimens was higher than the thickness of the resin used in the standard bonding joint, special attention was given through the process of preparing to prevent forming of the air bubble. However, still, some tiny bubbles could be noticed after testing. The mold was removed after two days. Specimens were left to cure for at least two weeks in the laboratory conditions before exposing to the hygrothermal environment. Figure 3-2 shows specimen configuration.

A uniaxial tensile test was performed according to ASTM D638 (ASTM D638-03, 2004). Five specimens were tested for each exposure period. Tests were performed using a displacement control Instron machine. ASTM D638 recommended that the test should last from 1/2 to 5 minutes before developing rupture. Therefore, numerous speeds were inspected to satisfy this criterion. Finally, a displacement rate of 1 mm/min was adopted. A clip gauge of 25mm was attached to the middle of the specimens to record the strain. The elastic modulus was determined from the stress-strain curves as the slope of the chord between 25% and 50% of the maximum tensile stress.

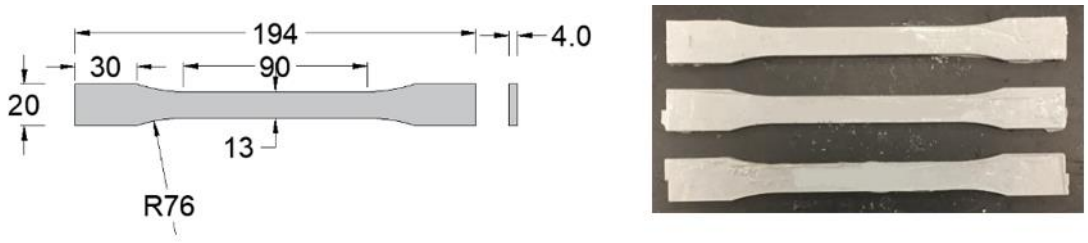

Figure 3-2: Geometry configuration of the Dumbbell resin specimen

3.2.2 CFRP coupon

A unidirectional carbon textile of (Sika, 2017b) was used in this study. The thickness of the textile was 0.166 mm. The CFRP coupon specimens were prepared on a flat mold. The preparation procedure included: (1) applying one layer of epoxy resin, (2) placing carbon fiber textile of 300x20 mm, (3) applying another layer of the resin. The curing period lasted at least two weeks. At the end of the curing period, the CFRP coupon was cut based on the dimension specified by the European standards (BS EN 2561, 1995). Finally, tabs made of glass fiber plates are attached to the ends of the CFRP coupon, as shown in Figure 3-3.

Five specimens were tested for each exposure period. The tests were performed using an Instron machine with a displacement rate of 2 mm/min. A clip gauge of 100 mm was used to monitor the strain. Since it is challenging to estimate fiber volume fraction in the wet layup technique, the tensile strength, and modulus of elasticity were reported as equivalent to the bare fiber cross-sectional area based on the hypothesis that tensile load is resisted by fibers, as explained in the (BS EN 2561, 1995) . Similar to dumbbell tests, modulus of elasticity was determined from the stress-strain curve as the slop of the chord between 10% and 50% of the maximum tensile stress.

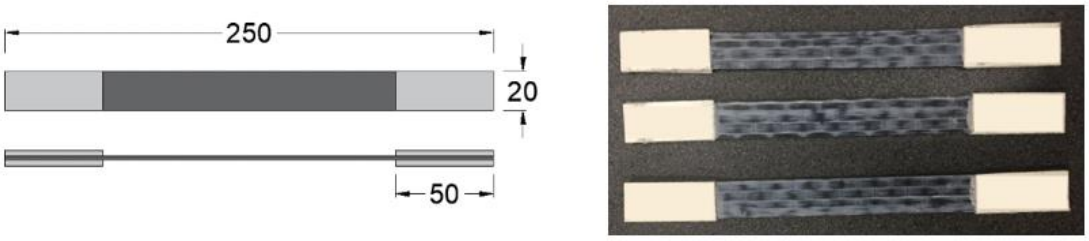

Figure 3-3: Geometry and configuration of the CFRP coupon

3.3 CFRP-concrete joints

External strengthening of the deteriorated concrete members with CFRP has been widely used in the last few decades. Stress transfers from the concrete substrate to the CFRP mainly through the bond. During its lifetime, CFRP-concrete joint is exposed to various

environmental conditions; however, hygrothermal and wet-dry environments are considered critical environments as reported in the literature (Maljaee et al., 2017; Sen, 2015). Consequently, the bond behavior of the CFRP-concrete joint under these two environmental conditions is an essential quality for the service life design.

In this part of the experiment, the effect of the hygrothermal and wet-dry conditions on the bond durability of the CFRP-concrete interface is investigated by performing 26 single-lap direct-shear tests (16 for hygrothermal and 10 for wet-dry cycles) and 16 pull-off tests (only for hygrothermal).

3.3.1 Specimen geometry and assembly

Thirteen concrete prisms of dimensions 100 mm x 100 mm x 250 mm were cast in two batches using a wooden mold, as shown in Figure 3-4a. The prisms were left in the wooden mold for 28 days and inside the lab environment (25 ^{o}C).

Eight prisms were made of the first batch, which was utilized to investigate the effect of the hygrothermal condition on the CFRP-concrete joints. The compressive strength of the first batch was measured on 150×150×150 mm cubes cast from the same batch (EN, 2009, 2012). It was measured at the same week that the direct-shear test was performed, and it was 26.32 MPa. Five prisms were made of the second batch and used to study the effect of the wet-dry condition on the CFRP-concrete joints. The compressive strength of the second batch was evaluated on 100 x 100 x 100 mm cubes cut from the prisms utilized for the single-lap direct-shear test. The is method was utilized to accurately evaluate the effect of the wet-dry conditions on the compressive strength of the prisms, as going to be noticed in section 3.4.4.2. The compressive strength of the second batch was 38 MPa.

CFRP strips were applied on the concrete prisms in a specific way to allow the performance of two single-lap direct-shear tests for each concrete prism. The two side faces (i.e., the faces adjacent to the casting face) of each prism were externally bonded with CFRP strips, as shown in Figure 3-4b. The bonded length and width of the CFRP strip were 200 mm and 50 mm, respectively. The strip was left unbonded for 30 mm from the edge of the specimen to prevent edge failure of the concrete prism as shown in Figure

3-4c. The CFRP strips were bonded on the concrete surface based on the following procedure (Al-Tamimi et al., 2015; American Concrete Institute, 2017; Sika, 2017b):

1. Roughening of the surface with steel brush and sandpaper.

2. Removal of dust and loose particles with an air jet.

3. Application of one layer of resin onto the prism surface using a spatula.

4. Application of the carbon fiber sheet of dimension 300 mm length and 50 mm width over the resin, promoting the fiber impregnation using a roller.

5. Application of a covering layer of resin over the carbon fiber sheet using a roller.

The specimens were cured for at least two weeks in laboratory conditions (23 ± 2 °C) before starting the hygrothermal aging

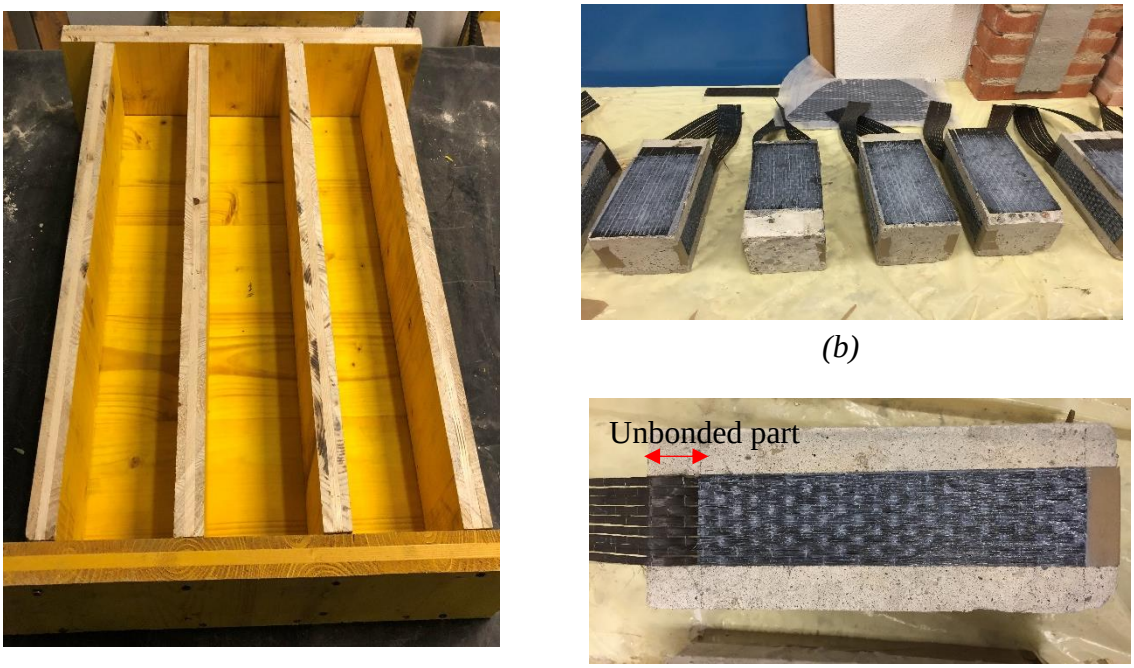

(a) *(b)* *(c)*

Figure 3-4: specimens' preparation (a) wooden mold, (b) concrete specimens bonded with CFRP, (c) unbonded length of the single-lap direct-shear test

The bottom faces (i.e., the face opposite to the casting face) of the prisms made of the first batch were also externally bonded with CFRP strips of the dimensions 70 mm x 200 mm,

as shown in Figure 3-4b. These CFRP-concrete joints were utilized to evaluate the effect of the hygrothermal condition on the pull-off strength (bond strength).

3.3.2 Testing procedure and test setup

Pull-off tests were performed according to the ASTM D4541 (ASTM D4541 – 09, 2009). Two circular grooves with 50 mm external diameter were drilled through the CFRP strip and along the concrete substrate using a coring tool. After that, aluminum testing disks were glued to the CFRP within the grooves border using the same two-component epoxy resin employed to apply the CFRP sheets. The resin was cured for two days before performing a pull-off test. Figure 3-5 shows the geometry of the specimens and the execution of a pull-off test.

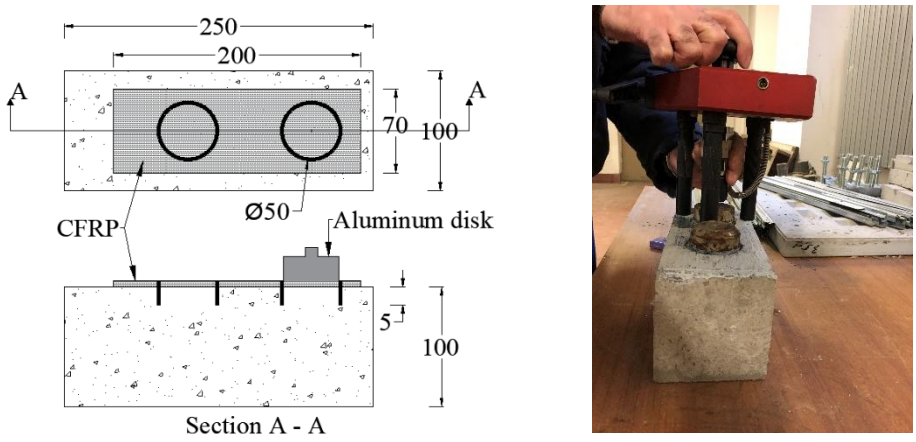

Figure 3-5: Pull-off test (demission in mm)

Figure 3-6 shows the single-lap direct-shear test setup. The adopted bond length (i.e., 200 mm) was higher than the effective bond length determined according to the CNR-DT 200 R1/13 (CNR, 2013). The load was applied at the end of the CFRP strip using a universal testing machine under displacement control. Two speeds were adopted: 0.2 mm/min and 0.05 mm/min. Although changing speed test did not have a significant effect on the bond characteristics of the CFRP-concrete joint, the slower speed allowed to precisely monitor the debonding process with the DIC technique (Ali-ahmad, Subramaniam, & Ghosn, 2006). Two linear variable differential transducers (LVDTs) were attached to the concrete surface at the CFRP loaded end to measure the relative displacement (i.e., the slip)

between the concrete and the CFRP sheet at the loaded end. The LVDTs reacted off a thin Ω-shaped aluminum plate glued to the CFRP sheet at the loaded end. The average displacement measured by the two LVDTs is named global slip, *g*, in this research. A two-dimensional digital image correlation method was employed to obtain the displacement field on the CFRP sheet bonded surface.

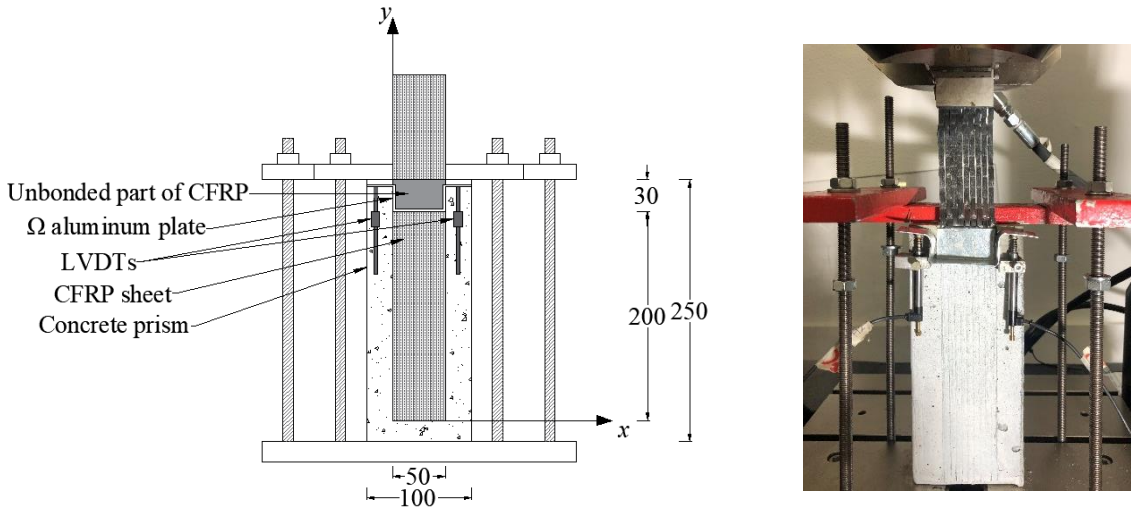

Figure 3-6: single-lap direct-shear test setup (demission in mm)

3.4 Results and discussion

3.4.1 Epoxy resin

Twenty specimens were tested in this part of the experimental program. Five specimens were tested without being exposed to the hygrothermal environment and consider as control specimens. The other fifteen specimens were tested after being immersed in water at 38±2°C for 500, 1000, and 1500 hours. Five specimens were tested for each exposure period. The specimens were named following a specific system. Each name consists of four parts. The first part refers to the specimen's type (D: Dumbbell specimens of the resin). The second part refers to the type of conditioning environment (H: Hygrothermal). The third part refers to the conditioning period (0: no conditioning, 500 hours, 1000 hours, and 1500 hours). The last part refers to the number of specimens within the group.

The effect of the hygrothermal aging on the epoxy resin was evaluated based on the changes in the external appearance, weight, and mechanical properties. After being conditioned, a thin and sticky layer was formed on the external surfaces of the specimens. The formation of this layer, which vanished after drying, can be attributed to the plasticization (Cabral-fonseca et al., 2018; Tuakta & Büyüköztürk, 2011). The specimens' color was also changed from dark grey into light gray, as shown in Figure 3-7a. Changing the epoxy color after the condition was also reported by (Au, 2005). Local deformation was noticed in some specimens after drying, as shown in Figure 3-7b. This deformation can be ascribed to the contraction and expansion of the specimens stimulated by the conditioning environment. Regarding weight changes, the weight of the specimens was recorded before and immediately after the exposure. Some of the specimens showed a slight increment, around 3%, which can be attributed to water absorption.

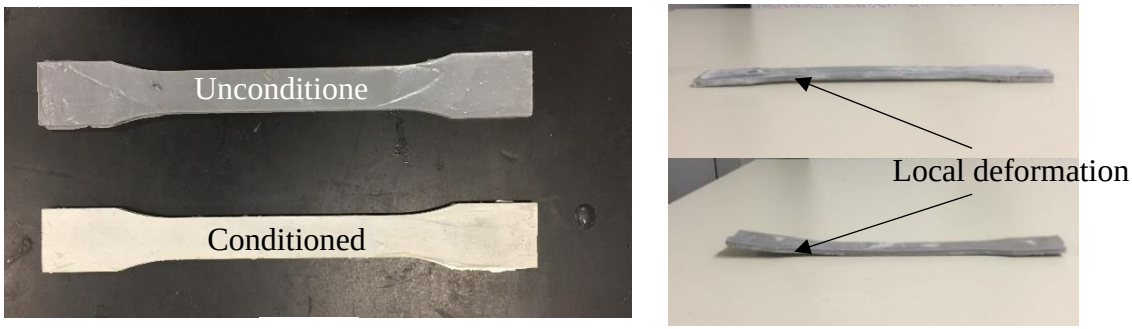

(a) *(b)*

Figure 3-7: changes in the epoxy resin due to the aging; (a) color change; (b) local deformation formation

Figure 3-8 shows the effect of the hygrothermal environment on the stress-strain relationship. It can be noticed that the general behavior has been slightly changed from brittle to ductile behavior. Moreover, the values of the strain and stress were increased for most conditioned specimens in comparison with the control specimens. However, the stiffness of most conditioned specimens was slight decreased in comparison with control specimens. A similar finding was also obtained by Shrestha et al. (Shrestha et al., 2015).

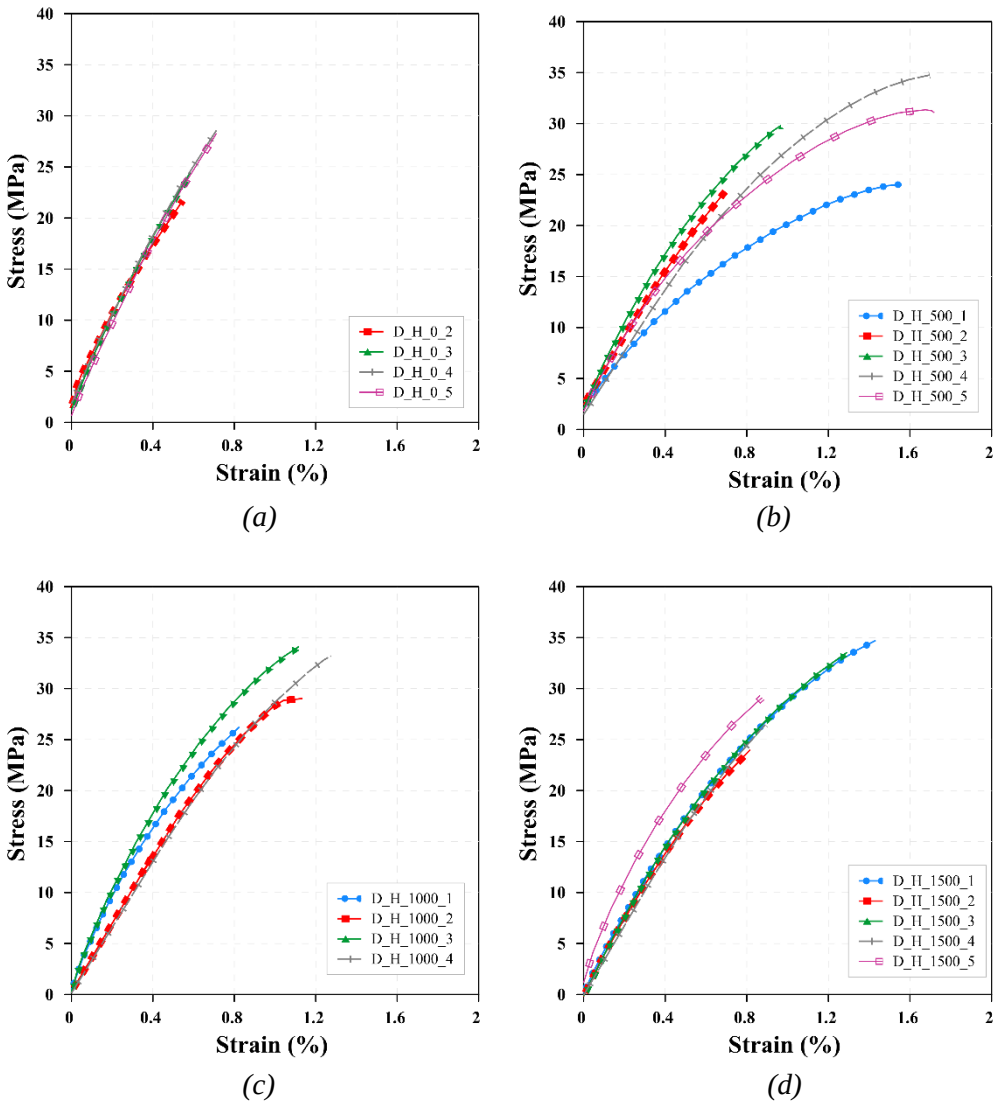

Figure 3-8: Stress vs. strain curves for the dumbbell specimens of the epoxy resin (a) control specimens, (b) specimens conditioned for 500 hours, (c) specimens conditioned for 1000 hours, (d) specimens conditioned for 1500 hours.

Figure 3-9a presents the effect of the hygrothermal environment on the average ultimate tensile strength and strain. The scatter of the data was presented as an error bar. The coefficient of variation (CoV) for the average ultimate strength was around 12% which is within the acceptable range. The average ultimate tensile strength has increased from 25.76 MPa to 27.62 MPa after 500 hours of conditioning. The increase in the ultimate strength has continued until it reached the peak value of 30.66 MPa after 1000 hours of

conditioning. After that, it slightly decreased to 29.61 MPa at 1500 hours. Regarding the average ultimate strain, it is significantly increased to 1.33% after 500 hours of conditioning; then, it slightly decreased to 1.27% and 1.12% after 1000 and 1500 hours, respectively. CoV was between 16% and 22%.

The effect of the hygrothermal environment on the average elastic modulus is presented in Figure 3-9b. CoV was in the range of 3%-7%. Elastic modulus has decreased from 4.22 GPa to 3.15 GPa after 500 fours of conditioning; subsequently, it is increased to 3.69 GPa and 3.74 GPa after 1000 hours and 1500 hours of conditioning, respectively. The contrary effect of moisture on tensile strength and elastic modulus was also reported by Shrestha et al. (Shrestha et al., 2015). It is believed that exposing resin specimens to hygrothermal aging conditions triggers both the harmful effect of plasticization and swelling and the beneficial effect of post-curing (Blackburn et al., 2015).

Finally, the effect of the hygrothermal condition on the mechanical properties of the epoxy resin is summarized in Table 3-1. The results of the specimens D_H_0_1 and D_H_1000_5 are not reported because the failure was developed close to the tabs (out of the gauge region).

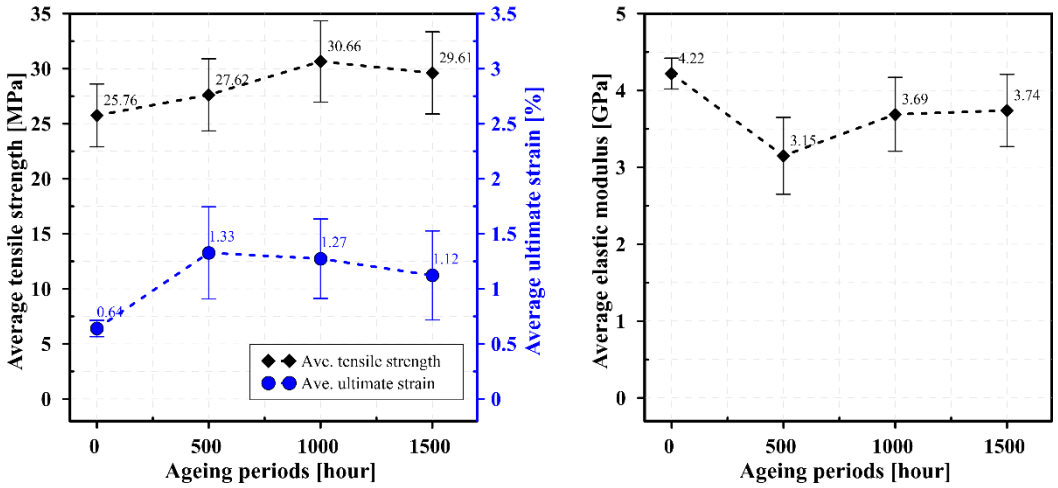

(a) *(b)*

Figure 3-9: Effect of the hygrothermal environment on the average ultimate mechanical properties of the epoxy resin, (a) tensile strength and strain, (b) elastic modulus

Table 3-1: Mechanical characterization of the epoxy resin

Specimen Name	Aging period (hours)	Ultimate strength (MPa)	Ultimate strain (%)	Modulus of elasticity (GPa)	Notes
D_H_0_1	0	NA	NA	NA	Failure developed out of the gauge area
D_H_0_2		21.71	0.55	3.92	
D_H_0_3		24.47	0.58	4.47	
D_H_0_4		28.58	0.71	4.22	
D_H_0_5		28.28	0.71	4.25	
D_H_500_1	500	24.05	1.56	2.35	
D_H_500_2		23.33	0.69	3.33	
D_H_500_3		29.76	0.97	3.89	
D_H_500_4		29.61	1.70	3.05	
D_H_500_5		31.36	1.72	3.12	
D_H_1000_1	1000	26.24	0.82	4.03	
D_H_1000_2		29.03	1.34	3.34	
D_H_1000_3		34.13	1.12	4.16	
D_H_1000_4		33.24	1.81	3.21	
D_H_1000_5		NA		NA	Failure developed out of the gauge
D_H_1500_1	1500	34.73	1.96	3.33	
D_H_1500_2		24.00	0.84	3.45	
D_H_1500_3		33.55	1.29	3.45	
D_H_1500_4		26.45	0.89	3.42	
D_H_1500_5		29.11	0.87	4.34	

3.4.2 CFRP coupon

CFRP coupon specimens were named following the same system used for the dumbbell specimens of the epoxy resin with one difference that the first letter of the dumbbell specimens (D) was replaced with (C) referring to the coupon specimens, as shown in Table 3-2. The effect of the hygrothermal environment on the stress-strain relationship is illustrated in Figure 3-10. CFRP coupon showed a linear behavior up to a strain of 0.9%. After this value, the strain was not recorded because the extensometer had to be removed to protect it from the destructive failure of the coupons, as shown in Figure 3-11. Nonetheless, the value of the ultimate strain was estimated as the ratio of the ultimate strength to the corresponding elastic modulus of each specimen. Table 3-2 reports the values of the ultimate strength, strain, and elastic modulus for each specimen.

Figure 3-12a shows the effect of the hygrothermal environment on the average ultimate tensile strength. The standard deviation was shown as an error bar. CoV was in the range of 3-8%. The result shows a slight increment (2%-7%) with the proceeding of the conditioning period. However, since it is within the scatter range of the data, it can be considered insignificant.

The effect of the hygrothermal environment on the average ultimate strain is also shown in Figure 3-12a. CoV was in the range of 3-8%. It can be noticed that the strain was not significantly affected. Figure 3-12b shows the behavior of the elastic modulus. CoV was in the range of 4-6%. Similarly, the results of the elastic modulus indicated no significant change where the maximum change was almost 5%.

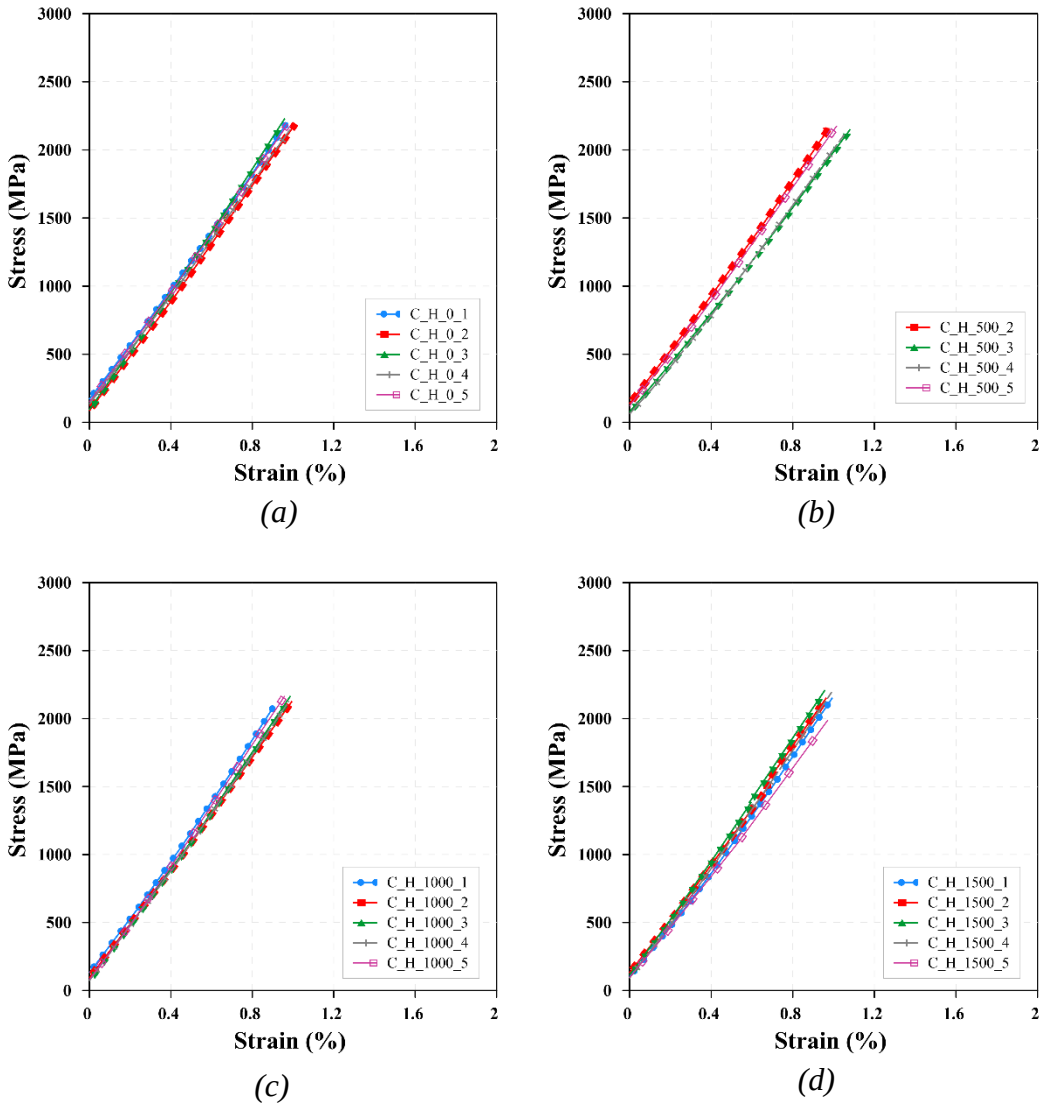

Figure 3-10: Effect of the hygrothermal condition on mechanical properties of the CFRP coupon, (a) control specimens, (b) specimens conditioned for 500h, (c) specimens conditioned for 1000h, (d) specimens conditioned for 1500h

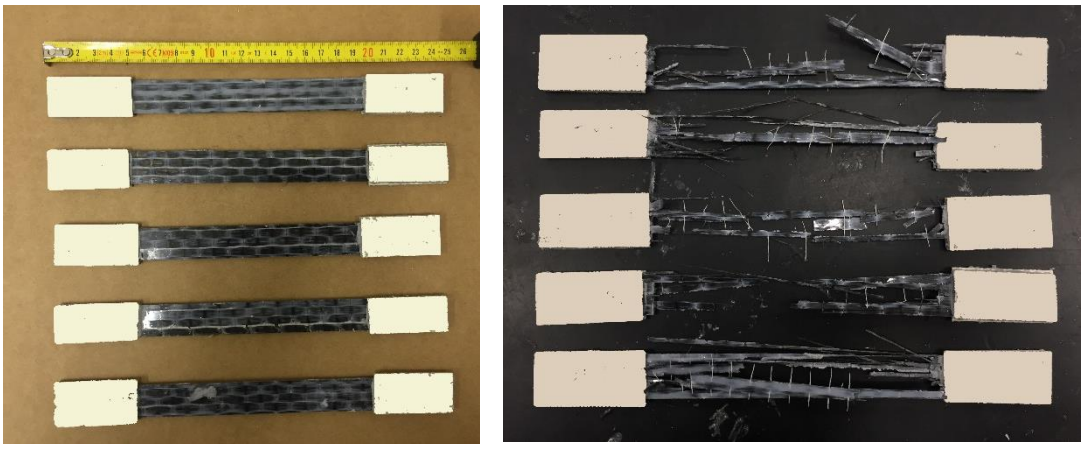

(a) *(b)*

Figure 3-11: Failure mode of the CFRP coupon, (a) before testing, (b) after testing

Table 3-2: Mechanical characterization of the CFRP coupon

Specimen Name	Aging period (hours)	Ultimate strength (MPa)	Elastic modulus (GPa)	Ultimate strain (%)	Notes
C_H_0_1	0	2945	205	1.44	
C_H_0_2		3271	206	1.58	
C_H_0_3		3009	210	1.37	
C_H_0_4		2899	202	1.44	
C_H_0_5		3311	208	1.60	
C_H_500_1	500	NA	NA		Extensometer did not measure the strain
C_H_500_2		3050	204	1.50	
C_H_500_3		3065	190	1.61	
C_H_500_4		3251	197	1.65	
C_H_500_5		3239	202	1.61	
C_H_1000_1	1000	3606	216	1.67	
C_H_1000_2		3218	203	1.59	
C_H_1000_3		3075	209	1.47	
C_H_1000_4		3649	210	1.74	
C_H_1000_5		2935	217	1.35	
C_H_1500_1	1500	3339	211	1.58	
C_H_1500_2		3353	220	1.52	
C_H_1500_3		3552	212	1.68	
C_H_1500_4		3035	193	1.57	
C_H_1500_5		3006	202	1.49	

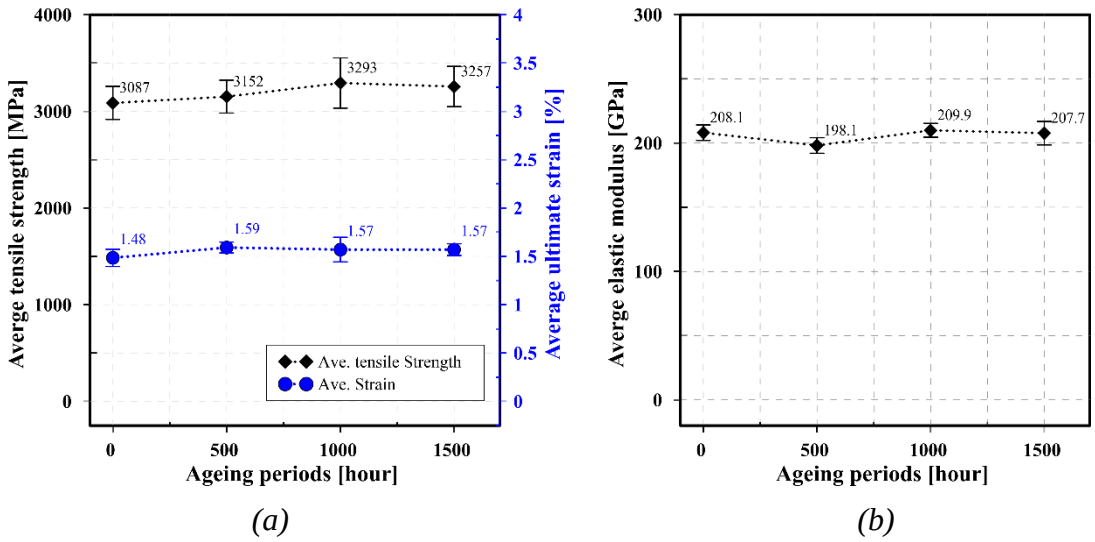

Figure 3-12: Effect of the hygrothermal aging on the mechanical properties of the CFRP coupon; (a) tensile stress and strain; (b) modulus of elasticity

3.4.3 Pull-off strength

The effect of the hygrothermal environment on the bond strength was studied using a pull-off test on control specimens (4 specimens) and conditioned specimens (12 specimens). The specimens were also named following the same system used for the dumbbell specimens of the epoxy resin and discussed in section 3.4.1, with one difference is that the first letter of the dumbbell specimens (D) was changed to (P), referring to the pull-off test as illustrated in Table 3-3.

The hygrothermal condition has changed the color of the CFRP strip from dark gray to light gray, as noticed previously with the epoxy resin specimens. Figure 3-13 compares the failure mode of the conditioned specimens with control specimens. It can be noticed that both specimens have developed a failure within the concrete substrate. This failure mode has been developed in all other specimens.

(a)

(b)

Figure 3-13: Pull-off test, (a) control specimen, (b) conditioned specimen

Table 3-3: Effect of the hygrothermal environment on the pull-off strength

Specimen Name	Aging period (hours)	Pull-off (MPa)
P_H_0_1	0	1.68
P_H_0_2		1.70
P_H_0_3		2.61
P_H_0_4		2.36
P_H_500_1	500	1.62
P_H_500_2		2.16
P_H_500_3		2.45
P_H_500_4		2.23
P_H_1000_1	1000	2.24
P_H_1000_2		2.51
P_H_1000_3		2.46
P_H_1000_4		2.64
P_H_1500_1	1500	2.92
P_H_1500_2		3.18
P_H_1500_3		2.78
P_H_1500_4		3.39

Figure 3-14 presents the variation in the pull-off strength at different aging periods. The pull-off strength was not significantly affected after 500 hours of aging. However, it was increased by 17.7% and 46.9% after 1000 hours and 1500 hours of conditioning. Since all the specimens had a debonding failure in the concrete substrate, the increment in the bond strength could be attributed to the increase in the substrate strength due to the continuation of the hydration process in a wet and warm environment. Table 3-3 summarizes the result of the pull-off strength measured for each specimen.

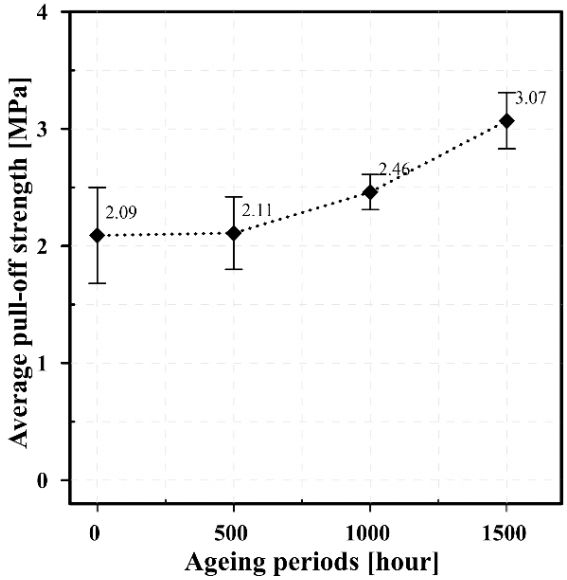

Figure 3-14: Effect of the hygrothermal environment on the pull-off strength

3.4.4 Bond capacity

Single-lap direct-shear test was utilized to evaluate bond durability of CFRP-concrete joints in hygrothermal and wet-dry conditions. Sixteen specimens were tested to evaluate the effect of the hygrothermal condition, whereas the effect of the wet-dry condition was evaluated by testing ten specimens. DIC technique was utilized to determine the strain distribution on the CFRP strip and, subsequently, the fracture energy. The specimens were named following the notation DS_X_m_n, where DS indicated the type of the test (direct shear), X referred to the type of the conditioning environment (H= hygrothermal, WD= wet-dry), m indicated the period of the conditioning (0: no conditioning, 500 hours, 1000 hours, and 1500 hours, 50= number of the wet-dry cycles of the second condition), and n referred to the number of the specimens within the group.

3.4.4.1 Hygrothermal condition

Figure 3-15 shows the failure modes of the specimens. It can be noticed that most of the reference specimens have developed a debonding failure in the concrete substrate. Nonetheless, an adhesive failure within the interface was also detected in the form of small spots located close to the free end of specimen DS_H_0_2.

Regarding the conditioned specimens, most of the specimens have developed a debonding failure in the concrete substrate like the reference specimens. However, some specimens such as DS_H_500_1 have developed a mixed adhesive failure within the interface and cohesive failure in the concrete substrate. It can be noticed that the area of the adhesive failure in some of the conditioned specimens was slightly increased in comparison with control specimens which could be attributed to the effect of the hygrothermal condition. However, the bond strength was not significantly affected, as it is going to be discussed in the following paragraphs, indicating no direct correlation between the area of the adhesive failure and bond strength.

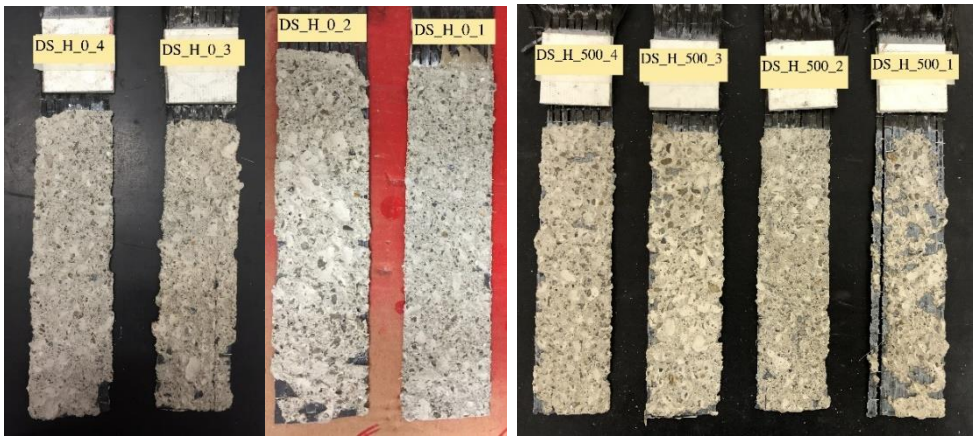

(a) *(b)*

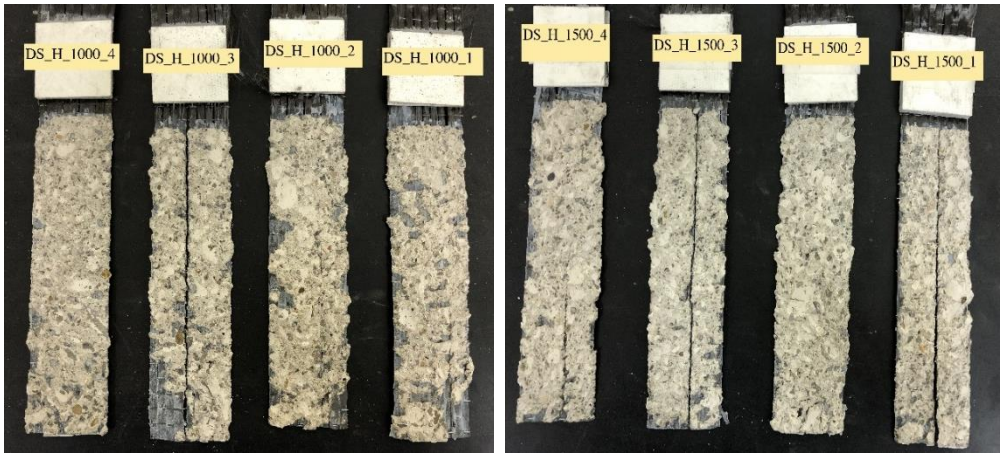

(c) *(d)*

Figure 3-15: CFRP-concrete interface failure mode, (a) control specimens, (b) specimens conditioned for 500h, (c) specimens conditioned for 1000h, (d) specimens conditioned for 1500h

The load-global slip (*P-g*) response of representative specimens is shown in Figure 3-16. The specimens had a linear ascending portion. It can be noticed that the stiffness of the ascending portion has slightly increased after conditioning. However, since this increment falls within the scatter of the data, it is considered insignificant. At the end of this stage, macro cracks were detected on the CFRP-concrete interface, and the slope of the load-slip curve started decreasing, taking a horizontal path, and the *P-g* response became non-linear. Figure 3-16 illustrates two points on the horizontal part of the curve. The first point is P^*, referring to the peak load recorded for a specimen. The load after this point usually

started decreasing and take a nominal constant behavior. The average of the nominal horizontal part is referred to as P_{cpty} which represents the load-carrying capacity of the specimen. P_{cpty} was determined as the mean load within the global slip range (g_1-g_2) based on the instruction of Carloni et al. (Carloni, Santandrea, & Imohamed, 2017). The slip range (g_1-g_2) of the load *P*-*g* response refers to the part where the stress-transfer mechanism was fully established and evaluated based on the strain analysis obtained from the DIC technique which is going to be explained in section 3.4.5. For the specimens tested without the DIC technique (Table 3-4), g_1 was considered as the point directly after the P^* while g_2 is the point at the start of the last ascending part of the *P*-*g* graph. Table 3-4 summarizes the values of the P^*, average peak load ($\overline{P^*}$), P_{cpty}, average load capacity ($\overline{P_{cpty}}$), g_1, and g_2 for each specimen.

The effect of the hygrothermal environment on the average load capacity was presented in 3-17. CoV was in the range of 6.7%-14.9%. The $\overline{P_{cpty}}$ was increased by 16.3% after 500 hours of conditioning. After that, it started decreasing; yet it still higher than the value of the control specimens by 8.8% and 4.8% at 1000 h and 1500 h, respectively. This small increment in the average load capacity can be ascribed to the post-curing effect of the resin (see section 3.4.1) and improvement in the mechanical properties of the concrete, as going to be discussed in section 3.4.4.2. Finally, similar behavior was also reported in the literature (Benzarti, Chataigner, et al., 2011; Teng, Zhang, Dai, & Chen, 2013).

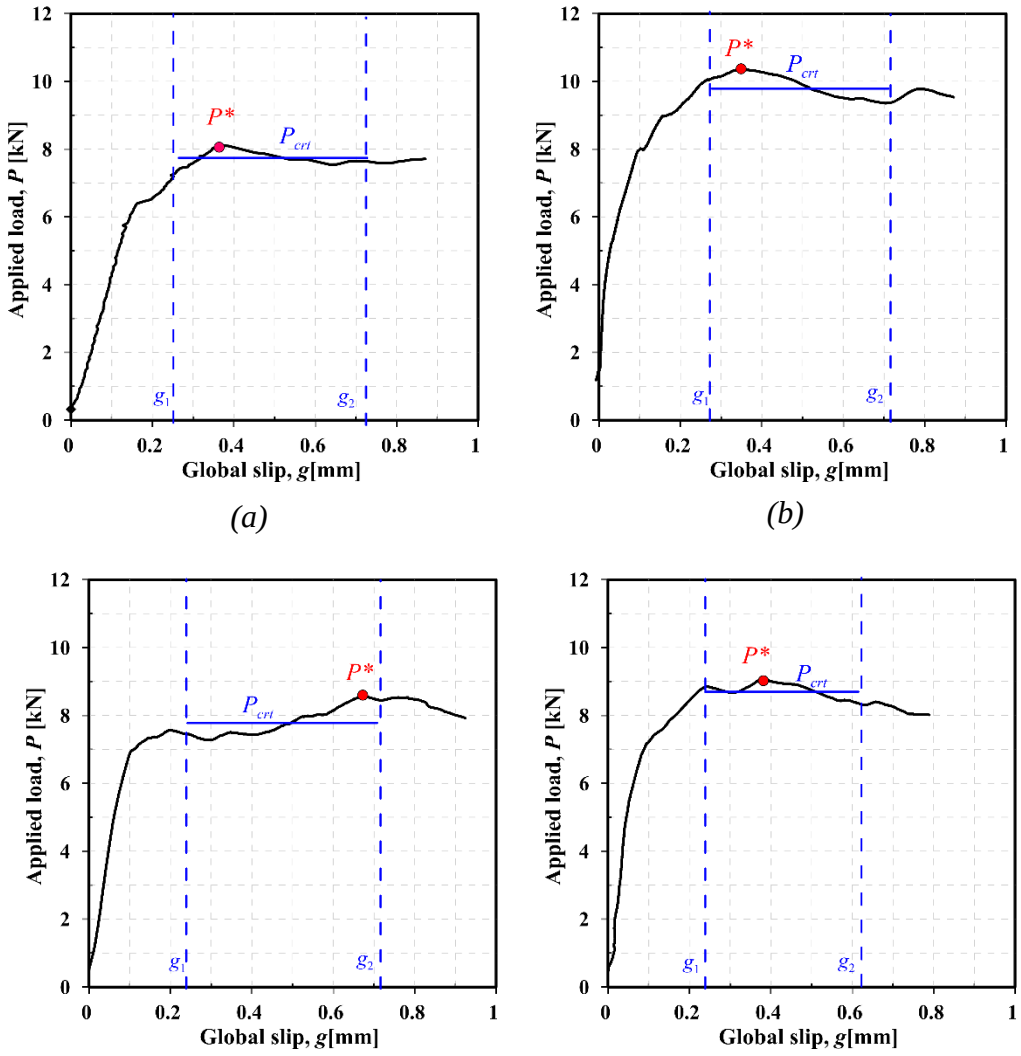

Figure 3-16: load-slip response of the specimens, (a) DS_H_0_1, (2) DS_H_500_1, (3)DS_H_1000_2, (d) DS_H_1500_4

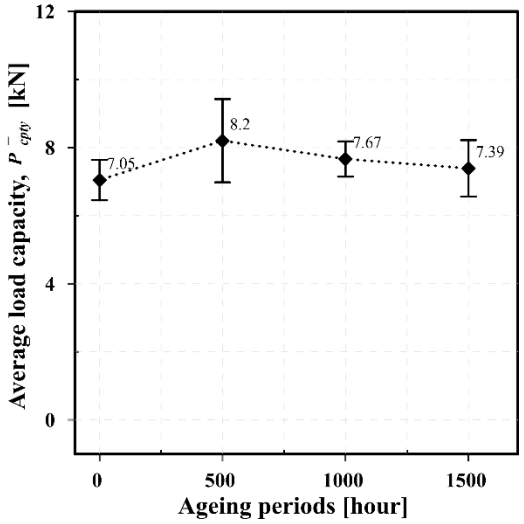

Figure 3-17: Effect of the hygrothermal on the average load capacity

Table 3-4: Effect of the hygrothermal condition on the bond capacity of CFRP-concrete joints

Specimen Name	Ageing period (hours)	P^* (kN)	$\bar{P}^*$ (kN)	P_{cpcy} (kN)	$\bar{P}_{cpcy}$ (kN)	g_1 (mm)	g_2 (mm)	DIC
DS_H_0_1	0	8.12	7.68 (6.92)	7.1	7.05 (8.39)	0.17	0.52	×
DS_H_0_2		6.82		6.13		0.38	0.46	✓
DS_H_0_3		8.12		7.78		0.23	0.73	✓
DS_H_0_4		7.64		7.18		0.53	0.74	✓
DS_H_500_1	500	10.33	8.66 (14.58)	9.87	8.21 (14.9)	0.26	0.71	✓
DS_H_500_2		7.09		6.66		0.23	0.48	✓
DS_H_500_3		9.35		8.78		0.57	0.92	✓
DS_H_500_4		7.86		7.54		0.20	0.58	×
DS_H_1000_1	1000	8.73	8.31 (4.69)	8.25	7.67 (6.74)	0.35	0.73	✓
DS_H_1000_2		8.57		7.87		0.24	0.72	✓
DS_H_1000_3		8.24		7.7		0.22	0.62	✓
DS_H_1000_4		7.71		6.84		0.16	0.53	×
DS_H_1500_1	1500	7.35	7.79 (10.36)	6.87	7.39 (11.2)	0.16	0.35	✓
DS_H_1500_2		6.91		6.62		0.15	0.50	×
DS_H_1500_3		7.84		7.31		0.68	0.99	✓
DS_H_1500_4		9.07		8.76		0.22	0.51	✓

* CoV reported between parentheses

3.4.4.2 Wet-dry condition

All the reference specimens have developed a debonding failure in the concrete substrate, as shown in Figure 3-18a. However, small spots of adhesive debonding within the interface were recognized. In comparison with reference specimens of the hygrothermal condition, the thickness of the debonded concrete substrate was thinner. This difference was attributed to the variation in the mechanical properties of the two concrete batches (i.e., concrete compressive strength).

At the end of the wet-dry cycles, the failure mode was shifted to an adhesive debonding failure in the interface of the CFRP-concrete joint or a mixed debonding failure, as shown in Figure 3-18b. The change in the failure mode is ascribed to the alternating effect of wetting and drying, which is going to be further discussed in the following paragraphs. It is essential to mention that the specimens were tested in a completely dry condition. They were removed out of the chamber at the end of the wet-dry cycles and left in the lab condition (25 ^{o}C) for 2 to 3 weeks until they were tested.

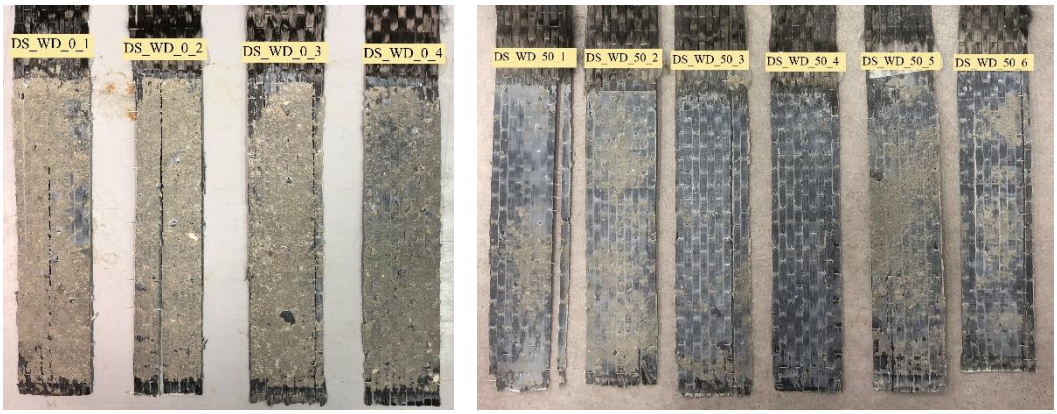

(a) *(b)*

Figure 3-18: CFRP-concrete joints' failure modes under wet-dry cycles, (a) reference specimens, (b) conditioned specimens

The *P-g* response of the reference specimens is illustrated in Figure 3-19a. The specimens had an initial linear behavior which started shifting to non-linear and taking a horizontal path close to the peak value. The *P-g* response of the specimens exposed to wet-dry cycles is presented in Figure 3-19b. Similarly, the specimens had an initial linear behavior; however, some of the conditioned specimens had a lower stiffness, such as DS_WD_50_4 and 5. Moreover, the response started changing to non-linear at a lower load value. Nonetheless, the P^* and P_{cpty} of the conditioned specimens were not significantly affected, as shown in Table 3-5. The $\overline{P_{cpty}}$ was increased by 3%. This increment is considered trivial since it falls within the scatter of the data, which was ranging between 3.5% and 6.3%.

The results of the wet-dry conditions implied that though wet-dry cycles had a pronounced effect on the failure mode of the CFRP-concrete joint, they did not significantly influence the bond capacity of the joint. In other words, there is no direct correlation between failure mode and bond capacity. This controversial finding could be attributed to two possible hypotheses. The first one is that the aqueous environment has resumed the hydration process in the concrete prisms leading to an increase in their compressive strength. Consequently, the failure mode was shifted from the concrete substrate to the CFRP-concrete interface. This hypothesis was supported by the results of compressive tests performed on 100x100x100 mm cubes cut from the prisms utilized for single-lap direct shear tests after being exposed to the wet-dry conditions. The compressive strength was increased from 38 MPa (for reference specimens) to 52 MPa (for conditioned specimens). More studies with a higher number of cycles (around 200 to 300 cycles) are advised to investigate this hypothesis. The second hypothesis is that water during the wetting phase has softened the epoxy via plasticization and reduced the chemical bond and the mechanical interlocking between CFRP strip and concrete substrate (Sen, 2015; Tuakta & Büyüköztürk, 2011). Concurrently, water droplets have replaced the epoxy resin in the voids of the substrate. After exposure to warm air, the plasticization process was reversed and the chemical bond between CFRP strip and concrete substrate was restored. However, the mechanical interlocking was not restored which might be attributed to the presence of water droplets in the voids since the drying process starts from outside to inside (i.e., from the CFRP strip to the concrete substrate). Therefore, the epoxy resin could not fill again to voids of the substrate.

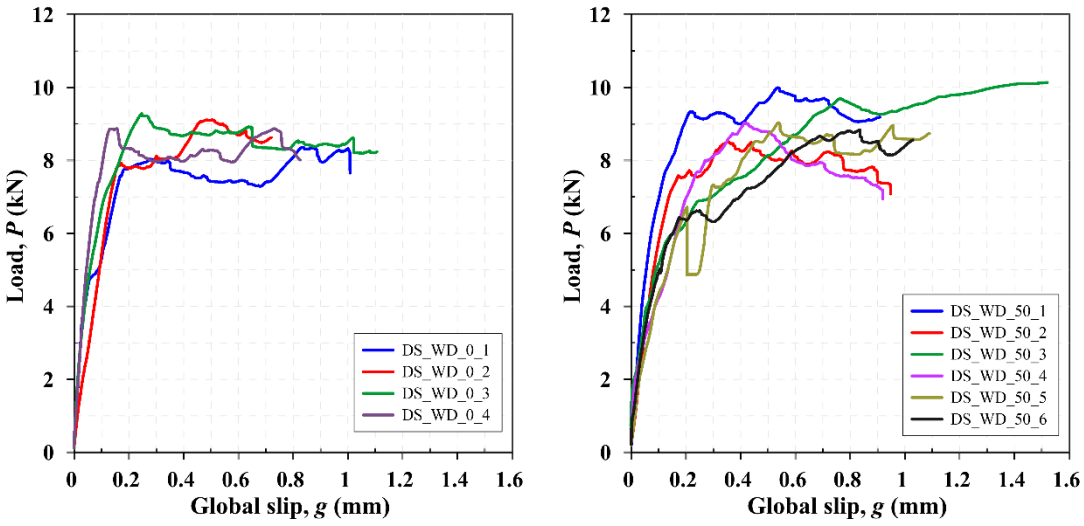

(a) *(b)*

Figure 3-19 P-g response for (a) reference specimens, (b) specimens exposed to the wet-dry conditions

Table 3-5: Effect of wet-dry condition on the bond capacity of CFRP-concrete joints

Specimen Name	Number of cycles	P^* (kN)	$\overline{P^*}$ (kN)	P_{cpcy} (kN)	$\overline{P_{cpcy}}$ (kN)	g_1 (mm)	g_2 (mm)	DIC
DS_WD_0_1	0	8.36	8.91 (3.91)	7.81	8.27 (3.52)	0.33	0.92	✓
DS_WD_0_2		9.11		8.46		0.28	0.61	×
DS_WD_0_3		9.28		8.57		0.46	1.00	×
DS_WD_0_4		8.87		8.24		0.27	0.69	✓
DS_WD_50_1	50	9.99	9.26 (6.44)	9.46	8.51 (6.28)	0.23	0.84	×
DS_WD_50_2		8.53		8.09		0.23	0.75	×
DS_WD_50_3		10.14		8.93		0.34	1.32	✓
DS_WD_50_4		9.03		8.35		0.31	0.79	✓
DS_WD_50_5		9.03		8.39		0.39	0.91	×
DS_WD_50_6		8.83		7.86		0.30	0.90	✓

3.4.5 Bond characteristics and fracture energy

DIC technique was utilized to determine strain profile on CFRP-concrete joints; after that, bond characteristics and fracture energy of the interface were determined based on the strain profile.

Figure 3-20a illustrates the typical *P-g* response of the CFRP-concrete joints along with three points (i.e., A, B and C) specified on the horizontal part of the curve. Figure 4-21b presents the typical experimental strain profile (ε_{yy}) averaged along a 10 mm strip width within the center of the CFRP strip. The cartesian system used to graph the strain profile is shown in Figure 3-6 with the origin point located at the free point of the CFRP reinforcement, where the x-axis of Figure 3-20b represents the bonded of the CFRP strip.

The averaged experimental strain profile (ε_{yy}) was fitted using the function (Jianguo Dai, Ueda, & Sato, 2005)

$$\varepsilon_{yy}(y) = \frac{A}{1 + e^{-B(Ay+C)}} \tag{3-1}$$

Where A, B, and C are parameters determined using a best-fitting procedure of the experimental strain profile. It is worth mentioning that there are some other functions proposed by other researchers (Ali-ahmad et al., 2006; Carloni et al., 2017) to fit the experimental strain profile; nonetheless, they did not have a significant effect on the values of the CML and fracture energy.

Generally, the ε_{yy} curve (Figure 3-20b) can be divided into three main zones (Carloni et al., 2017). The first one is the Stress-Free Zone (SFZ) which is located at the free end of the specimen. The value of the ε_{yy} in this region is around zero. The second one is the Stress-Transfer Zone (STZ). In this zone, the stress is transferred from the CFRP to concrete. The last one is the Fully Debonded Zone (FDZ) and located at the loaded end of the specimen. This region is debonded from the concrete substrate, and there is no stress transfer. Consequently, STZ is the only region transferring stress between CFRP and concrete. Figure 3-20c presents the behavior of the STZ measured at different points within the *P-g* response (Figure 3-20a). As the value of the *g* increases, STZ moves from the loaded end toward the free end. The global slip range (g_1-g_2) was selected by

specifying the first point (g_1) and the last point (g_2), where the STZ was fully developed. In other words, point g_1 represents the beginning of the debonding (the point where the STZ was fully established) while g_2 refers to the point where STZ reaches the free end.

Assuming a pure fracture mechanic with mode-II loading condition, the interfacial shear stress, τ, and slip, s, can be determined by equilibrium and compatibility of the CFRP strip (Ali-ahmad et al., 2006; Carloni et al., 2017):

$$\tau(y) = E_f t_f \frac{d\varepsilon_{yy}}{dy} \tag{3-2}$$

$$s(y) = \int_0^y \varepsilon_{yy}\, dy \tag{3-3}$$

where E_f is the average elastic modulus of the CFRP coupon for each exposure period as discussed in section 3.4.2; t_f is the nominal thickness of the carbon fiber textile (i.e., 0.166 mm).

CML for the CFRP-concrete interface can be obtained by solving Equations (3-2) and (3-3) for the fitted strain values and combining them after that. Figure 3-20d presents the CML determined at point A of the *P-g* response (Figure 3-20a). Finally, the interfacial fracture energy of the interface, G_F, is calculated as the area under the CML curves:

$$G_F = \int_0^\infty \tau\,(s) ds \tag{3-4}$$

The fracture energy, G_F, and load capacity, $P_{cpty.}$, for each specimen were determined as the average value for 5 points of the *P-g* response within the range (g_1-g_2).

After determining the G_F of the interface, the effective bond length of the interface, l_{eff}, (i.e., the length of the STZ) can be determined using the equation (Carloni et al., 2017):

$$l_{eff} = \frac{\sqrt{2E_f t_f}}{B\sqrt{G_F}} \ln\left(\frac{1+\alpha}{1-\alpha}\right) \tag{3-5}$$

Where B is a parameter determined based on best fitting procedure; α is assumed equal to 0.96 based on (Carloni et al., 2017).

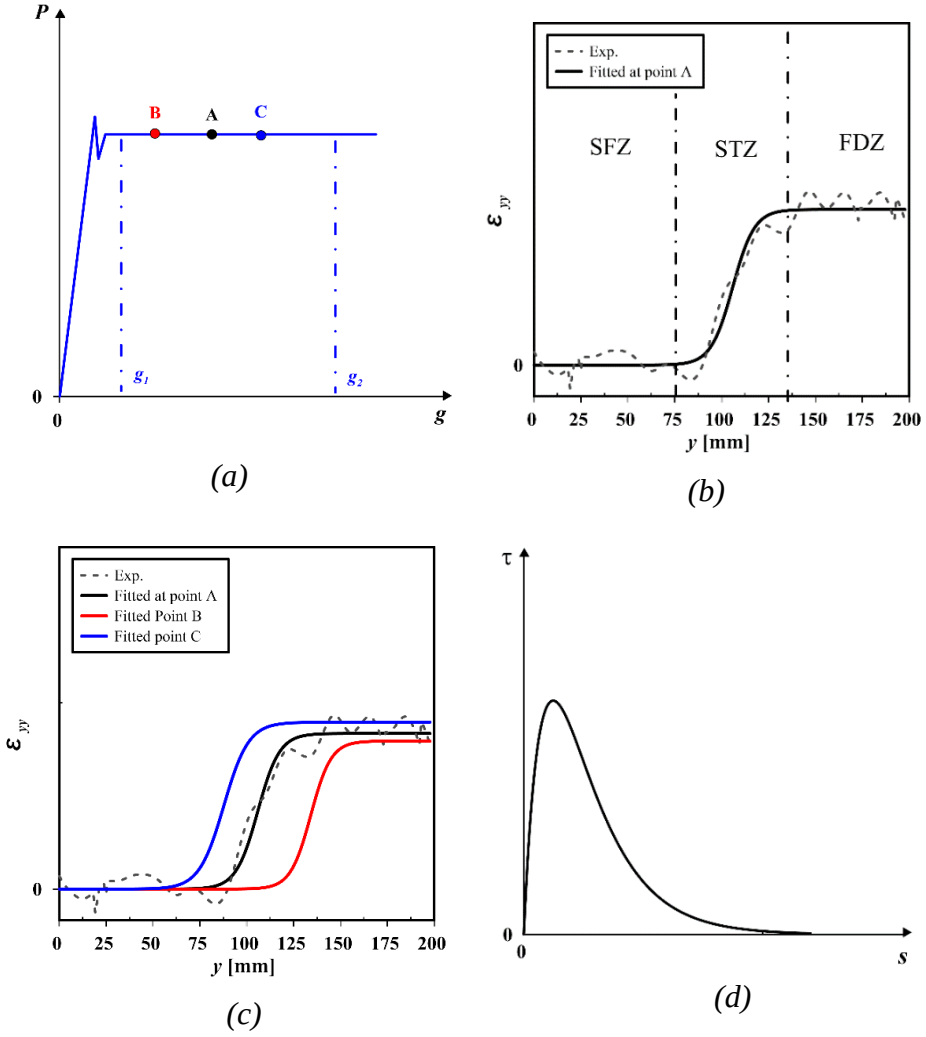

Figure 3-20: typical procedure utilized to determine bond characteristics based on DIC technique, (a) typical P-g response (b) *typical experimental and fitted* ε_{yy} *(c) typical fitted* ε_{yy} *at different global slip values, (d) cohesive material law*

3.4.5.1 Hygrothermal condition

Figure 3-21 illustrates strain distribution on the CFRP-concrete joint and adjacent concrete surface of the specimen DS_H_1500_4 at two specific points within the *P-g* response where the stress-transfer mechanism has fully developed. The strain profile has an S shape (Ali-ahmad et al., 2006; Franzoni et al., 2017) with the highest value at the loaded end and lowest value (almost zero) at the free end, as explained in the previous section. As the value of the global slip (*g*) increased from 0.22 mm (Figure 3-21a) to 0.30 mm (Figure 3-21b), strain values started increasing and moving toward the free end.

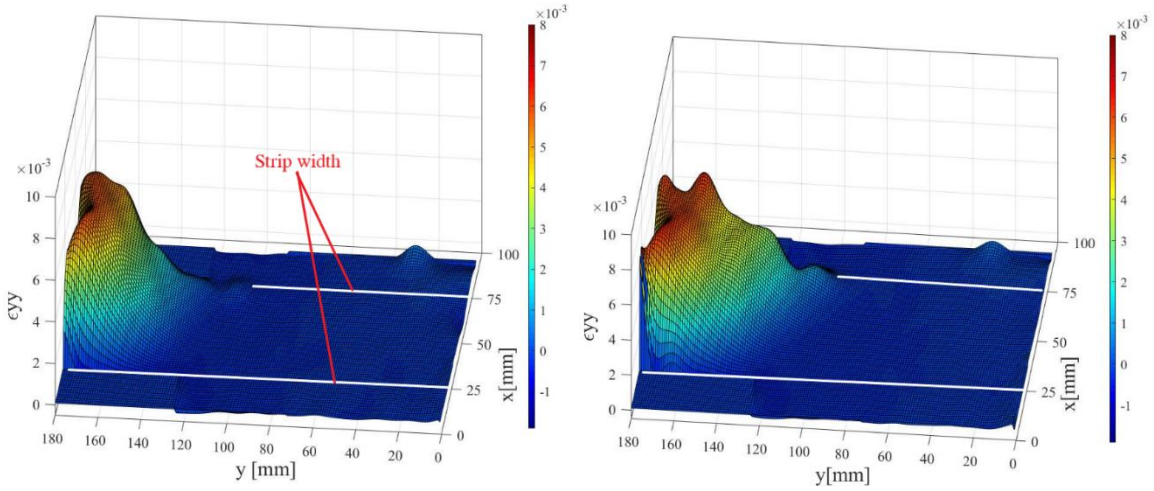

Figure 3-21: strain profile on CFRP-concrete interface for the specimen DS_H_1500_4 at slip of (a) g= 0.22 mm, (b) g=30 mm

The effect of the hygrothermal condition on the CML is illustrated in Figure 3-22a. It can be noticed that the interfacial elastic shear stiffness, k_s (i.e., stiffness of the ascending portion of the curves), has slightly increased after conditioning. This finding agrees with the *P-g* response discussed in section 3.4.4.1 and presented in Figure 3-16, which was attributed to the increase in the compressive strength of the concrete due to the conditioning.

Figure 3-22b illustrates the effect of the hygrothermal condition on the average effective bond length, $\overline{l_{eff,}}$ (i.e., length of the STZ) of each exposure period. It can be noticed that the $\overline{l_{eff}}$ was not significantly affected after 500 hours of conditioning; however, it was decreased by 27% after 1500 hours. Since the failure mode was not changed, the decrease in the effective bond length could be attributed to the increase in the interfacial stiffness of the joints due to the continuation of the hydration process for the concrete substrate.

Figure 3-22c and d present the effect of hygrothermal condition on the average debonding strain, $\overline{\varepsilon_{max}}$, and $\overline{G_F}$, respectively. They both follow the same trend observed for the $\overline{P_{cpty}}$ (Figure 3-17). $\overline{\varepsilon_{max}}$ increased by 14% after 500 hours of conditioning, while $\overline{G_F}$ was increased by 28.6%. After that, they started decreasing; yet after 1500 hours of conditioning, $\overline{\varepsilon_{max}}$ was higher than the control specimens by 4% while $\overline{G_F}$ was higher by 9%. Despite the scatter noticed in the results, this minor variation in the ε_{max} and G_F could be ascribed to the effect of the hygrothermal condition on the CFRP-concrete joint. Generally, it can be noticed that the scatter of the data was increased for $G_{F,}$ especially at 500 hours which is scribed to the unavoidable margin of error accompanies the procedure utilized to determined G_F using the DIC technique.

The load-carrying of the joint can be estimated based on ε_{max} or G_F using Equations (3-6) and (3-7)(3-5), respectively, (Jianguo Dai et al., 2005; Täljsten, Journal, Publishers, Engineering, & Engineering, 1996; Wu et al., 2002)

$$P_{est}^{\varepsilon_{max}} = E_f b_f t_f \varepsilon_{max} \tag{3-6}$$

$$P_{est}^{G_F} = b_f \sqrt{2 E_f t_f G_F} \tag{3-7}$$

Where b_f is the width of the bonded CFRP strip.

Table 3-6 summarizes the values of the load-carrying capacity estimated with Equations (3-6) and (3-7). The difference between the values estimated with the two equations is relatively small (around 1%). Nonetheless, these estimated values were higher than the corresponding experimental results, P_{cpty}, by 6%-23%, as shown in Table 3-6. Carloni et al. (Carloni et al., 2017) reported that evaluating the elastic modulus of the CFRP strip based on the thickness of the bare fiber (i.e., t_f) can overestimate load-carrying capacity.

Regardless of the effect of the elastic modulus, the main reason for the difference between the estimated load values and corresponding experimental results is that Equations (3-6) and (3-7) do not consider strain variation along the width of the interface (i.e., they consider ε_{yy} constant along the width). Nevertheless, studies (Benvenuti, Orlando, Ferretti, & Tralli, 2016; Carloni et al., 2017) emphasize that ε_{yy} is constant only within the central part of the CFRP-concrete interface and it depends on the ratio of the width between CFRP and concrete substrate. Figure 3-23 illustrates the variation of ε_{yy} across the width of the interface and at different locations along the bonded length at the point of specimen DS_H_1500_4. It can be noticed that the value of the ε_{yy} at the edge of the interface is lower than in the center.

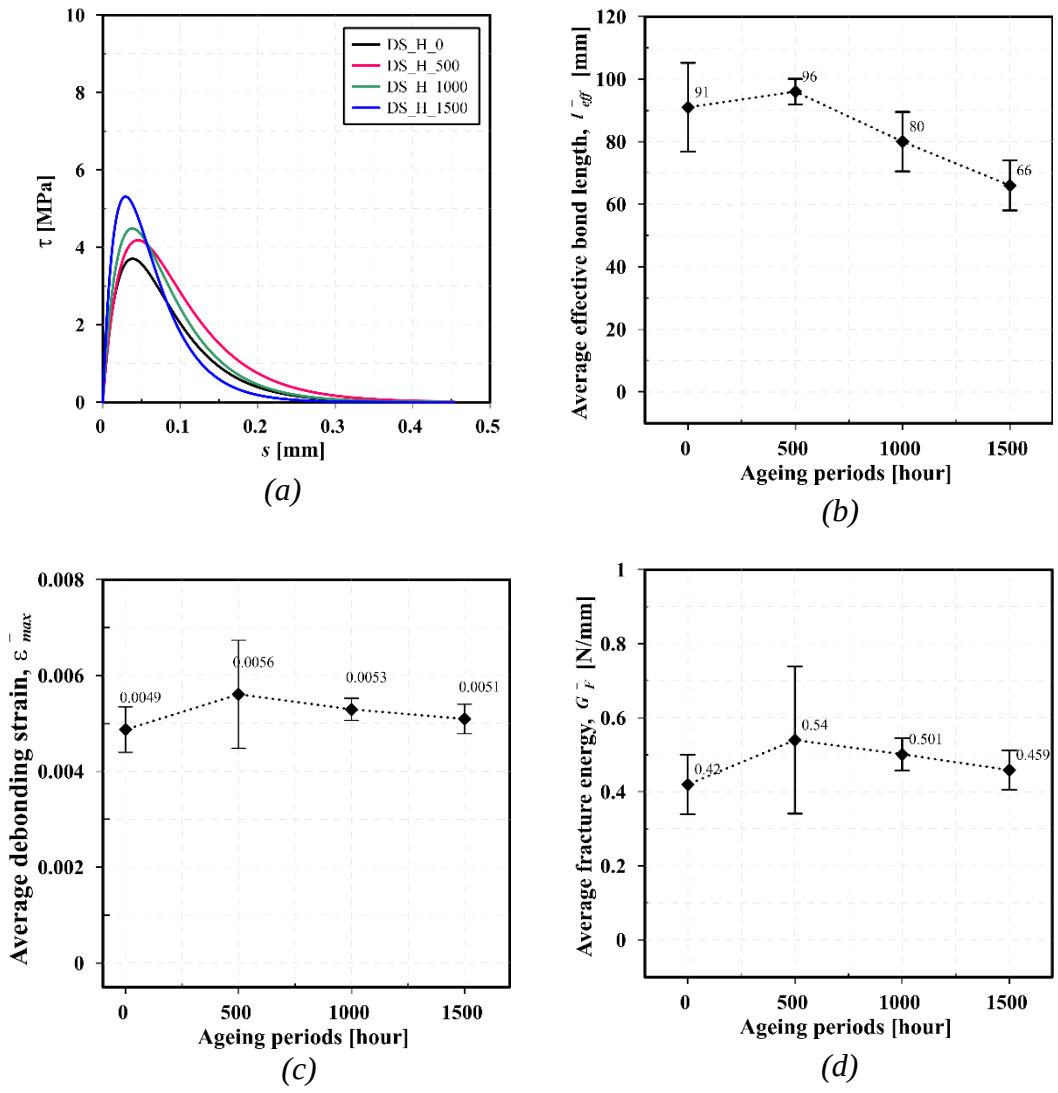

Figure 3-22:effect of hygrothermal condition on bond characteristics, (a) CML, *(b)* l_{eff}, *(c)* ε_{max}, *(d)* G_F

Table 3-6: Effect of hygrothermal condition on bond characteristics

Specimen Name	Condition (hours/ cycle)	P_{cpty} (kN)	l_{eff} (mm)	ε_{max}	$P_{est}^{\varepsilon_{max}}$ (kN)	G_F (N/mm)	$P_{est}^{G_F}$ (kN)	$1-\frac{P_{cpty}}{P_{est}^{G_F}}$ (%)
DS_H_0_2	NA	6.13	87	0.0044	7.65	0.35	7.72	21
DS_H_0_3		7.78	76	0.0048	8.32	0.41	8.41	7
DS_H_0_4		7.18	110	0.0054	9.28	0.51	9.34	23
DS_H_500_1	500	9.87	97	0.0064	10.63	0.69	10.64	7
DS_H_500_2		6.66	90	0.0043	7.13	0.31	7.19	7
DS_H_500_3		8.78	100	0.0061	10.03	0.62	10.07	13
DS_H_1000_1	1000	8.25	68	0.0055	9.61	0.53	9.62	14
DS_H_1000_2		7.87	83	0.0050	8.83	0.45	8.86	11
DS_H_1000_3		7.70	90	0.0054	9.50	0.52	9.54	19
DS_H_1500_1	1500	6.87	69	0.0051	8.83	0.46	8.91	23
DS_H_1500_3		7.31	54	0.0048	8.22	0.40	8.33	12
DS_H_1500_4		8.76	73	0.0054	9.28	0.51	9.36	6

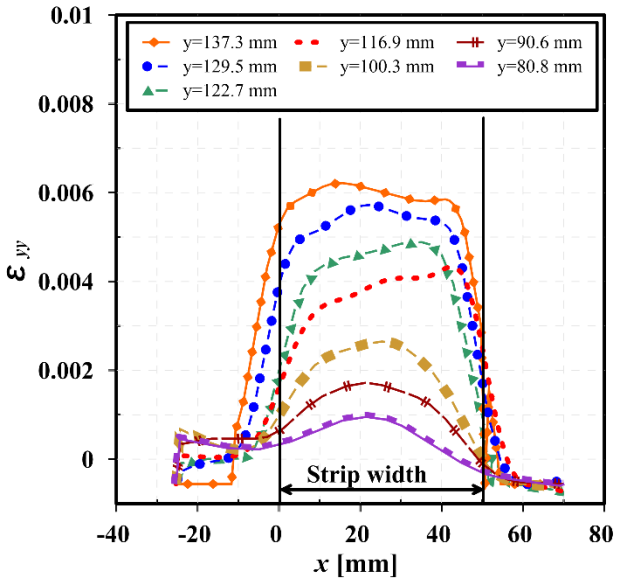

Figure 3-23: variation of ε_{yy} across the width of the CFRP-concrete interface and at different locations along the bonded length.

3.4.5.2 Wet-dry conditions

Figure 3-24 compares the experimental and fitted strain profile averaged along 10 mm width within the center of the CFRP strip of specimen DS_WD_0_4 and specimen DS_WD_50_4. Strain profiles have S shapes with the highest strain values at the loaded end and lowest values at the free end of the joint. It can be noticed that the shape of the fitted strain profile was changed after conditioning where the stiffness of the STZ was decreased; however, its length was increased. Furthermore, the value of the debonding strain at the FDZ was slightly increased. These changes had a noticeable influence on the shape of the CML and subsequently bond characteristics.

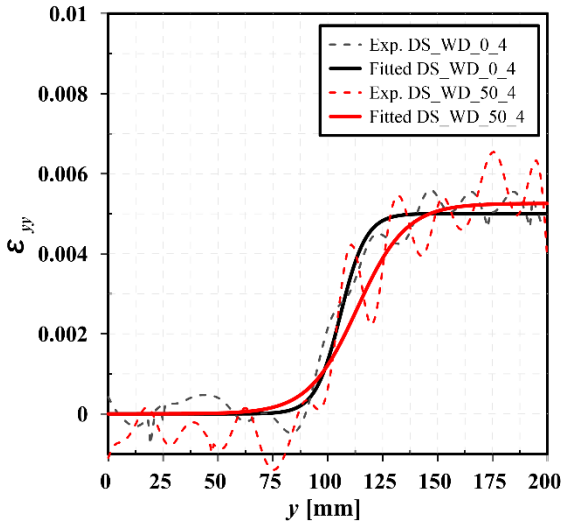

Figure 3-24: comparison of the strain profile for specimens DS_WD_0_4 and DS_WD_50_4.

Figure 3-25 compares the average CML of the reference specimens with conditioned specimens. As previously predicted, the shape of the CML was changed after conditioning, where the interfacial elastic shear stiffness, k_s, was decreased. Furthermore, the interface started softening at a lower shear stress value. These two findings reasonably agree with the *P-g* response of the joint discussed in section 3.4.4.2 and ascribed to the change in the failure mode.

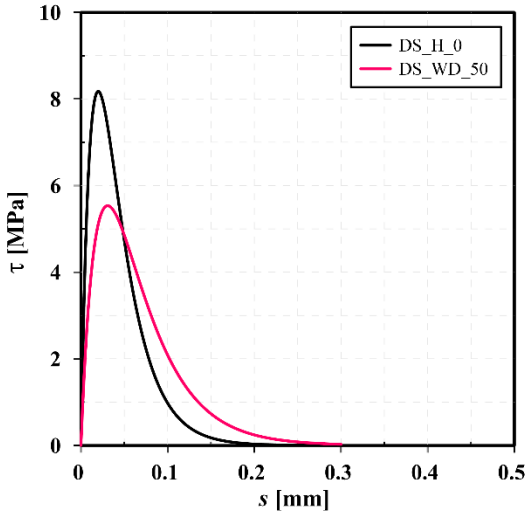

Figure 3-25: effect of wet-dry cycles on the bond characteristics

Table 3-7 reports the l_{eff} of the reference and conditioned specimens as evaluated based on Equation (3-5). As implied from the length increment of the STZ (Figure 3-24), the $\overline{l_{eff}}$ was increased by 51% after exposing to the wet-dry cycles.

Table 3-7 also presents the effect of the wet-dry condition on the G_F. After exposure to wet-dry conditions, $\overline{G_F}$ was only increased by 4%. Nonetheless, since this increment falls within the scatter of the data, which was in the range of 4-11%, it is considered insignificant. Although the stiffness of the CML was decreased after conditioning, it can be noticed from Figure 3-25 that the area under the CML curve was not significantly changed due to an increase in the effective bond length. The value of ε_{max} of each specimen was reported in Table 3-7. $\overline{\varepsilon_{max}}$ was increased by 3.8 % after conditioning; however, the CoV was around 5%, implying trivial change.

The load-carrying capacity of the joints before and after conditioning was estimated using Equations (3-6)and (3-7) and reported in Table 3-7. As noticed in section 3.4.5.1, the estimated values were higher than the experimental results by 4% to 14% since Equations (3-6) and (3-7) do not consider strain variation along the width (Figure 3-23).

Table 3-7: Effect of wet-dry condition on bond characteristics

Specimen Name	Condition (hours/ cycle)	P_{cpty} (kN)	l_{eff} (mm)	ε_{max}	$P_{est}^{\varepsilon_{max}}$ (kN)	G_F (N/mm)	$P_{est}^{G_F}$ (kN)	$1-\frac{P_{cpty}}{P_{est}^{G_F}}$ (%)
DS_WD_0_1	NA	7.81	41	0.0052	8.92	0.52	9.03	14
DS_WD_0_4		8.24	45	0.0049	8.42	0.42	8.54	4
DS_WD_50_3	50	8.93	64	0.0055	9.48	0.50	9.59	7
DS_WD_50_4		8.35	65	0.0055	9.48	0.52	9.59	13
DS_WD_50_6		7.86	66	0.0050	8.54	0.46	8.67	9

3.5 Numerical modeling using finite elements

The numerical study presented in this part of the research includes a simulation of the single-lap direct-shear test of the CFRP-concrete joint presented in section 3.3.2. The main objective is to calibrate a numerical model so it could be implemented in a future parametric study aiming the evaluate the effect of different concrete strength and FRP materials.

The CMLs evaluated experimentally are utilized here to define the inputs of traction-separation laws between the master and slave surfaces which is used to replicate the behavior of the whole joint. Three parameters are utilized to define traction-separation laws: (i) interfacial elastic shear stiffness, k_s; (ii) maximum shear stress, τ_{max}; (iii) fracture energy, G_F.

The behavior of the joint is simulated using commercial software Abaqus. Subsequently, the accuracy of the model is validated by comparing the solution of the numerical model with experimental results in terms of failure load, *P-g* response, strain distribution, and debonding strain. The results indicated that the model could reasonably simulate the behavior of the CFRP-concrete joint under hygrothermal and wet-dry conditions.

3.5.1 Geometry and material properties

Since a 2D model can reasonably simulate the CFRP-concrete joint (Chen, Teng, & Chen, 2010; Tao & Chen, 2014), it was adopted in this research to reduce the computational effort. The geometry of the model mimicked the single-lap shear test of the joint. The model is assembled in two parts. The first part simulated the concrete prism with a length and height of 250 mm and 50 mm, respectively. The second part replicated the CFRP strip with a length and thickness of 200 mm and 0.166 mm. Figure 3-26 illustrates the parts of the model.

An elastic isotropic material was utilized to simulate the behavior of the concrete. The elastic modulus was determined from the compressive strength of each batch, as reported in section 3.3.1 using the formula (CEB-FIP, 2010):

$$E_c = \alpha_i \,.\, E_{c0} \,.\, \alpha_E \,.\, \left[\frac{f_{cm}}{10}\right]^{1/3} \tag{3-8}$$

Where E_{c0} = 21.5*10^3 MPa; α_E is 1.0 for quartzite aggregates; f_{cm} is concrete compressive strength at the age of 28 days; α_i is a reduction factor depends on the concrete compressive strength and can be determined using the equation:

$$\alpha_i = 0.8 + 0.2\,\frac{f_{cm}}{88} \leq 1.0 \tag{3-9}$$

Although CFRP strip is characterized with an orthotropic behavior (involving unidirectional fibers), in the current model, it only behaves in the longitudinal direction; therefore, it was modeled as a linear elastic isotropic material with ν=0.3 for the purpose of simplicity (Arruda, Firmo, Correia, & Tiago, 2016). The average values of the elastic modulus presented in Figure 3-12b are used here for the CFRP strip

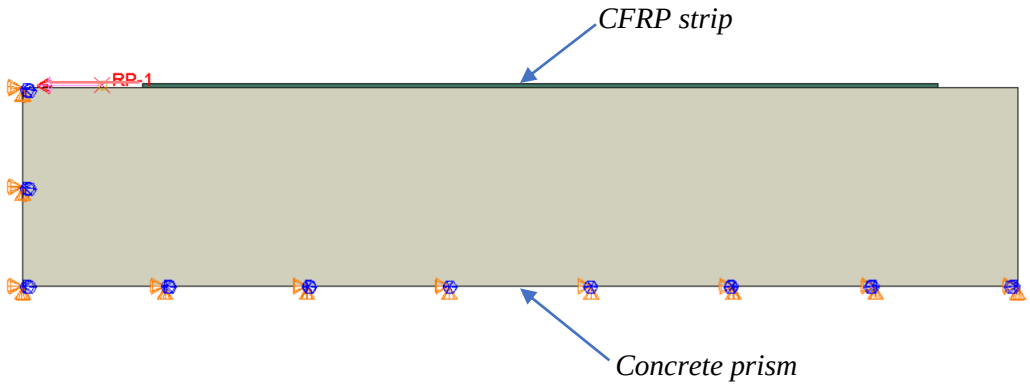

Figure 3-26: Model parts and boundary conditions

3.5.2 Boundary condition, loading, and type of analysis

A fixed boundary condition was imposed on the bottom and side faces of the concrete prism, as shown in Figure 3-26. This boundary condition was intended to prevent the prism from movement and replicates the test setup. The pulling load at the end of the CFRP strip was simulated with the displacement boundary condition that was applied at the loaded end of the CFRP strip, as illustrated in Figure 3-26. Since the loading speed utilized during the experimental campaign was relatively slow, a general static non-linear analysis was utilized to simulate debonding of the CFRP strip from the concrete prism.

3.5.3 Contact interface, element type and mesh characteristics

In the current model, the interaction between CFRP strip and concrete substrate was modeled using a surface-based cohesive behavior which is defined based on the traction-separation law. Surface-based cohesive behavior is intended to model interfaces with a negligible thickness ("Abaqus Documentation," 2018), as in the case of the CFRP-concrete joint. Furthermore, it can simulate the delamination between the CFRP strip and concrete substrate.

The traction-separation model in Abaqus adopts an initial linear elastic behavior followed by the initiation and evolution of damage, as shown in Figure 3-27. The linear elastic behavior is written using an elastic constitutive matrix that correlates the normal stress and shear stress to the normal separation and shear separation, respectively, across the

interface through elastic constitutive matrix K ("Abaqus Documentation," 2018). The cohesive behavior for a two-dimensional model is expressed using the equation:

$$t = \begin{Bmatrix} t_n \\ t_s \end{Bmatrix} = \begin{bmatrix} K_{nn} & K_{ns} \\ K_{sn} & K_{ss} \end{bmatrix} \begin{Bmatrix} \delta_n \\ \delta_s \end{Bmatrix} = K\delta \qquad (3\text{-}10)$$

Where t is the traction vector with its normal component (t_n) and shear component (t_s); δ is the separation vector and its corresponding normal component (δ_n) and shear component (δ_s). In the current model, the linear elastic behavior of the traction-separation law for the case of the shear component (K_{ss}) was defined using the linear elastic branch of the CMLs (i.e., interfacial elastic shear stiffness, k_s), which was determined from the experimental campaign (Figure 3-22a and Figure 3-25). However, the value of the K_{nn} was assumed to be much higher than K_{ss} (in this research, it is assumed to be two times K_{ss}) to ensure a dominant shear behavior (i.e., mode-II loading condition). Finally, K_{ns} and K_{sn} usually are zero.

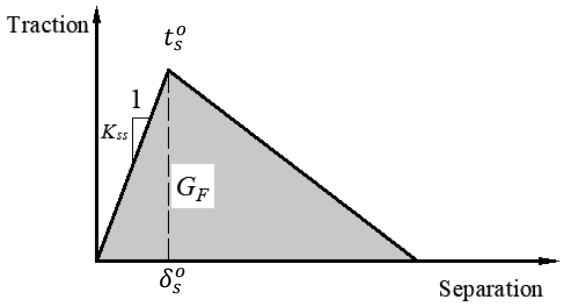

Figure 3-27: traction-separation model adopted by Abaqus

To simulate bond degradation and eventually debonding failure in the CFRP-concrete interface, a damage mechanism was defined, which consists of two components: a damage initiation criterion and a damage evolution law. Damage initiation refers to the onset of the degradation process of the cohesive response at the contact point. Damage initiation can be defined using several criteria such as stress, separation, and others. In the current work, it was defined based on the maximum stress criterion assuming that damage is initiated when the maximum contact stress ratio become one based on the formula:

$$\max\left\{\frac{\langle t_n \rangle}{t_n^o}, \frac{t_s}{t_s^o}\right\} = 1 \tag{3-11}$$

Where t_n^o is the peak value of the traction in a direction normal to the interface; t_s^o is the peak value of the traction in a purely shear direction (Figure 3-27). The value of t_s^o is defined using the maximum shear stress τ_{max}, obtained from the CMLs measured experimentally (Figure 3-22a and Figure 3-25). Similarly, to ensure a dominant shear behavior, the value of the t_n^o is assumed to be much higher than t_s^o (it is assumed $2t_s^o$ in this research).

The damage evolution law explains the rate at which cohesive stiffness is degraded when the damage initiation criterion is reached. In Abaqus, the overall damage at the contact point is represented with a scalar variable *D* which initially has a 0 value. The value of *D* progressively increases to 1 as the load further exceeds the damage initiation criterion. The contact stress components are influenced by the damage according to the formulas:

$$t_n = \begin{cases} (1-D)\bar{t}_n & \bar{t}_n \geq 0 \\ \bar{t}_n & otherwise\ (no\ damage) \end{cases} \tag{3-12}$$

$$t_s = (1-D)\bar{t}_s \tag{3-13}$$

Where $\bar{t}_n$ and $\bar{t}_s$ are the normal and shear traction components, respectively, predicted by the elastic traction-separation behavior for the current separation without damage. In the current model, the damage evolution is defined using the fracture energy, G_F (energy dissipated until failure), determined from the experimental campaign. Table 3-8 reports the values of k_s, τ_{max}, and G_F determined from the experimental campaign and utilized to define the traction-separation laws in Abaqus.

Table 3-8: Input and output of the numerical analysis

Specimen	k_s (MPa/mm)	$\overline{k_s}$ (MPa/mm)	τ_{max} (MPa)	$\overline{\tau_{max}}$ (MPa/mm)	G_F (N/mm)	$\overline{G_F}$ (MPa/mm)	P_{est}^{num} (kN)	P_{cpty} (kN)	$1-\frac{P_{cpty}}{P_{est}^{num}}$ (%)	ε^{num}
DS_H_0_2	97	93	3.4	3.7	0.35	0.42	7.70	6.13	23	0.0043
DS_H_0_3	121		4.3		0.41		8.41	7.78	7	0.0046
DS_H_0_4	60		3.3		0.51		9.34	7.18	23	0.0052
DS_H_500_1	72	76	4.3	3.8	0.69	0.54	10.90	9.87	9	0.0064
DS_H_500_2	85		3.2		0.31		7.37	6.66	10	0.0041
DS_H_500_3	71		4.0		0.62		10.32	8.78	15	0.0060
DS_H_1000_1	150	105	5.5	4.4	0.53	0.50	9.59	8.25	14	0.0054
DS_H_1000_2	87		3.8		0.45		8.83	7.87	11	0.0048
DS_H_1000_3	77		4.0		0.52		9.53	7.70	19	0.0054
DS_H_1500_1	145	151	4.9	5.0	0.46	0.46	8.94	6.87	23	0.0052
DS_H_1500_3	203		5.6		0.40		8.36	7.31	13	0.0046
DS_H_1500_4	104		4.6		0.51		9.40	8.76	7	0.0052
DS_WD_0_1	444	441	8.9	8.4	0.52	0.47	9.42	7.87	16	0.0053
DS_WD_0_4	438		7.9		0.42		8.51	8.24	3	0.0049
DS_WD_50_3	183	181	5.7	5.6	0.50	0.49	9.27	8.93	4	0.0053
DS_WD50_4	183		5.7		0.52		9.42	8.35	11	0.0053
DS_WD_50_6	176		5.3		0.46		8.91	7.86	12	0.0051

k_s= interfacial elastic shear stiffness of the CFRP-concrete interface; $\overline{k_s}$ = averge interfacial elastic shear stiffness; τ_{max}= maximum interfacial shear stress; τ_{max}= averge maximum interfacial shear stress; G_F= interfacial fracture energy; $\overline{G_F}$= average interfacial fracture energy; P_{est}^{num}= load-carrying capacity estimated based on the numerical model; P_{cpty}= load-carrying capacity of the CFRP-concrete joint; ε^{num}= strain estimated numerically on the CFRP strip

Finally, a quadrilateral element (CPS4) was utilized to mesh both CFRP strip and concrete. Mesh size of 1mm element length was used, as shown in Figure 3-28. The size of the mesh was chosen after performing a sensitivity check on the effect of the mesh size on the obtained result.

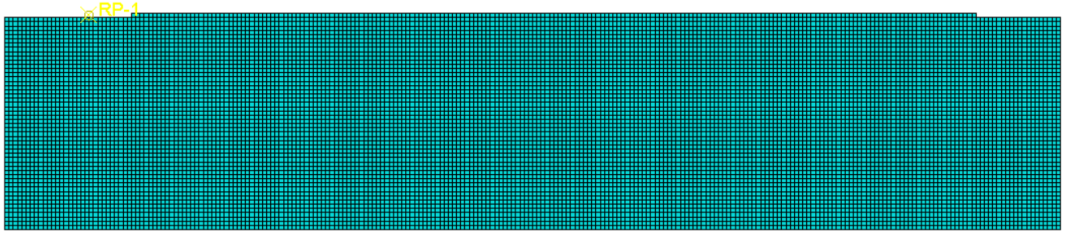

Figure 3-28: Mesh of the finite element model

3.5.4 Numerical result and discussion

In this section, the results obtained from the numerical analyses are presented and validated with the experimental results in terms of load-carrying capacity, *P-g* response, strain distribution, and debonding strain. After that, the *P-g* response of the CFRP-concrete joints under the effect of the hygrothermal and wet-dry conditions is simulated based on the determined average values of CMLs.

Table 3-8 reports the values of the load-carrying capacity estimated by the numerical model, P_{est}^{num}. The relative difference between the estimated values and the experimental values, P_{cpty}, is in the range of 3% to 23%. This range considerably equals to the difference noticed between the P_{cpty} and $P_{est}^{G_F}$, estimated based on Eq.(3-7) and reported in Table 3-6 and Table 3-7. Consequently, the divergence of the numerical result is attributed to the same reason mentioned in 3.4.5.1, where the model does not consider strain variation along the width (i.e., width effect) since it is a 2D model.

Figure 3-29a compares the *P-g* response simulated with the numerical model to the experimental result obtained for specimen DS_WD_0_4. It can be noticed that the numerical model is in good agreement with the experimental behavior.

Figure 3-29b compares strain distribution (ε_{yy}) on the CFRP strip at different g values estimated from the numerical model with the fitted experimental values measured with the DIC technique for specimen DS_WD_0_4. The numerical values are shown as continuous lines; nonetheless, the experimental values are presented as dotted lines. The comparison of the results indicates a reasonable agreement between the numerical and experimental values. Furthermore, it can be noticed that the three zones of the strain distribution (i.e., fully debonded zone, stress-transfer zone, and stress-free zone) are fully developed at a g= 0.14mm. Subsequently, the stress-transfer zone self-translates toward the free end of the joint with the propagation of the debonding process as the g increases until full debonding occurred at g= 0.82mm.

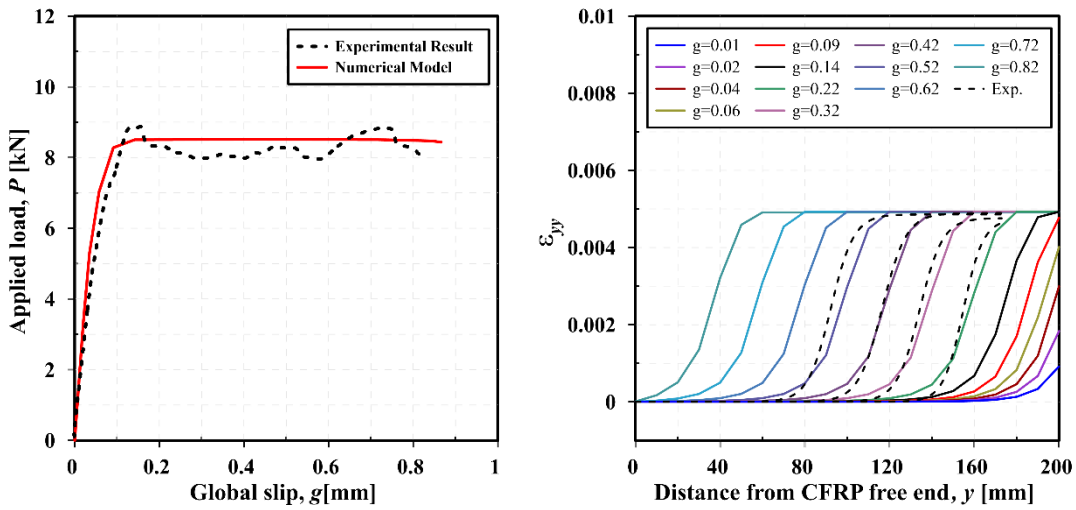

(a) *(b)*

Figure 3-29: Results of the numerical analysis for specimen DS_WD_0_4, (a) comparison of the P-g response, (b) axial strain distribution on CFRP strip

Figure 3-30 illustrates the absolute strain distribution in the CFRP-concrete joint and the development of the debonding process for specimen DS_WD_0_4 at different *g* values. At a *g* value of 0.14 mm, the CFRP-concrete joint has already attained the bond capacity (i.e., P_{est}^{num}= 8.51 kN) and debonding was already initiated at the loaded end of the CFRP-concrete joint, as shown in Figure 3-30a. Concurrently, the strain at the loaded end has reached the debonding value (i.e., ε^{num} = 0.0049) as presented in Figure 3-30a and Figure 3-29b. Comparing the debonding strain obtained from the numerical model with the value measured experimentally and reported Table 3-7 shows them equal. As the *g* further increased to 0.42mm, the load and strain at the loaded end of the joint did not further increase because they have already attained the maximum debonding values. However, the debonding process continued propagating toward the free end of the CFRP-concrete joint, as illustrated in Figure 3-30b and Figure 3-29b. Table 3-8 reports the values of the debonding strain estimated numerically (ε^{num}) for each specimen. In comparison with experimental values reported in Table 3-6 and Table 3-7, the estimated numerical values showed a considerable agreement where the relative difference was less than 6% for most specimens. Based on the presented discussion, it can be noticed that the proposed

numerical model can reasonably simulate the experimental behavior of the CFRP-concrete joint.

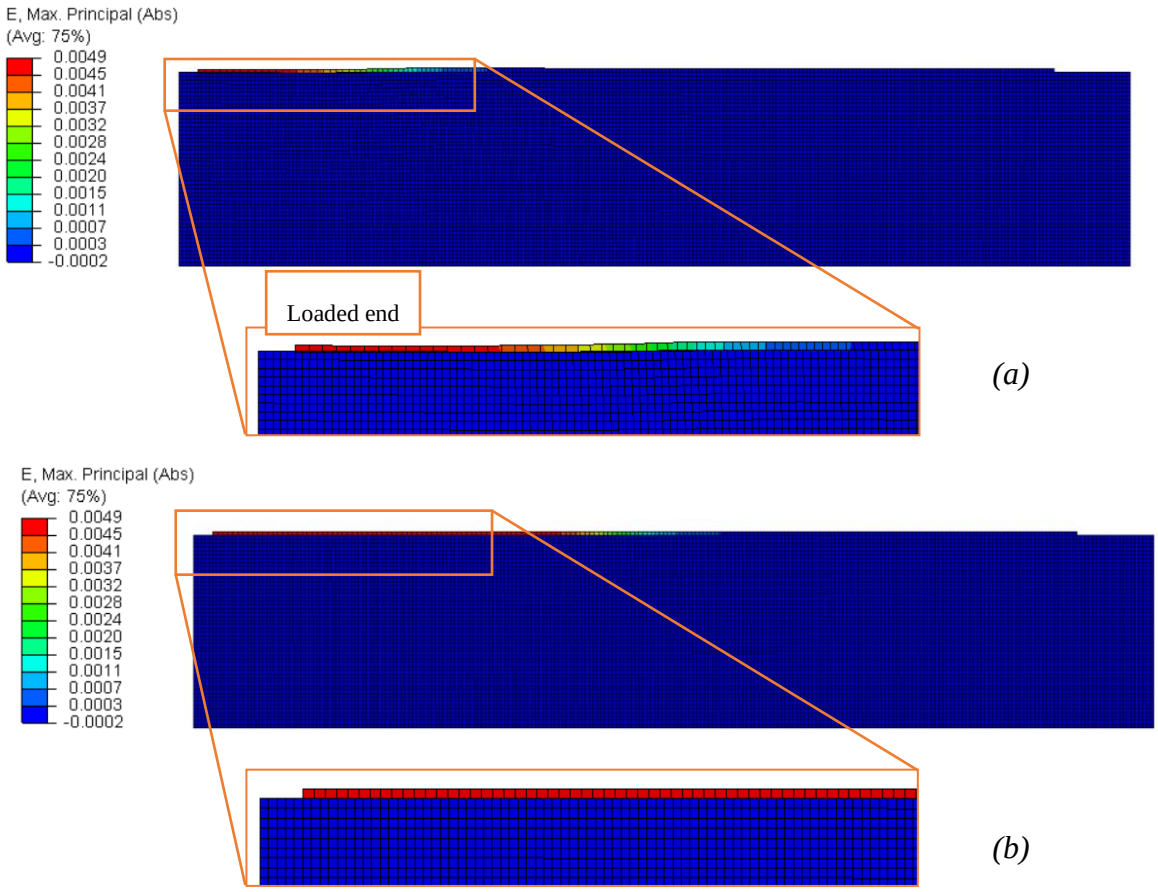

Figure 3-30: Maximum absolute strain distribution for specimen DS_WD_0_4 at various global slip g values *(a) g= 0.14 mm, (b) g= 0.42 mm*

Figure 3-31 and Figure 3-32 compare the *P-g* responses simulated numerically using the average parameters reported in Table 3-8 with an envelope of the experimental responses under the effect of the hygrothermal and wet-dry conditions, respectively. It can be noticed that the numerical model can reasonably simulate the ascending part of the curves. However, the model has overestimated the bond capacity for some conditions because it does not consider the variation of the load along the width of the interface.

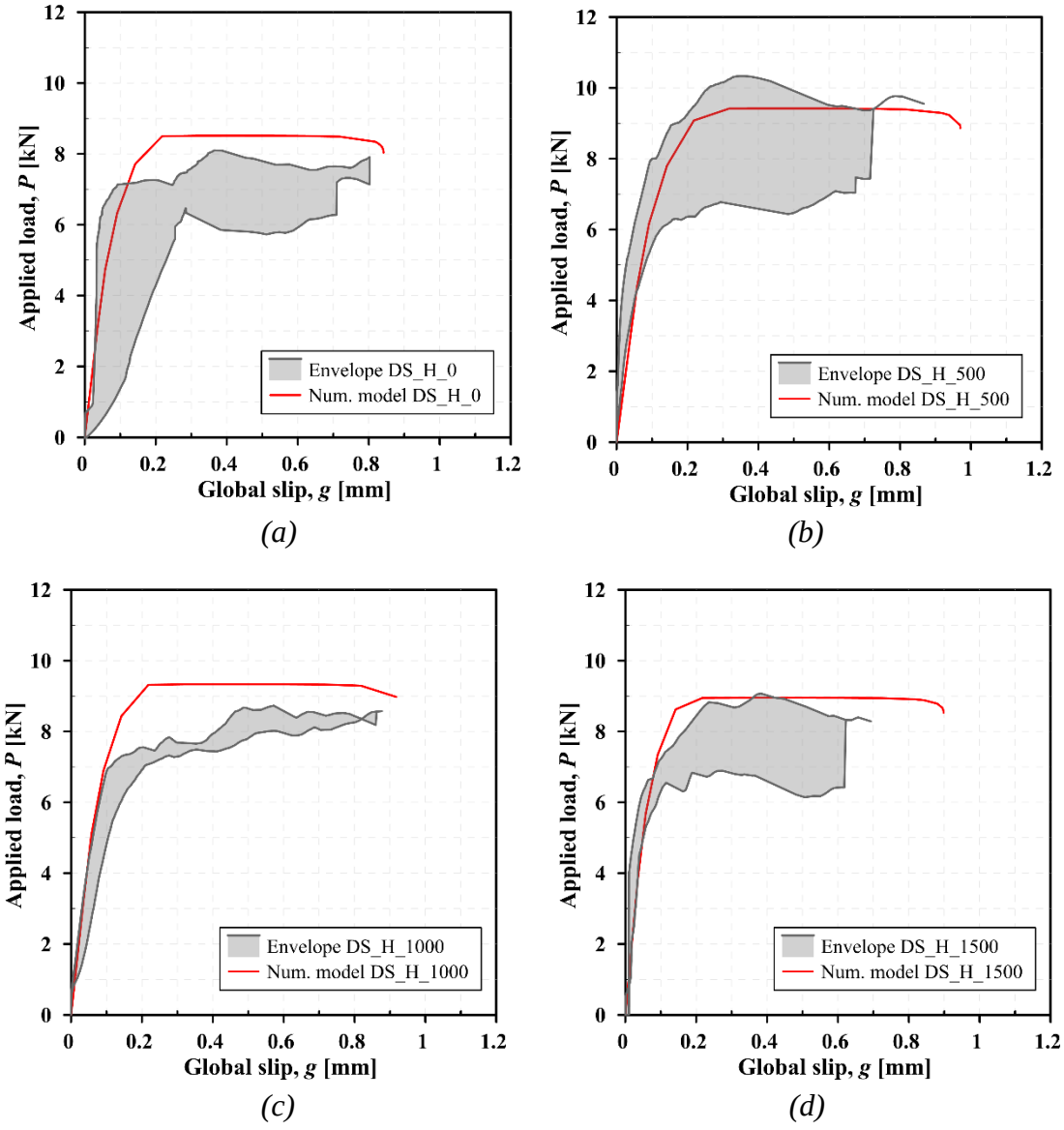

Figure 3-31: P-g response of CFRP-concrete joint under hygrothermal condition (a) reference specimens, (b) 500 h of conditioning, (c) 1000 h of conditioning, (d) 1500 h of conditioning

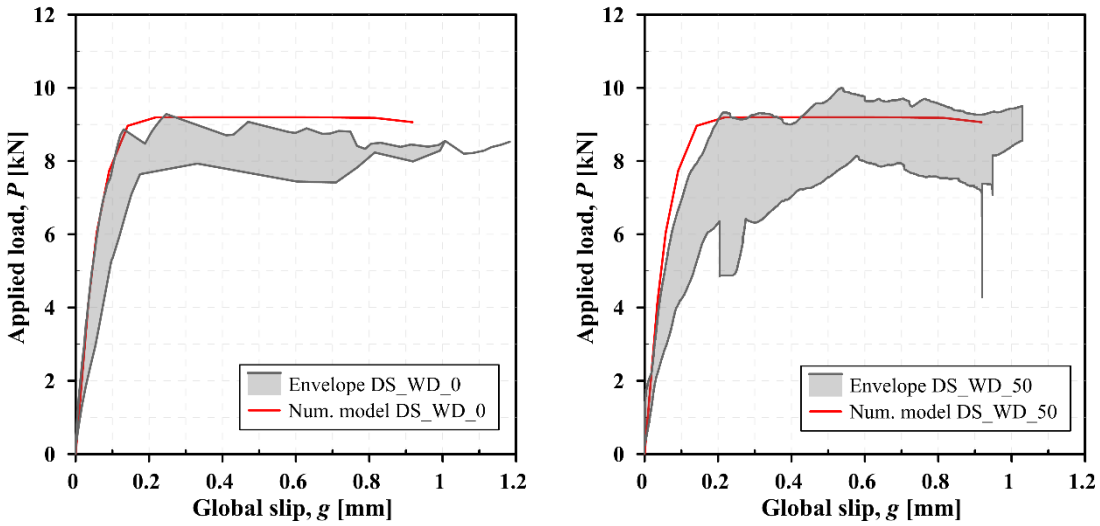

Figure 3-32: P-g response of the CFRP-concrete joint under wet-dry condition, (a) reference specimens, (b) conditioned specimens

Chapter 4: Durability of FRCM-masonry joints under the effect of wet-dry cycles

4.1 Durability of the FRCM composite

FRCM has been proposed as an alternative to the FRP composite for repairing and strengthening structures and especially masonry structures due to its compatibility, sustainability, and reversibility. Nonetheless, there is limited information available in the literature on the durability of this strengthening technique. This chapter presents an experimental study utilized to investigate the effect of the wet-dry cycles on the durability of the FRCM composites externally bonded to masonry blocks. Furthermore, the behavior of the FRCM-masonry joints analytically modeled using a trilinear CML. The wet-dry condition was investigated in this part of the research since it was not considered by the (Consiglio Superiore dei Lavori Pubblici, 2018) like other environments, such as hypothermal condition.

4.1.1 Materials and specimens assembly

Three FRCM composites and one SRG composite were studied in this part of the research. The first FRCM composite was made of carbon textile (Ruregold, 2019a), as shown in Figure 4-1a. The thickness and the width of a single fiber bundle (also referred to as yarns) t^* and b^*, respectively, are reported in Table 4-1. The bundles were spaced from each other by 5 mm in both longitudinal and transversal directions. The mechanical properties of the textile were measured by (Calabrese, D'Antino, Colombi, & Poggi, 2020) and reported in Table 4-1. The second FRCM composite was composed of PBO textile (Ruregold, 2019b), as presented in Figure 4-1b. The bundles were spaced at 5 mm from each other in the longitudinal direction and 20 mm in the transversal direction. The mechanical properties of the textile were evaluated by (T. D'Antino et al., 2014) and presented in Table 4-1. Bothe carbon and PBO textiles were embedded inside a cement-based matrix (Ruregold, 2019b). Mechanical properties of the matrix are reported in Table 4-1. The third FRCM composite was recently developed by Sika and comprised of AR-glass pre-impregnated with resin shown in Figure 4-1c and bonded to the masonry

substrate using a cement-based matrix (Sika, 2019). The bundles were spaced from each other by 17 mm, both in the longitudinal and transversal directions. The diameter of each bundle, *d**, is 1.11 mm, as reported in Table 4-1. The tensile strength and elastic modulus of the AR-glass textile were obtained by 9 tensile tests on specimens comprising 3 longitudinal (see Figure 4-1c) yarns according to (Consiglio Superiore dei Lavori Pubblici, 2018) as reported in Table 4-1. Finally, the final composite was SRG which is composed of unidirectional stainless-steel cords (TCS, 2020b) embedded in natural hydraulic lime NHL 5 (TCS, 2020a). Figure 4-1d illustrates the configuration of the textile. The cords were spaced from each other by 5 mm, and the diameter of each steel cord was 1 mm as presented in Table 4-1. Mechanical characterizations of the textile are presented in Table 4-1as reported by the manufacturer.

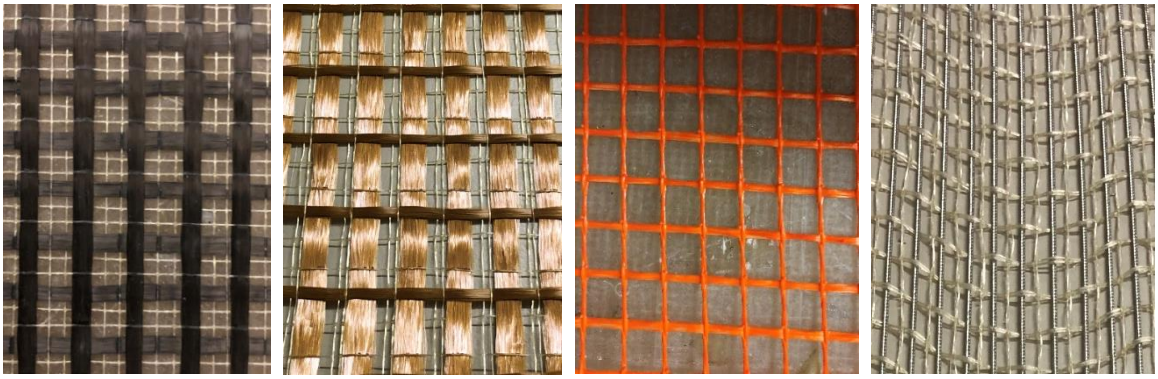

(a) *(b)* *(c)* *(d)*

Figure 4-1: FRCM fabrics and meshes; (a) carbon fabric; (b) PBO fabric; (c) AR-glass impregnated with resin; (d) stainless steel mesh

Table 4-1: Mechanical properties of the textiles and matrices

Composite	Textile properties						Matrix properties		
	d^* [mm]	b^* [mm]	t^* [mm]	f_f [MPa]	E_f [GPa]	ε_f	f_c [MPa]	f_r [MPa]	E_c† [GPa]
Carbon FRCM	-	5	0.094	1944	203	0.0095	25.0	6.1	>7.5†
PBO FRCM	-	5	0.092	3014	206	0.0145	25 .0	6.2	>7.5†
Glass FRCM	1.11	-	-	874	65	0.0134	22.0	6.0	~ 7.6†
SRG†	1.01	-	-	>2000	210	-	10.0	-	-

† = provided by the manufacturer; d^*= diameter of a single fiber bundle; b^*= width of a single fiber bundle; t^* = thickness of a single fiber bundle; f_f = tensile strength of textile; E_f = elastic modulus of the textile; ε_f = ultimate strain; f_c = compressive strength of the matrix; f_r= flexural strength of the matrix; E_c = elastic modulus of the matrix.

The FRCM composites and SRG composites were externally bonded to masonry blocks. Fourteen masonry blocks of the dimension 120 mm x 125 mm x 380 mm were constructed in this research. Each block was assembled of 6 half-bricks (Terreal Italia San Marco, 2018) bonded to each other with a 10 mm joint of cement-based mortar (FASSA BORTOLO, 2019), as shown in Figure 4-2. The compressive strength, splitting strength, and modulus of elasticity for the bricks were determined in (D'antino, Santandrea, & Carloni, 2020) by testing cylinders cored from the bricks and were 20.3 MPa, 3.12 MPa, and 7300 MPa, respectively; however, the compressive strength of the mortar was 2.5 MPa as reported by the manufacturer.

After assembly, they were placed inside a chamber at 25 ^{o}C and 90% RH for 28 days to assure complete mortar curing. At the end of the curing period, each masonry block was externally bonded with three FRCM or SRG composites, one composite on each face except the face with cut (Figure 4-2). The composites were applied at 35 mm from the edge of the masonry block to avoid edge failure due to the stress concentration. The bonded length of the composite was 300 mm and selected to be longer than the effective bond length reported in previous studies (D'Ambrisi, Feo, & Focacci, 2013; T. D'Antino et al., 2014) and recommended by the Italian initial type testing procedure (Consiglio Superiore dei Lavori Pubblici, 2018). The width of the composites was 50 mm and selected to include multiple bundles for each textile where the number of the bundles (n) was 5 for carbon, 5 for PBO, 3 for AR-glass, and 7 for stainless-steel. Before applying

each composite, the surface of the masonry block was properly moisturized to prevent it from absorbing the water of the matrix. A thin layer of 5 mm thickness, as recommended by the manufacturer (Ruregold, 2019b; Sika, 2019; TCS, 2020a), was first applied on the masonry surface. This layer was referred to as the internal layer of the composite. After that, the textile was applied over the internal layer and gently pressed on it. The textile was also extended by 20mm from the free end (i.e., the end opposite to the loaded end of the textile). This extension was used to monitor the slippage of the matrix at the free end (s_F). Finally, another thin layer of 5 mm thickness was applied over the textile. This layer was referred to as the external layer of the matrix. After applying the composites, the specimens were cured inside an environmental chamber at 25 ^{o}C and 90% RH for 28 days. Ten specimens were prepared for each type of composite. Four of them were tested at the end of the curing period and considered as reference specimens, whereas the remaining six specimens were exposed to 50 successive wet-dry cycles.

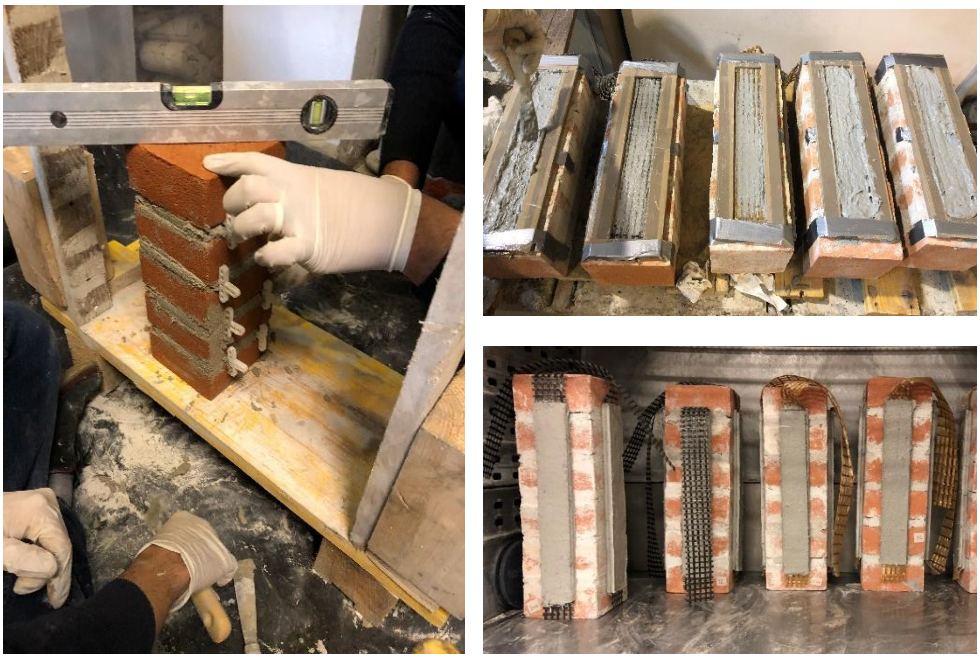

Figure 4-2: assembly of the FRCM specimens

4.2 Conditioning environment

As mentioned in chapter three, there is no specific standard to perform wet-dry cycles for FRP and FRCM. Most of the studies in the literature on FRCM durability (Donnini, 2019; Franzoni et al., 2017) have adopted lab tests to determine the wetting and drying period similar to the FRP. For instance, Donnini et al. (Donnini, 2019) utilized two days of wetting followed by two days of drying in a ventilated oven at 60^{o}C. Yin et al. (Yin et al., 2019) performed 12 hours of wetting followed by 12 hours of drying both at room temperature. Franzoni et al. (Franzoni et al., 2017) mentioned that 8 hours is an adequate period to saturate masonry blocks externally strengthened with FRCM via capillary absorption. In the drying phase, specimens are placed in a ventilated oven at 60^{o}C for two days.

The system discussed in section 3.1.2 was also utilized here to perform wet-dry cycles. Similarly, the specimens were also exposed to 50 cycles of wet-dry. Each cycle consisted of 6 hours of complete immersion in water followed by 18 hours of drying, which is selected based on preliminary tests performed on representative specimens composed of two half bricks bonded to each other with one layer of matrix, as shown in Figure 4-3a. The purpose of the preliminary tests was to determine the period required to saturate the representative specimen after being immersed in water. The weight of the representative specimen was repeatedly measured to determine the period required to reach to the saturation status. The specimen has become relatively saturated after 4 hours of wetting, where the increase in its weight by this period specimen was less than 2 grams. Similarly, for the drying phase, the weight of the specimen was continuously monitored after placing it inside the drying chamber, and the specimen lost most of the gained weight after 17 hours of drying at 50 ^{o}C.

Unlike the FRP situation, the temperature of the chamber was fixed at 50 ^{o}C during both the drying and wetting phases, as shown with the red curve of Figure 4-3b. This procedure was adopted because the specimens required a bigger chamber that was not able to alternate temperature during the wetting and drying phases. The temperature in the container, where the specimens were placed inside the chamber, was also monitored using a thermocouple, as shown with the blue curve of Figure 4-3b. At the start of the wetting

phase, the water was pumped to the container inside the chamber. Initially, the temperature of the water was around 25 ^{o}C; however, when it became in contact with specimens, which were already warm from the drying phase, it started equalizing and increased to 28 ^{o}C. Subsequently, the temperature of the water started increasing because of the warm air inside the chamber and the warm temperature of the specimens until it became 37 ^{o}C at the end of the wetting phase. At the start of the drying phase, the water was pumped out of the container in the chamber causing the temperature inside it to drop rapidly to 35 ^{o}C. Subsequently, the temperature of the air in the container increased to 42 ^{o}C. The temperature of the air inside the container continued increasing with proceeding the drying phase until it became 45 ^{o}C at the end of this phase.

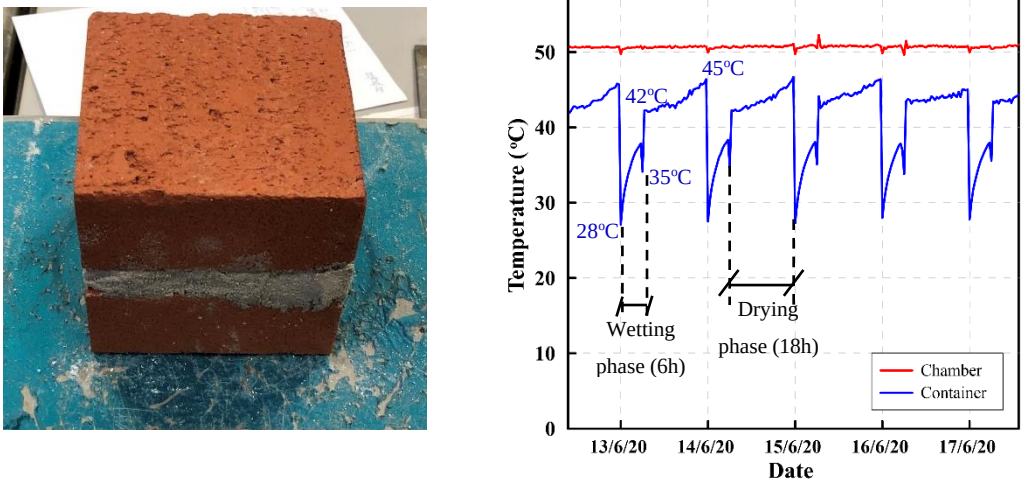

(a) (b)

Figure 4-3: wet-dry condition for FRCM, (a) representative specimens, (b) wet-dry cycles

4.3 Direct shear single-lap test

Single-lap direct-shear test (Figure 4-4) was utilized to investigate bond performance. The specimens were restrained between two steel plates connected by four threaded bars. The end of the textile mesh was bonded with two steel tabs to facilitate its gripping to the testing machine. A servo-hydraulic universal testing machine was utilized to apply the load at a rate of 0.2 mm/min at the end of the textile. The slippage of the textile mesh out of the matrix was measured relative to the adjacent substrate using Linear Variable

Displacement Transducers (LVDTs). Two LVDTs (A and B) were utilized to measure the slippage of the textile out of the matrix close to the loaded end (upper side) of the specimens, as shown in Figure 4-4. The average slip measured by these two LVDTs is called the global slip, *g*. In addition, there were two other LVDTs (C and D) attached close to the free end of the specimens (bottom side) used to record the slippage of the textile to the matrix when the debonding reach close to the free end and called free end slip, s_F. The LVDTs acted against two angles mounted on the loaded and free ends of the textile mesh, as shown in Figure 4-4.

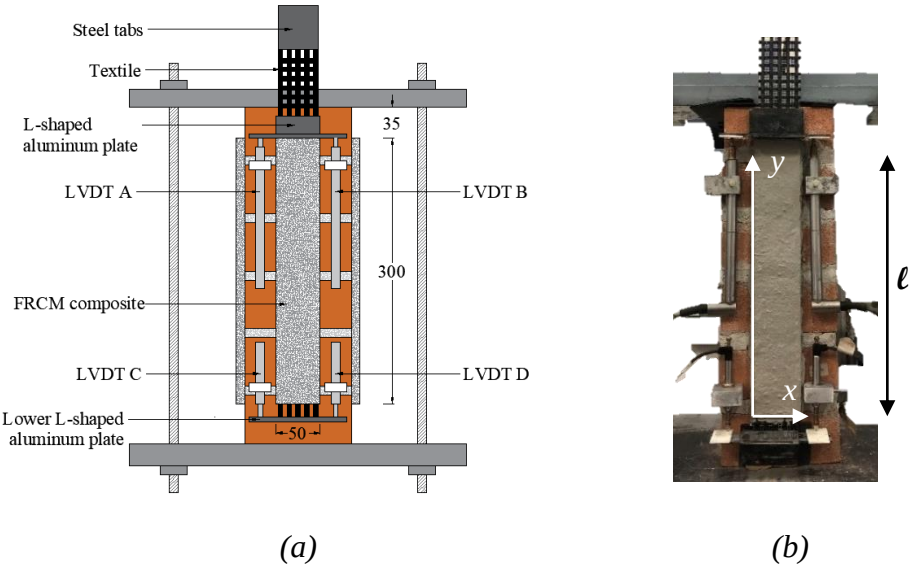

Figure 4-4: Single-lap shear test, (a) sketch of the setup, (b) photo of specimen DS_300_50_C_R_3 with the reference system

4.4 Results and discussion

At the end of the wet-dry cycles, the dry specimens were removed out of the chamber and left in the lab temperature (25 ^{o}C) for one week; after that, they were tested in the dry condition. The specimens were named following the notation DS_300_50_X_Y_i, where DS referred to the type of the test (Direct Shear), 300 indicated the bonded length of the composite (in mm), 50 indicated the bonded width of the composite b_1, X referred to the type of the composite (C= Carbon, P= PBO, G= AR-Glass, and S= SRG), Y referred to

the conditioning statues (R= Reference specimens, C= Conditioned specimens), and i referred to the number of the specimen.

4.4.1 Visual inspection and failure modes

At the end of the conditioning period, specimens were visually inspected to determine any changes. Small spots of salt accumulation in the form of efflorescence were detected on the matrix, bricks, and mortar, as shown in Figure 4-5. Since the water used to condition the specimens was tap water without or with a relatively low salt concentration, it was implied that salt has already existed in small concentration within the utilized materials. Small salt accumulation was also observed in the matrix-substrate interface after debonding. It is essential to mention that no signs of severe deterioration in the form of flacking or crumbling were detected on the composites or the masonry bricks. Similar finding was also reported by Franzoni et al (Franzoni et al., 2017).

Four failure modes were noticed in the tested specimens. To differentiate each mode from another, they were named following the notation J_z, where *J* referred to the failure mode (*D*= Debonding failure, *R*= Rupture failure within fiber, and *M*= Mixed failure mode), and subscript *Z* referred to the position of failure (*m*=within the matrix, *s*=within the substrate, *ms*=at the matrix-substrate interface, and *mf*=at the matrix-fiber interface). Figure 4-6 illustrated the four failure modes developed in this study. The first failure mode was a debonding in the matrix-substrate interface (D_{ms}) (Figure 4-6a). The second mode was debonding in the matrix-fiber interface (D_{mf}), which was characterized by slipping the textile out of the matrix (Figure 4-6b). The third mode was a mixed failure of debonding in the matrix-fiber interface followed by textile rupture ($MD_{mf}R$), as shown in Figure 4-6c. Finally, the last failure mode was a mixed debonding failure in the matrix-substrate interface and matrix-fiber interface ($MD_{mf}D_{ms}$), as shown in Figure 4-6d.

(a) (b) (c)

Figure 4-5: Salt accumulation in specimens, (a) DS_300_50_K_C_5, (b) DS_300_50_P_C_4 (c) DS_300_50_C_C_4

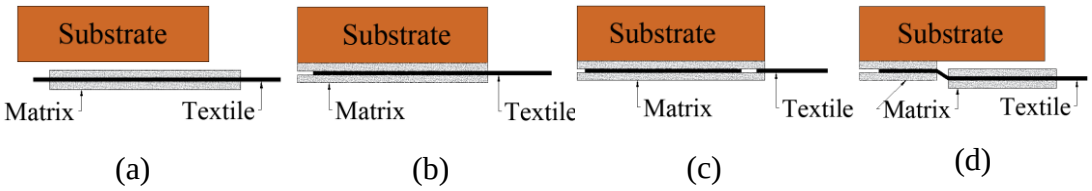

Figure 4-6: Failure modes, (a) debonding within the matrix-substrate interface (Dms), (b) debonding within the matrix-fiber interface (Dmf), (c) mixed debonding within the matrix-fiber interface and fiber rupture (MDmfR), (d) mixed debonding failure within the matrix-substrate and matrix-fiber interfaces (MDmfDms).

4.4.2 Bond durability of carbon FRCM-masonry joints.

Two failure modes were observed in the reference specimens. The first and most common mode was D_{mf}, which was developed in 3 specimens. The second mode was $MD_{mf}D_{ms}$ and developed in specimen DS_300_50_C_R_1. It was initiated by slipping the textile out of the matrix; subsequently, a crack was developed in the middle of the composite, as shown in Figure 4-7a. After that, the upper half of the composite was debonded from the substrate while the lower remained bonded as the textile continued slipping out of it. After conditioning, three failure modes were noticed. The first mode was D_{mf}, which was developed in DS_300_50_C_R_2. The second mode was a brittle failure of D_{ms} (Figure

4-7b) and observed in specimens DS_300_50_C_R_1 and 4. The last mode was $MD_{mf}R$, which was noticed in specimens DS_300_50_C_R_3, 5 and 6.

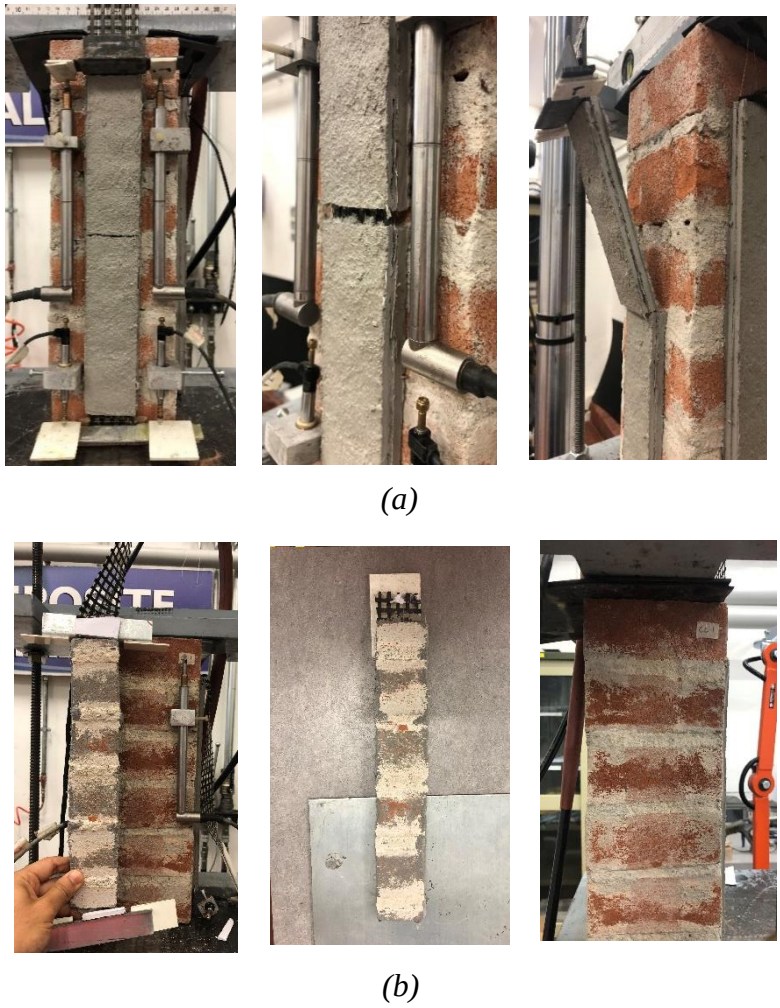

(a)

(b)

Figure 4-7: Failure modes of carbon FRCM-masonry joints (a) mixed debonding failure ($MD_{mf}D_{ms}$) for specimen DS_300_50_C_R_1, (b) debonding with the matrix-substrate (D_{ms}) for *specimen DS_300_50_C_C_1*

Table 4-2 reports the failure mode, FM, of each specimen. In addition, the results of the peak load P^*, corresponding average peak load $\bar{P}^*$, ultimate stress σ^*, and corresponding average ultimate stress $\bar{\sigma}^*$ were also reported. The ultimate stress σ^* was determined using Eq.(4-1):

$$\sigma^* = \frac{P^*}{n\, t^*\, b^*} \tag{4-1}$$

where n is the number of longitudinal yarns within the composite strip width; t^* is the thickness of textile bundles as reported in Table 4-1; b^* is the width of the bundle.

Applied load- global slip (P-g) response and shear stress- global slip (σ-g) response are shown in Figure 4-8. In addition, the applied load vs. free end slip (P-s_F) and shear stress vs. free end slop (σ-s_F) are also presented with a dotted line whenever it has existed. All the reference specimens presented in Figure 4-8a had approximately an initial linear P-g response. As the load increased and approached the peak value, the stiffness of the P-g curves started slightly decreasing due to the slippage of the textile bundles out of the matrix. However, the load continued increasing until it reached the peak value due to the friction (interlocking) between the matrix and the textile. At the peak load value, STZ has already reached the free end of the composite, as confirmed with P-s_F (Figure 4-8a). After that, the load started softening and gradually decreasing until the residual applied load attained (Figure 4-8a). At this point, the textile has completely debonded from the matrix, and friction was the only load transfer mechanism.

Figure 4-8b presents P-g, σ-g, P-s_F, and σ-s_F responses of the conditioned specimens. Similarly, all the specimens had an initial linear P-g response. Both DS_300_50_C_C_2 and 6 had a comparable response to the reference specimens. However, for specimen DS_300_50_C_C_6, the s_F was developed after P-g response had already decreased, which could possibly indicate the development of fiber rupture inside the composite before attaining the s_F. Furthermore, it can be noticed that the value of the s_F is relatively smaller than g, which is be attributed to the rotation of the lower L-shaped aluminum plate (Figure 4-9) causing the lower LVDTs to read opposite values. The rotation of the lower L-shaped aluminum plate could be possiby ascribed to few reasons: (i) uneven debonding

at both sides of the composite, (ii) rupture of some fibers inside the composite on one side, making debonding propagate on the other side, (iii) uneven load distribution at both sides of the composite.

In comparison with reference specimens, the $\bar{\sigma}^*$ of these two specimens (DS_300_50_C_C_2 and 6) was increased by 17%. This increment could be attributed to the continuation of the hydration process, which enhanced the mechanical interlocking between matrix and textile.

Specimens DS_300_50_C_C_1 and 4 showed a different response in which the load was suddenly dropped from the peak value to zero after developing a pre-mature failure of debonding within the matrix-substrate interface (D_{ms}). In comparison with reference specimens, the average ultimate stress for these two specimens was slightly decreased by 7%. Since this reduction is relatively small and lies within the scatter of the results, it could be ignored.

Regarding the last two specimens (DS_300_50_C_C_3 and 5), the stiffness of the *P*-g curve started decreasing as the load increased and approached the peak value due to the slippage of the textile from the matrix. At the peak value, the load had a sharp drop which could be attributed to rupture of fibers inside the matrix since there are no signs of fibers rupture in the unbonded part of the textile (i.e., the part of textile utilized to transfer the load from the machine to the composite) and the s_F was null. After that, the load continued decreasing as the g increased until it reached zero, where the test was suspended. It is worth mentioning that s_F was null during the whole test, indicating that STZ has never reached the free end of the composite, and load decrement could be ascribed to the rupture of fibers inside the matrix. Comparing the average ultimate stress of these two specimens with the average ultimate stress of the reference specimens indicated a significant increment of 33%. This increment could be mainly ascribed to the increase in the bond strength after conditioning which favored rupture failure over complete debonding.

Finally, Figure 4-10 illustrated the effect of the wet-dry cycles on $\bar{\sigma}^*$ before and after conditioning. The scatter of the data was shown as an error bar. Generally, it can be noticed that $\bar{\sigma}^*$ was increase by 14%. In addition, CoV was increased from 8.7% to 14.7% due to the alteration in the failure modes.

Table 4-2: Direct shear test results for the FRCM

Specimen Name	P^* (kN)	$\overline{P^*}$ (kN)	σ* (MPa)	$\overline{\sigma^*}$ (MPa)	$P_b{}^*$	$\overline{P_b}^*$	FM
DS_300_50_C_R_1	2.42		1152		484		$MD_{mf}D_{ms}$
DS_300_50_C_R_2	2.46	2.37	1171	1130	49.2	47.5	D_{mf}
DS_300_50_C_R_3	2.58	(8.7)	1229	(8.7)	51.6	(8.7)	D_{mf}
DS_300_50_C_R_4	2.03		967		40.6		D_{mf}
DS_300_50_C_C_1	2.23		1062		44.6		D_{ms}
DS_300_50_C_C_2	2.67		1269		53.3		D_{mf}
DS_300_50_C_C_3	3.08	2.71	1468	1290	61.7	54.2	$MD_{mf}R$
DS_300_50_C_C_4	2.17	(14.7)	1034	(14.7)	43.4	(14.7)	D_{ms}
DS_300_50_C_C_5	3.21		1531		64.3		$MD_{mf}R$
DS_300_50_C_C_6	2.89		1376		57.8		$MD_{mf}R$
DS_300_50_P_R_1	5.67	4.80	2465		113.4		D_{mf}
DS_300_50_P_R_2	4.66		2026	2086	93.2	96.0	D_{mf}
DS_300_50_P_R_3	5.01	(13.7)	2178	(13.7)	100.2	(13.7)	D_{mf}
DS_300_50_P_R_4	3.85		1674		77.0		D_{mf}
DS_300_50_P_C_1	4.01		1743		80.2		$MD_{mf}R$
DS_300_50_P_C_2	4.37	4.46	1900	1939	87.4	89.2	$MD_{mf}R$
DS_300_50_P_C_3	5.07	(7.8)	2205	(7.8)	101.4	(7.8)	$MD_{mf}R$
DS_300_50_P_C_5	4.35		1891		87.0		$MD_{mf}R$
DS_300_50_P_C_6	4.49		1954		89.9		$MD_{mf}R$
DS_300_50_G_R_1	1.77		634	661	35.4		$MD_{mf}R$
DS_300_50_G_R_2	1.69	1.85	606	(6.43)	33.8	36.9	$MD_{mf}R$
DS_300_50_G_R_3	1.95	(6.4)	699		39.0	(6.4)	$MD_{mf}R$
DS_300_50_G_R_4	1.97		706		39.4		$MD_{mf}R$
DS_300_50_G_C_1	1.66		596		33.3		$MD_{mf}R$
DS_300_50_G_C_2	1.70		610		34.0		$MD_{mf}R$
DS_300_50_G_C_3	1.79	1.71	641	612	35.8	34.2	$MD_{mf}R$
DS_300_50_G_C_4	1.56	(5.6)	557	(5.4)	31.1	(5.6)	$MD_{mf}R$
DS_300_50_G_C_5	1.86		666		37.2		$MD_{mf}R$
DS_300_50_G_C_6	1.69		604		33.7		$MD_{mf}R$
DS_300_50_S_R_1	4.36		793		87.2		D_{ms}
DS_300_50_S_R_2	5.28	5.14	961	934	105.6	102.7	D_{ms}
DS_300_50_S_R_3	5.2	(9.5)	946	(9.5)	104	(9.5)	$MD_{mf}R$
DS_300_50_S_R_4	5.7		1037		114		$MD_{mf}R$
DS_300_50_S_C_1	4.91		894		98.3		D_{ms}
DS_300_50_S_C_2	3.38		614		67.5		D_{ms}
DS_300_50_S_C_3	4.02	3.73	732	679	80.5	74.6	D_{ms}
DS_300_50_S_C_4	2.71	(30.4)	493	(30.4)	54.2	(30.4)	D_{ms}
DS_300_50_S_C_5	2.09		380		41.8		D_{ms}
DS_300_50_S_C_6	5.26		957		105.2		$MD_{mf}R$

P^*= peak-load value; $\overline{P^*}$ = average peak load value; s^*= ultimate stress; $\overline{\sigma^*}$= averge ultimate stress; $P_b{}^*$= peak load per unite width; $\overline{P_b}^*$= averge peak load per unite width; FM= failure mode.

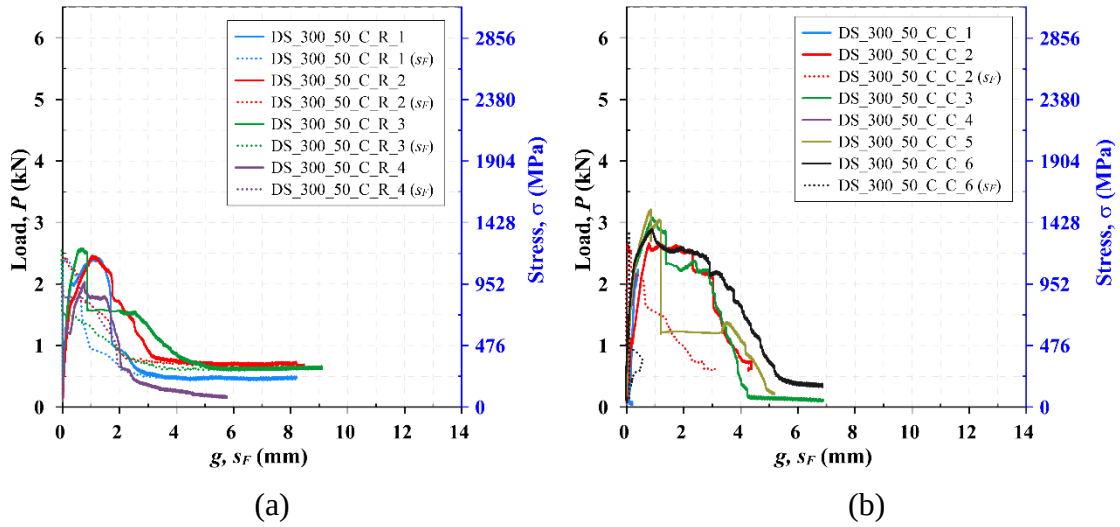

Figure 4-8: P-g response for the carbon FRCM-masonry joints, (a) reference specimens, (b)conditioned specimens

Figure 4-9: Failure developed in specimen DS_300_50_C_C_6

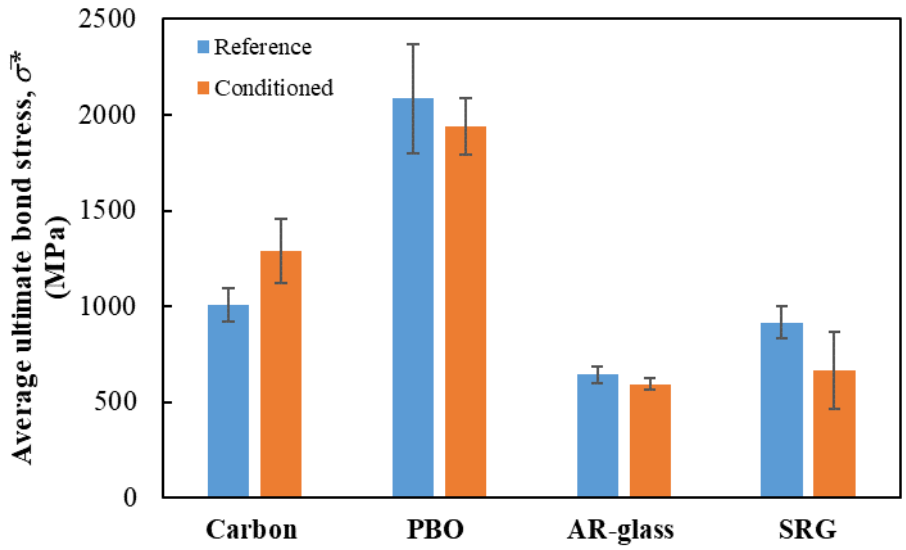

Figure 4-10: effect of the wet-dry cycles on the bond strength.

4.4.3 Bond durability of PBO FRCM- masonry joints

All the reference specimens developed D_{mf} failure. Unlike carbon FRCM, it was accompanied by numerous transversal macro cracks developed on the external matrix layer, as shown in Figure 4-11. In addition, a longitudinal crack was also detected in the internal-external matrix layer interface (matrix interlaminar crack), which sometimes led to detachment of the external layer (Figure 4-11). After exposing to wet-dry cycles, all the specimens developed a mixed debonding failure within the matrix-fiber interface followed by fiber rupture ($MD_{mf}R$). Regarding specimens DS_300_50_P_C_1 and 5, fiber rupture was noticed in the unbonded part of the textile (i.e., the part of textile utilized to transfer the load from the machine to the composite). However, for specimens DS_300_50_P_C_2,3 and 6, fibers rupture was speculated to be developed in the bonded part of the textile (i.e., inside the matrix). Finally, since specimens DS_300_50_C_P_4 developed a pre-mature failure of fiber rupture in the unbonded part of the textile, the result of this specimen was neglected. Table 4-2 illustrates the failure modes developed in each specimen.

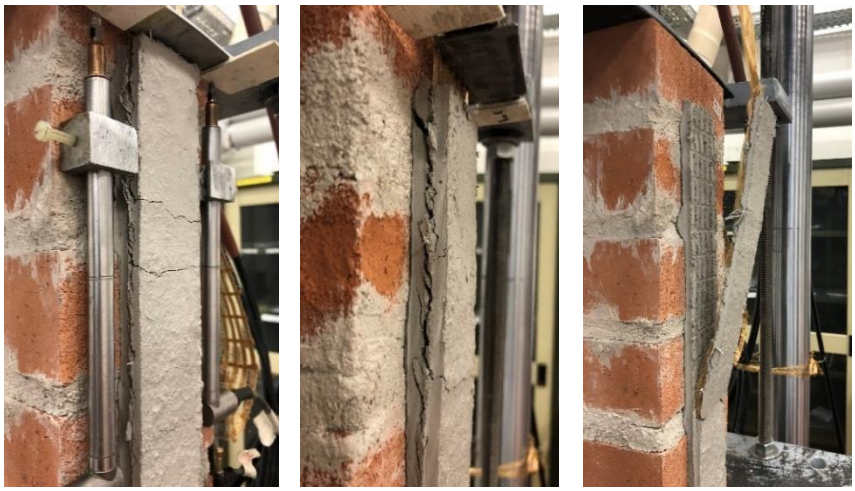

Figure 4-11: D_{mf} failure accompanied with macro cracks noticed on PBO FRCM of specimen DS_300_50_P_R_3

P-g response, σ-*g* response, σ-s_F, and *P*-s_F response of the reference and conditioned specimens are presented in Figure 4-12. The reference specimens had an initial linear behavior; nonetheless, it was interrupted with some oscillation because of the cracks developed on the layers of the matrix. As the load increased and approached the peak value, the response became non-linear after slipping the textile from the matrix of the composite. At this point, STZ has reached to free end of the composite, as determined with the *P*-s_F. After that, the load started decreasing until the residual applied load was attained, where the textile completely debonded from the matrix, and friction was the only load transfer mechanism.

After conditioning, two responses were identified depending on the location of the fiber rupture. The first response was observed in specimens DS_300_50_P_C_2,3 and 6, which had a comparable ascending load response to the reference specimens (Figure 4-12b). However, after attaining the peak value, the load started decreasing, yet the s_F was null. Concurrently, previously developed transversal cracks on the external layer of the matrix started closing, indicating rupture of some fibers inside the matrix. Although some of the fibers were ruptured, the remaining unruptured fiber continued slipping into the matrix at the free end of the composite, as determined from the *P*-s_F. However, the value of the s_F was noticeably lower than *g* due to the reasons discussed in section 4.4.2 (i.e., rotation of

the lower angle). After that, the load continued decreasing as the value of *g* increased, and finally, the test was suspended when the load almost vanished.

The second response was noticed in DS_300_50_P_C_1, and 5, which also had a comparable ascending *P*-g response to the reference specimens. At the peak load value, the STZ reached the free end of the composite, as confirmed with *P*-s_F. Subsequently, some of the fibers in the unbonded part of the textile started losing their strength and rupturing, causing the *P*-*g* response to dropping to zero with no further increase in *g*.

Figure 4-10 illustrates the effect of the wet-dry cycles on the average ultimate stress. It can notice that $\bar{\sigma}^*$ was decreased by 7%. Furthermore, the CoV was decreased from 13.7% to 7.8%. Since the reduction in the $\bar{\sigma}^*$ was falling within the scatter of the data, it can consider that wet-dry cycles had a trivial effect on the bond between PBO FRCM and masonry substrate.

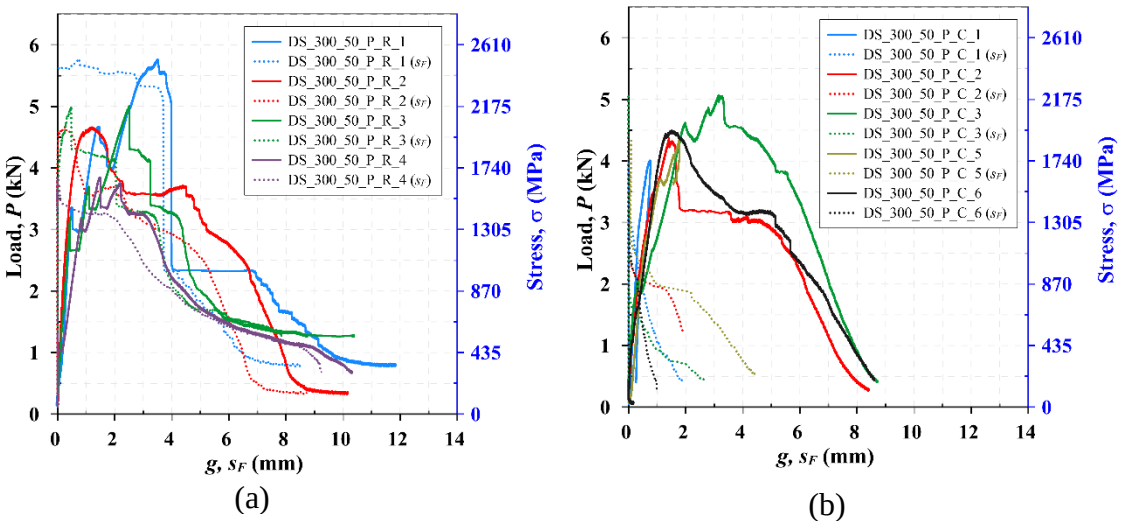

(a) (b)

Figure 4-12: P-g response for PBO FRCM-masonry joints, (a) reference specimens, (b) conditioned specimens

4.4.4 Bond durability of AR-glass FRCM-masonry joints

All the reference and conditioned specimens developed a $MD_{mf}R$ failure. This failure mode started by slipping the textile out of the FRCM matrix, followed by rupture of the fibers, as shown in Figure 4-13a. Although fibers' rupture for most of the specimens was

developed in the textile bundles embedded inside the matrix, for some of the conditioned specimens, it was recognized in the unbonded part of the textile (Figure 4-13b).

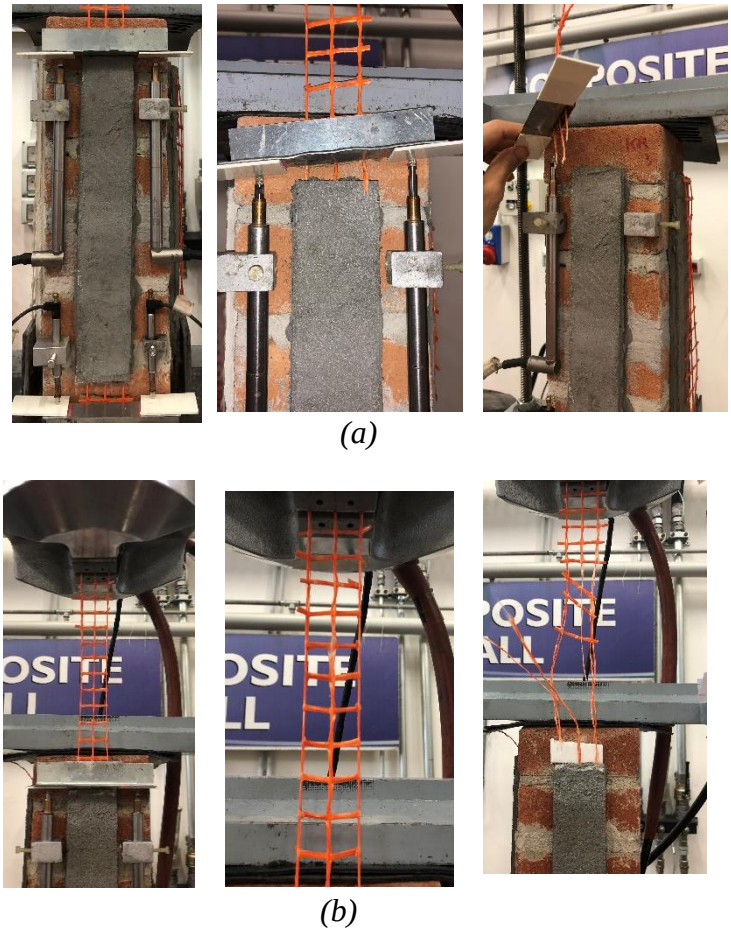

Figure 4-13: $MD_{mf}R$ failure developed in glass FRCM-masonry joints (a) fiber rupture failure developed in the bonded part of the textile for specimens DS_300_50_G_R_3, (b) fiber rupture developed in the unbonded textile yarns of specimen DS_300_50_G_C_2.

Figure 4-14 presents the *P-g*, σ-*g*, σ-s_F, and *P*-s_F responses of the reference and conditioned specimens. Both reference and conditioned specimens had an initial linear performance like the previous two composites. As the load increased, the stiffness of the *P-g* curve decreased, and the response changed to non-linear due to the slippage of the textile from the matrix. Nevertheless, the load continued increasing until it reached the peak value due to the friction between the textile and the matrix. At the peak value, STZ has reached the free end of the composite, as confirmed with *P*-s_F. After that, the load took

a horizontal path until the fibers started rupturing, making the load drop sharply. The load kept decreasing as the fibers ruptured until it became null, where the test was suspended. It is worth mentioning that for specimen DS_300_50_G_C_1 fiber rupture was initiated first within one of the bundles before STZ reached the free end of the composite.

The effect of the wet-dry cycles on the $\bar{\sigma}^*$ is presented in Figure 4-10. The average ultimate stress was decreased by 7%. In comparison with other composites, the results of the AR-glass FRCM had the lowest scatter, which was ranging between 6.2% for the reference specimens and 5.4% for the conditioned specimens. This low value could be attributed to the consistency in the failure mode.

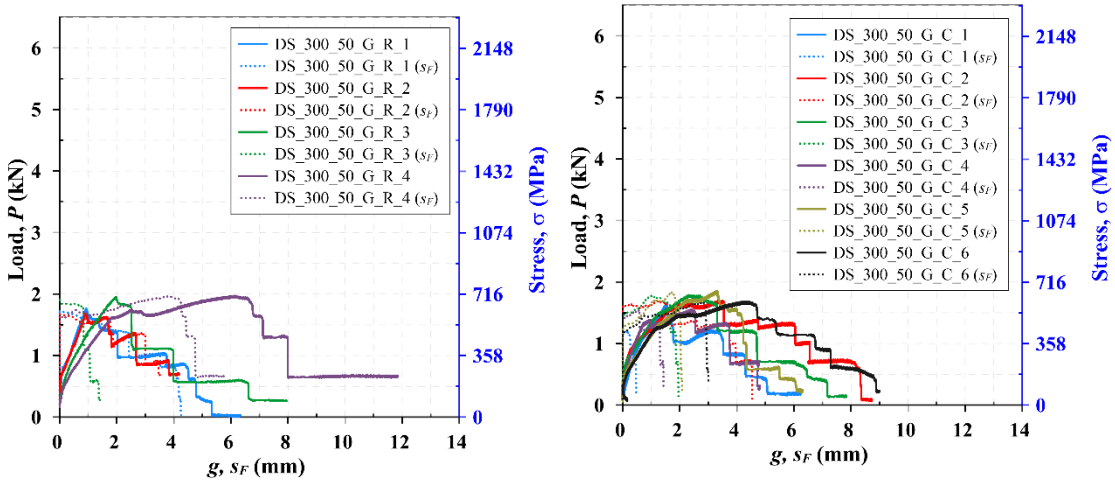

(a) (b)

Figure 4-14: P-g response for glass FRCM-masonry joints, (a) reference specimens, (b) conditioned specimens

4.4.5 Bond durability of SRG-masonry joints

Two failure modes were observed in the reference and conditioned specimens. The first mode was D_{ms}, which was sometimes preceded by a macro crack noticed on the layers of the matrix, as shown in Figure 4-15a. This failure mode was observed in two reference specimens (DS_300_50_S_R_1 and 2). However, after conditioning, the number of specimens developed in this failure mode was increased to five (DS_300_50_S_C_1-5), as illustrated in Table 4-2. The second failure mode was $MD_{mf}R$, as shown in Figure 4-15b.

This failure mode was observed in two of the reference specimens (DS_300_50_S_R_3 and 4) and one of the conditioned specimens (DS_300_50_S_C_6).

(a)

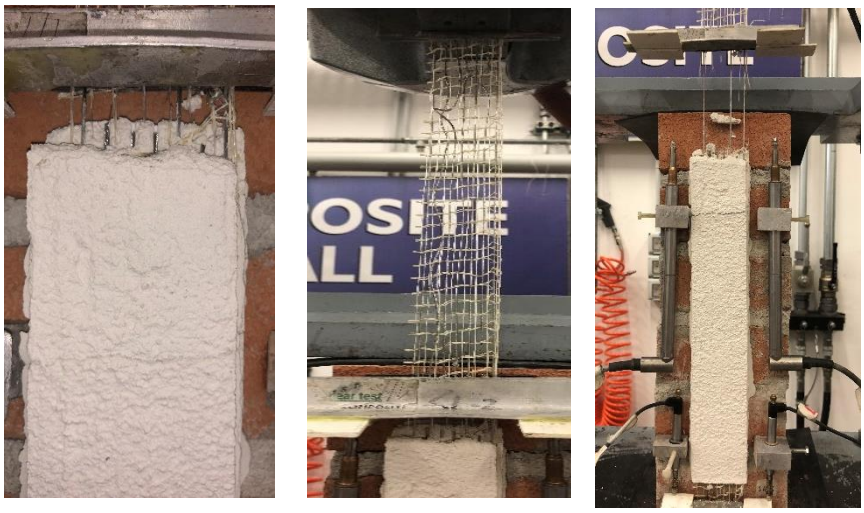

(b)

Figure 4-15: Failure modes developed in the masonry blocks externally bonded with SRG, (a) D_{ms} failure mode in specimen DS_300_50_S_R_1, (b) $MD_{mf}R$ failure mode in specimen DS_300_50_S_R_3.

P-g, σ-*g*, σ-s_F, and *P*-s_F responses for SRG-masonry joints are present in Figure 4-16. Both reference and conditioned specimens had two responses depending on the failure mode. The first response was observed in the specimens with D_{ms} failure. Regarding the reference specimens, they had an initial linear response. The stiffness of the *P-g* curve slightly decreased as the load increased and approached the peak value due to the slippage

of the steel cords, as confirmed with cracks noticed on the external and internal layers of the matrix. At the peak load value, the SRG composite detached from the masonry block, and the load dropped to zero. Nonetheless, s_F was null, indicating that matrix-fiber debonding was only occurred close to the loaded end of the composite and did not propagate to the free end of the composite. After conditioning, a comparable response was detected in specimens DS_300_50_S_C_1 and 3. However, for specimens DS_300_50_S_C_2, 4 and 5, the failure was developed prematurely with no cracks occurred on the matrix layers. In comparison with the reference specimens, the average peak load of the conditioned specimens that developed a D_{ms} failure was decreased by 29%, indicating the significant effect of the wet-dry cycles on the bond between SRG composite and masonry substrate.

The second response was noticed in the specimens with $MD_{mf}R$. Both reference and conditioned specimens had a similar behavior which was characterized by an initial linear performance. As the load increased and approached the peak value, the steel cords started slipping out of the matrix, causing a slight decrement in the stiffness of the *P-g* curve. At the peak load value, the response has already changed to non-linear, and the steel cords of the textile started rupturing, causing rapid drops in the load, as can be noticed in the descending part of the *P-g* response presented in Figure 4-16. The load continued decreasing due to the rupture of other cords as the global slip was increased. Finally, the residual applied load was attained as the remaining unruptured steel cords started sliding out of the matrix, as confirmed with the *P*-s_F response. However, since the s_F was only developed on one side of the composite, the average s_F was smaller than *g* due to the rotation of the lower L-shaped aluminum plate. Regarding DS_300_50_S_C_6, it was not presented in Figure 4-16 because of an error that occurred during the test that prevented the lower LVDTs to recorded it. Comparing the results of the reference specimens with conditioned specimens for this failure mode indicated a minor change in the peak load value.

Figure 4-10 illustrates the effect of the wet-dry cycles on the average ultimate stress. The $\bar{\sigma}^*$ was decreased by 27%. In addition, CoV was increased from 9.5 % to 30.4 %. These

results reveal the significant effect of wet-dry cycles on the bond durability between SRG composite and masonry substrate.

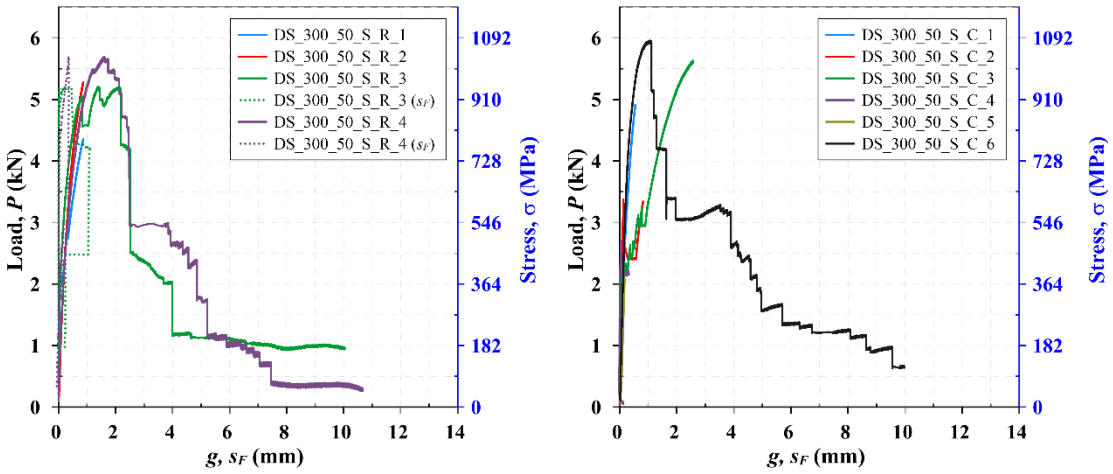

Figure 4-16: P-g response of the SRG, (a) reference specimens, (b) conditioned specimens

4.4.6 Comparison of bond performance for the various composites

In this section, the bond performance of the different composites is compared in term of peak load per unite width $P_b^* = P^*/b_1$ and corresponding average peak load per unit width $\overline{P_b}^*$ (see Table 4-2). Peak load per unite width is an engineering property utilized to compare the behavior of the FRCM systems that have different equivalent thicknesses. However, when it comes to selecting an FRCM system over another, other parameters should also be considered, such as composite stiffness, strength, cost, compatibility with the substrate, and textile layout (unidirectional, bidirectional, and multidirectional).

Figure 4-17 compares the $\overline{P_b}^*$ of the four systems. The scatter of the data was presented as an error bar. Before conditioning, SRG-masonry joints had the highest value of 103 kN/m, and AR-glass FRCM-masonry joints had the lowest value of 37 kN/m. Comparing the average peak load per unite width with average ultimate stress (Figure 4-10), it can be noticed that the behavior of the carbon FRCM and PBO FRCM have not been significantly affected. However, the peak load per unite width of the SRG composite was increased. This increment is ascribed to the higher equivalent thickness of stainless-steel mesh (t = 0.113 mm). The peak load per unite width of the AR-glass FRCM was also

increased, yet it remained lower than the other systems. Similar finding was also reported in the literature (de Felice, D'Antino, De Santis, Meriggi, & Roscini, 2020).

After conditioning, the average peak load per unite width deteriorated for PBO, AR-glass, and SRG composites, yet it was improved in the case of carbon FRCM. It can be noticed the deterioration in the case of SRG was higher than the other composites, which were decreased by 27% after exposure to wet-dry cycles. This implies the critical role of durability in choosing a specific composite for another for intervention applications.

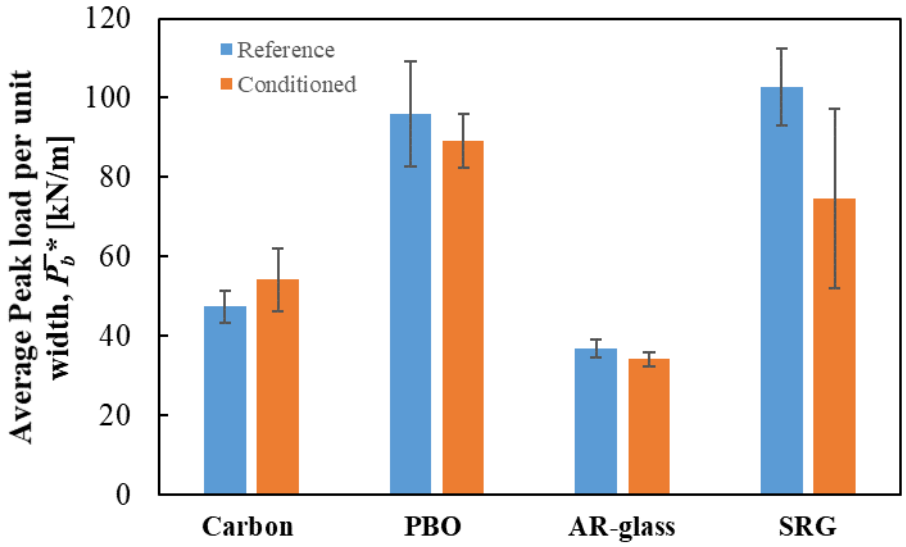

Figure 4-17: Comparison of the bond performance of various FRCM systems based on average load per unite width strength

4.5 Analytical modeling of FRCM-masonry joints

The result of the direct shear test presented in chapter 4 indicated that FRCM-masonry joints could have various failure modes depending on the type of FRCM system (carbon, steel, AR-glass, and PBO) and on the conditioning environment. One of these failure modes was debonding in the matrix-fiber interface. This failure mode is more ductile than the debonding failure in the matrix-substrate interface because of the friction and slippage phenomena between the filaments of the yarns and between the matrix and yarns.

The are several factors that play an essential role in the analysis of the bond behavior for the FRCM-masonry joints, such as mechanical properties of the matrix, textile, and impregnation of the two components. Since the last factor can have a significant role in characterizing the interfacial bond properties, factors such as chemical properties of the fiber surface and granular size of the matrix are considered very important in the analysis of the bond properties.

In this part of the research, the result obtained from the experimental campaign was modeled using the analytical approach developed by (Tommaso D'Antino et al., 2018). A trilinear CML was adopted to describe the bond behavior of the FRCM-masonry joint. To accurately calibrate CML, a *P-g* response associated with the debonding at the matrix-fiber interface or matrix-substrate interface should be utilized. Consequently, the analytical approach was employed to model carbon and PBO FRCM developed a debonding failure in the matrix-fiber interface. Regarding the glass FRCM and SRG composites which showed a rupture failure or a mixed-mode failure, though the calibration of the CML could be possible, yet more tests with various bond length are needed to understand the effect of fiber rupture and mixed-mode failure and to obtain a reliable calibration of the CML.

4.5.1 Bond-slip model

The bond-slip model or the trilinear CML (Figure 4-18) utilized in this part of the research is composed of an ascending elastic branch followed by a descending softening branch and ends with a horizontal friction branch. The elastic branch has slop k_1 that ends when the maximum interface strength τ_{max} is attained (or equivalently when the s_o was reached). The softening branch has a slop k_2 that ends when the shear stress achieves the value of τ_f (or equivalently when the slip achieves the value of s_f). It is worth mentioning that there are some simpler CML, e.g., bilinear elastic-fragile (Calabrese, Colombi, & D'Antino, 2019) or rigid-softening (Calabrese et al., 2019), utilized to study the bond behavior of the FRCM composites. However, the accuracy of these models is less than the trilinear model.

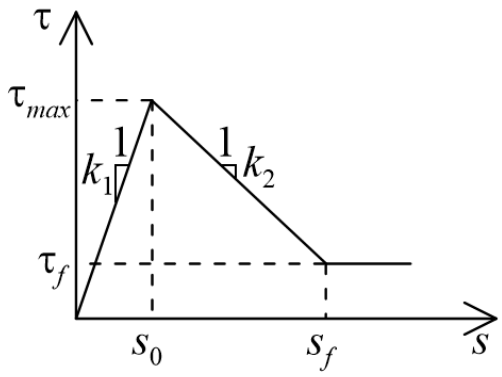

Figure 4-18: Trilinear CML

The following assumptions are made to obtain the governing equations of the problem: (i) pure mode-II loading condition is considered at the matrix-fiber interface; (ii) matrix and substrate are rigid (i.e. they have no deformation); (iii) composite has no width effect; (iv) textile has a linear elastic behavior until failure (T. D'Antino et al., 2014; Wu et al., 2002). The carbon and PBO textiles used in this research are assumed to have yarns with rectangular cross-sections with a width b^* much bigger than the thickness t^* (i.e., $p \cong 2b^*$, where p is the matrix–fiber contact perimeter of a single yarn). Particularly, both textiles have b^* = 5mm while the value of t^* is 0.094 for carbon and 0.092 for PBO (Table 4-1). Based on these assumptions, the differential equation that describes the distribution of the shear stress τ(y) and slip s(y) in the matrix-fiber interface is:

$$\frac{d^2s}{dy^2} - \frac{2}{E_f t^*}\,\tau = 0 \qquad (4\text{-}2)$$

Where E_f is the elastic modulus of the textiles as reported in Table 4-1 and y is the coordinate along the bonded length, ℓ, with the origin of the reference system located at the free end of the composite (i.e., $y=0$ at the free end and $y=\ell$ at the loaded end as illustrated in Figure 4-4b. Solving equation (4-2) using a specific CML and applying appropriate boundary conditions (Tommaso D'Antino et al., 2018) provides the interface shear stress τ(y), axial fiber strain $\varepsilon(y)$ (or equivalent fiber applied stress σ(y)=$E_f . \varepsilon(y)$), and slip $s(y)$ for each point of the load response.

Considering FRCM-masonry joint with a bonded length longer than the minimum length needed to fully develop stress transfer mechanism (effective bond length l_{eff}), the load

response can be divided into five stages as shown in Figure 4-19: (i) elastic; (ii) elastic-softening; (iii) elastic-softening debonding; (iv) softening debonding; (v) fully debonded stage. In the first stage (i), the behavior of the whole interface is elastic. At the end of this stage, the fiber applied stress $\sigma(\ell)$, and the global slip $s(\ell)$ at the loaded end are named σ_A and g_A, respectively. As the shear stress at the loaded end exceeds the τ_{max} value and starts decreasing after entering the softening branch of the CML, the load response becomes non-linear and stage (ii) (elastic softening stage) begins. In this stage, the interface has two parts. The first part is associated with softening branch of the CML and has a length l, while the second part is associated with the elastic branch and has a length of ℓ-l, as shown in Figure 4-19. The fiber applied stress at the end of this stage is debonding stress $\sigma_{deb.}$ In the third stage (elastic-softening debonded stage), part of the interface with a length d has debonded; nonetheless, the stress at the loaded end did not drop to zero and a stress value of $2\tau_f d/t^*$ still transferred. The remaining part of the interface is still under the elastic-softening stage in which the length of the portion associated with softening branch of the CML is l and the length of the portion associated with the elastic branch of the CML is ℓ-l-d, as illustrated in Figure 4-19. In stage (iv) (softening-debonding stage), the interface has only two parts. The first part is the debonded portion and has a length of d while the second part is associated with softening branch of the CML and has a length of ℓ-d. The fiber applied stress at the end of this stage is ascribed to the friction only and equals to $\sigma_f = 2\tau_f \ell/t^*$. In the last stage (v), the whole interface is debonded while the axial stress in the fiber is constant and equals σ_f as the global slip increases. The solution of equation (4-2) for each of these stages is presented in Table 4-3.

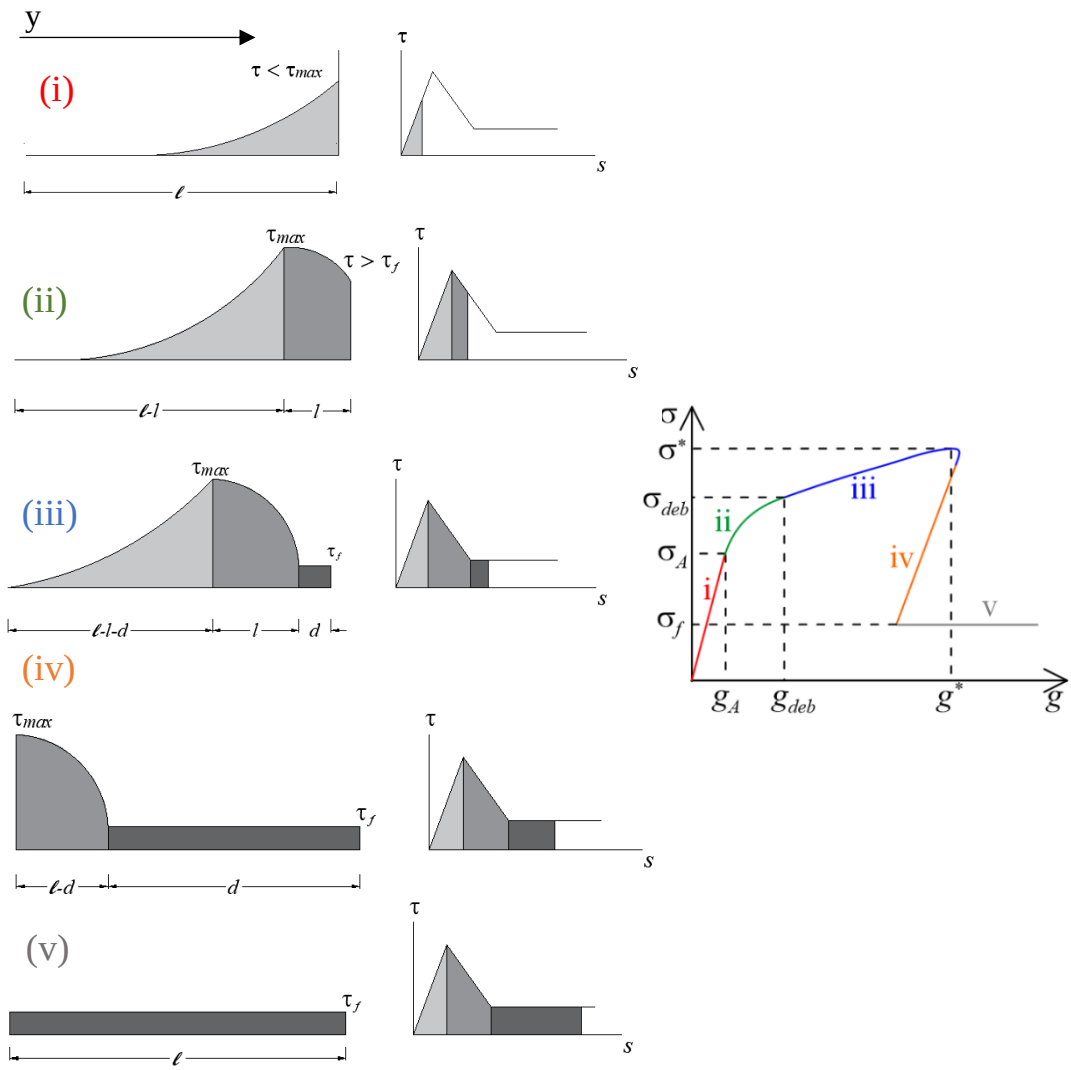

Figure 4-19: interfacial shear stress distribution and stages of the load response development.

Table 4-3: solution of equation (4-2) for each stage of Figure 4-19

Elastic stage i.	
$s(y) = \frac{\sigma t^* \lambda}{2k_1} \frac{\cosh(\lambda y)}{\sinh(\lambda \ell)}$; $\varepsilon(y) = \frac{\sigma t^* \lambda^2}{2k_1} \frac{\sinh(\lambda y)}{\sinh(\lambda \ell)}$; $\tau(y) = \frac{\sigma t^* \lambda}{2} \frac{\cosh(\lambda y)}{\sinh(\lambda \ell)}$	$0 \le y \le \ell$
Elastic-softening stage ii.	
$s(y) = s_0 \left\{\frac{\lambda}{\omega}\tanh[\lambda(\ell - l)]\sin[\omega(y - \ell + l)] - \frac{k_1}{k_2}\cos[\omega(y - \ell + l)] + \frac{k_1 k_2}{k_2}\right\}$ $\varepsilon(y) = \omega s_0 \left\{\frac{\lambda}{\omega}\tanh[\lambda(\ell - l)]\cos[\omega(y - \ell + l)] + \frac{k_1}{k_2}\sin[\omega(y - \ell + l)]\right\}$ $\tau(y) = -\tau_{\tau max} \left\{\frac{\omega}{\lambda}\tanh[\lambda(\ell - l)]\sin[\omega(y - \ell + l)] - \cos[\omega(y - \ell + l)]\right\}$	$\ell - l \le y \le \ell$
Elastic-softening-debonding stage iii.	
$s(y) = \frac{\tau_f}{E_f t^*}(y^2 - 2\ell y + l^2 - d^2) + \frac{\sigma}{E_f}(y - \ell + d) + s_f$ $\varepsilon(y) = \frac{2\tau_f}{E_f t^*}(y - \ell) + \frac{\sigma}{E_f}$; $\tau(x) = \tau_f$	$\ell - l \le y \le \ell$
Softening-debonding stage iv.	
$s(y) = \frac{\omega}{k_2}\left[\tau_f d - \frac{\sigma t^*}{2}\right]\frac{\cos(\omega y)}{\sin[\omega(\ell - d)]} + \tau_{max}\frac{k_1 + k_2}{k_1 k_2}$ $\varepsilon(y) = \frac{\omega^2}{k_2}\left[\frac{\sigma t^*}{2} - \tau_f d\right]\frac{\sin(\omega y)}{\sin[\omega(\ell - d)]}$ $\tau(y) = \omega\left[\frac{\sigma t^*}{2} - \tau_f d\right]\frac{\cos(\omega y)}{\sin[\omega(\ell - d)]}$	$0 \le y \le \ell - d$
Fully debonded stage v.	
$s(y) = \frac{\tau_f}{E_f t^*}(y^2 - 2\ell y) + \frac{\sigma}{E_f} y + s_f$ $\varepsilon(y) = \frac{2\tau_f}{E_f t^*}(y - \ell) + \frac{\sigma}{E_f}$ $\tau(y) = \tau_f$	$0 \le y \le \ell$

Note: $\omega = \sqrt{\frac{2k_2}{(E_f t^*)}}$; $\lambda = \sqrt{\frac{2k_1}{(E_f t^*)}}$; E_f= textile Young's modulus; t^*= thickness of a yarn; k_1, k_2, s_f, and τ_f are parameters of the CML (see Figure 4-18).

4.5.2 Effective bond length

It was discussed in the previous section that the stress transfer mechanism is associated with the elastic-softening stage. Based on this fact, the effective bond length can be determined by equating the loaded end slip in stage (ii) (see Table 4-3) to s_f.

$$l_{eff} = l + \frac{1}{\lambda}\operatorname{arctanh}\left[\frac{\lambda}{\omega \sin(\omega l)} \cdot \left(\cos(wl) - \frac{\tau_f}{\tau_{max}}\right)\right] \tag{4-3}$$

Since the adopted CML requires an infinite bonded length to fully develop the elastic stage (Focacci & Carloni, 2015), l (i.e., the length of the softening portion) can be evaluated by enforcing axial stress for $\ell = l_{eff}$ equal to a certain fraction α of the axial stress associated with an infinite bonded length (Tommaso D'Antino et al., 2018; Jianguo Dai, Ueda, & Sato, 2006; Yuan, Teng, Seracino, Wu, & Yao, 2004):

$$l = \frac{2}{\omega}\arctan\left[\frac{\frac{\alpha\omega}{\xi} - \sqrt{\left(\frac{\tau_f}{\tau_{max}}\right)^2 + \left(\frac{\alpha\omega}{\xi}\right)^2 - 1}}{\frac{\tau_f}{\tau_{max}} + 1}\right] \tag{4-4}$$

Where:

$$\xi = \frac{\omega}{\sqrt{1 + \frac{\omega^2}{\lambda^2}}} \tag{4-5}$$

4.5.3 Calibration of the trilinear CML

Four conditions are needed to fully define trilinear CML, which is characterized by four of the parameters: s_0, τ_{max}, s_f, τ_f, k_1, k_2, and fracture energy (i.e., the area under the elastic-softening branch, $G_F = 0.5[s_f(\tau_{max}+\tau_f) - \tau_f s_0]$, see Figure 4-18). Out of the several possible methods to define these conditions, in this study, the parameters of the CMLs were calibrated by enforcing the axial stress σ_A and corresponding global slip g_A at the end of the elastic stage (i), the debonding stress σ_{deb}, and the friction stress σ_f (Figure 4-19). The average of these parameters detected on load responses in Figure 4-8 and

Figure 4-12 allowed to calibration of the CML of the carbon and PBO FRCM, respectively. The shear stresses τ_{max} and τ_f and corresponding slips s_0 and s_f obtained for the two CMLs are reported in Table 4-4.

Table 4-4: Parameters of the trilinear CMLs of the carbon and PBO FRCM

Specimen	s_0 [mm]	τ_{max} [MPa]	s_f [mm]	τ_f [MPa]	G_F [N/mm³]	l_{eff} [Eq. (4-3)] [mm]	l [Eq.(4-4)] [mm]
DS_300_50_P_R	0.30	0.80	0.98	0.07	0.416	220	88
DS_300_50_P_C	0.30	0.80	0.86	0.05	0.360	208	77
DS_300_50_C_R	0.12	0.54	0.36	0.04	0.102	163	63
DS_300_50_C_C	0.12	0.54	0.60	0.03	0.167	189	102

Figure 4-20 compares the trilinear CMLs estimated for PBO and carbon FRCM with non-linear CML measured experimentally by (T. D'Antino et al., 2014) using closely spaced strain gauges placed on the textile. Regarding the PBO FRCM-masonry joints, it can be noticed that the ascending part of the trilinear CML of the reference specimens is identical to the conditioned specimens, as implied from the *P-g* response (Figure 4-12). However, the stiffness of the descending part was decreased after conditioning due to the decrement in the bond capacity and subsequently the fracture energy of the interface (section 4.4.3). Comparing the trilinear CML to the non-linear one, implying that they are relatively close to each other though the matrix used in this study is different from the one utilized by (T. D'Antino et al., 2014). It is worth mentioning that the matrix utilized by (T. D'Antino et al., 2014) had an average compressive strength of 28.4 MPa, and it was designed to be applied on concrete substrate. However, the matrix used in this had an average compressive strength of 25 MPa (Table 4-1) and was designed to be used with a masonry substrate. The slight difference between the two CMLs implies that the method utilized to construct the trilinear CML is quite effective in capturing the main characteristics of the matrix-fiber interface. Furthermore, the matrix strength does not have a significant effect on the definition of the CML.

Figure 4-20 also presents the trilinear CMLs of the reference and conditioned carbon FRCM-masonry joints. Similarly, the ascending parts of the CMLs for the reference and conditioned specimens were identical. Nonetheless, the stiffness of the descending part

was increased after conditioning because of the increase in the fracture energy of the interface (section 4.4.2).

It can be noticed from Figure 4-20 that carbon FRCM has lower maximum shear stress and corresponding slip in comparison with PBO FRCM (Figure 4-20). Furthermore, the debonding of the carbon fiber was developed at an s_f = 0.36mm and s_f = 0.60mm for reference and conditioned specimens, respectively, which is lower than the values obtained for the PBO (s_f = 0.96mm and s_f = 0.86mm, respectively). Consequently, the fracture energy of the carbon FRCM was approximately 25%-50% of the PBO CML, which entitles for a debonding stress σ_{deb} of the carbon FRCM equal to 50% of that of a corresponding PBO FRCM with the same geometrical properties (Santandrea, Focacci, Mazzotti, Ubertini, & Carloni, 2020).

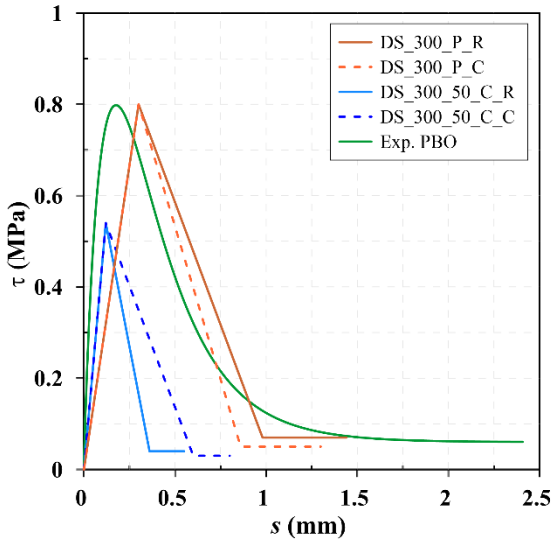

Figure 4-20: comparison between trilinear CMLs calibrated for PBO and carbon FRCM and the non-linear CML measured on PBO FRCM-concrete joint by (T. D'Antino et al., 2014)

The effective bond length l_{eff} and the length of the softening part l for the carbon and PBO FRCM were determined using equations (4-3) and (4-4), respectively, assuming $\alpha = 0.99$ (C. Carloni, D'Antino, Sneed, & Pellegrino, 2015). It can be noticed from Table 4-4 that the effective bond length of PBO FRCM was decreased after conditioning, which is

ascribed to the decrement in the bond capacity and subsequently the fracture energy of the interface. However, the opposite is true for the case of the carbon FRCM (Table 4-4)

The obtained results (shown in Table 4-4) also indicated that the difference in the l_{eff} of the reference carbon FRCM and PBO FRCM was around 26%; nonetheless, this difference was a decrease to 9% after exposure to the wet-dry condition due to the decrement in the l_{eff} of PBO FRCM and the opposite for the carbon FRCM. This difference (i.e., 9%) is relatively small considering the difference in the CMLs presented in Figure 4-20. However, results in the literature showed that evaluating the effective bond length of the FRCM composites based on the single-bonded length might provide misleading results (C. Carloni et al., 2015). Therefore, more studies are advised to confirm the obtained values of the l_{eff} in this work.

4.5.4 Analytical load response

After estimating the CMLs, the load response can be simulated using the equations reported in Table 4-3. Figure 4-21 and Figure 4-22 compares the analytical load response simulated based on the estimated trilinear CMLs with the envelope of the experimental responses (see Figure 4-8 and Figure 4-12) for the carbon FRCM and PBO FRCM, respectively. Although the experimental results had an obvious scatter, which is often reported in the literature (T. D'Antino et al., 2014; Franzoni et al., 2018; Sneed, D'Antino, & Carloni, 2014), the analytical load response matched well the experimental envelop responses up to the peak load. Regarding the post-peak behavior of the analytical response, it was characterized by the presence of the snap-back; nonetheless, the global slip continued increasing for the experimental response. This difference in the behavior is attributed to the control mode utilized in performing experimental tests where the global slip was enforced to monotonically increase during the entire test. Further details regarding the occurrence of snap-back in analytical and experimental FRP- and FRCM-substrate joints can be found in (Calabrese et al., 2019; Carrara & Ferretti, 2013).

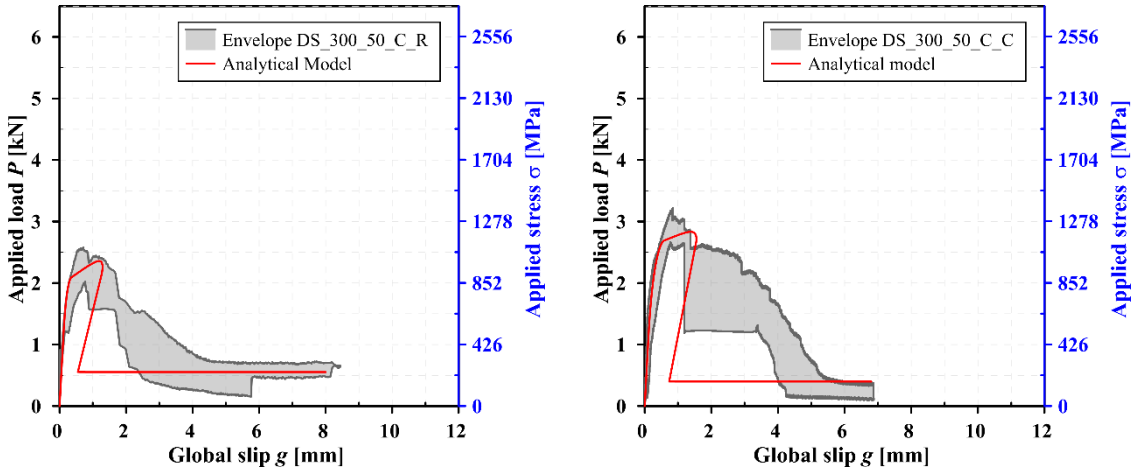

Figure 4-21: load response comparison of the analytical and experimental (envelope) of carbon FRCM, (a) reference, (b) conditioned

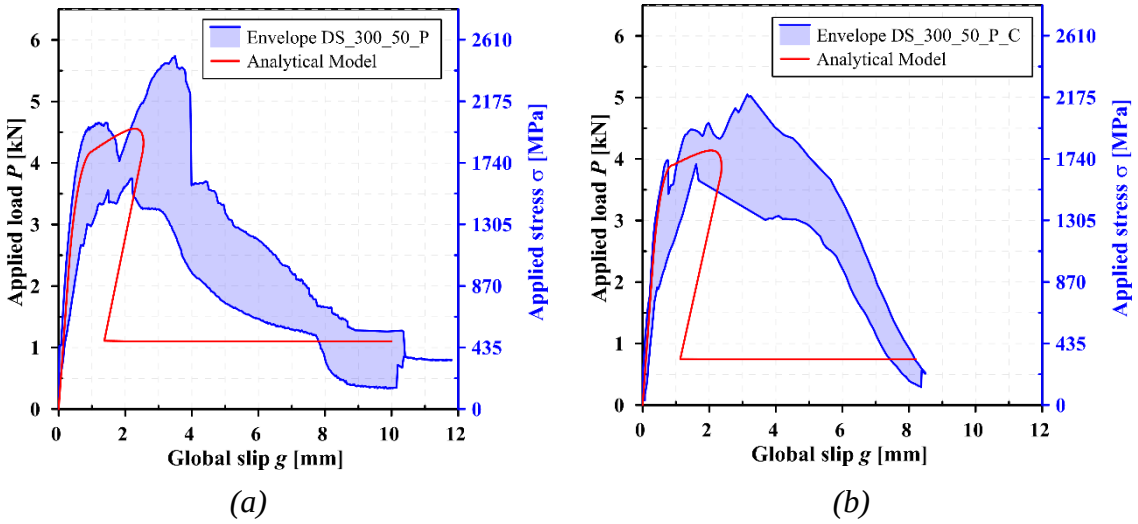

Figure 4-22: load response comparison of the analytical model with the envelope of the experimental results for the PBO FRCM, (a) reference, (b)conditioned

Chapter 5: Conclusions

5.1 Problems and accomplished objectives

After an extensive review of the available literature, a significant gap was identified in the durability of the FRP and FRCM composite systems. For instance, in the case of FRP composite, despite the numerous studies dedicated to investigating mechanical properties of the FRP composite and bond characteristics of the FRP-concrete interface, extremely limited numbers have focused on the G_F of the FRP-concrete joint after exposing to the environmental conditions such as the hygrothermal environment. The situation for FRCM and SRG composites was even worse due to the variation in the types of these composites, which could behave differently from each other in various environments. Nonetheless, there is only a limited number of studies on the durability performance of these composites.

The objective of this dissertation was to fill part of the gap about the durability of the FRP and FRCM. An experimental program consisted of two parts was conducted. The first part focused on the effect of the hydrothermal and wet-dry conditions on the bond characteristics of the CFRP-concrete joint. DIC technique was utilized to evaluate CML and fracture energy of the interface. Subsequently, the CMLs were calibrated using the finite element method so they could be utilized in a future parametric study aiming to evaluate the effect of various concrete strength and FRP materials under the investigated conditions (i.e., hygrothermal and wet-dry conditions)

The second part of the research was dedicated to investigating the durability of the FRCM and SRG composites externally bonded to masonry substrate under the effect of the wet-dry conditions. The FRCM composites consisted of one layer of carbon, PBO, or AR-glass embedded between two layers of cement-based matrices. The SRG system was composed of unidirectional stainless-steel cords embedded in a lime-based matrix. The specimens were exposed to 50 cycles of wet-dry. The bond performance of these composites was evaluated using a direct-shear single-lap shear test. Finally, the behavior of the carbon and PBO FRCM was modeled by solving the bond differential equation with a trilinear CML.

5.2 Remarks on the durability of the CFRP

The effect of the hygrothermal and wet-dry conditions on the CFRP-concrete joint and constituent materials (epoxy resin and CFRP strip) was experimentally investigated in this research. After that, the experimentally measured CML laws were numerically calibrated so they could be implemented in future models aimed to evaluate the durability of the RC structures externally bonded with CFRP.

The hygrothermal condition had some visible changes on the epoxy resin, where its color was changed from dark grey into light grey. In addition, some of the specimens had a small deformation after drying. The tensile strength of the epoxy resin was increased with the proceeding of the conditioning period until it reached the plateau after 1000 hours of conditioning. The overall behavior of the epoxy resin specimens was changed from linear to non-linear. It was implied that the hygrothermal environment has a conflicting effect on the epoxy resin. On the one hand, it stimulates the post-curing process. On the other, it can cause plasticization, deformation and swelling in the epoxy resin.

Unlike epoxy resin, the overall behavior of the CFRP strip was not affected by the conditioning environment. This finding indicated that the performance of the CFRP strip was dominated by the behavior of the carbon fibers, which have better durability (Benzarti, Freddi, & Frémond, 2011) than the epoxy resin. Nonetheless, it worth mentioning that color changing from dark gray to light grey was also noticed in the case of the CFRP coupons.

The effect of the hygrothermal and wet-dry conditions on the CFRP-concrete joint was investigated using the direct-shear single-lap test. The hygrothermal condition did not significantly affect the failure mode of the joint. Nonetheless, wet-dry conditions shifted failure mode from a debonding failure within the concrete substrate to an adhesive failure in the interface or a mixed failure. Furthermore, wet-dry cycles slightly reduced the stiffness of the joint. However, both conditioning environments did not have a significant effect on the load-carrying of the joint.

The behavior of the CFRP-concrete joint under the effect of the hygrothermal and wet-dry conditions was also numerically simulated using the 2D model. The model effectively simulated the behavior of the joint.

Finally, CNR-DT 200 (CNR, 2013) and ACI 440.2R (American Concrete Institute, 2017) have recommended reducing tensile strength and rupture strain of the CFRP exposed to the outdoor environment by 15%. Based on the findings of this experiment, this value could be conservative. However, more studies are needed with more extended conditioning periods, different conditioning environments, and different FRP materials to validate the reduction factor.

5.3 Remarks on the durability of the FRCM and SRG composites

Bond durability between masonry blocks and FRCM composites was studied in the second part of this research. Three types of FRCM composites and one type of SRG composite were investigated. FRCM composites were made of three types of textiles, namely carbon, PBO, and AR-glass pre-impregnated with reins. They were bonded to the masonry blocks with two types of cement-based matrices. The SRG composite was made of stainless-steel cords bonded to the masonry blocks with a lime-based matrix. The specimens were exposed to 50 cycles of wetting and drying.

At the end of the wet-dry cycles, some visible changes were identified. Small salt accumulation in the form of efflorescence was recognized on the external surfaces of composites and bricks. Small salt accumulation was also recognized in the interface between matrix and substrate of the specimens developed a debonding failure. It was believed that the salt has already existed in the used material since the water used in the wetting phase was tap water without or with minimal salt concentrations.

Failure mode and load-carrying capacity were also influenced by the wet-dry cycles. Regarding masonry block externally bonded with carbon FRCM, two of the conditioned specimens developed a debonding failure in the matrix-substrate interface, which was not observed within the reference specimens. Although the peak load of these two specimens was decreased in comparison with the reference specimens, the average peak load of all the conditioned specimens was increased, indicating that wet-dry cycles can have a contradicting effect on this type of composite. On one side, it enhances the bond strength by the resumption of the hydration process for cement-based matrix. On the other, it can shift failure mode to the matrix-substrate interface, causing a slight reduction in the bond strength.

The behavior of the PBO FRCM-masonry joint was different from the previous composite system. After conditioning, all the specimens developed a mixed debonding failure within the matrix-fiber interface followed by fiber rupture. The average peak load of the conditioned specimens was decreased by 7%, which was considered insignificant since it falls within the scatter of the data.

The performance of the masonry blocks externally bonded with AR-glass FRCM composite was consistent where all the specimens (i.e., control and conditioned) developed a mixed debonding failure in the matrix-fiber interface followed by fiber rupture. Due to the consistency in the failure mode, the scatter was relatively small. The average peak load was reduced by 8%, which could be ascribed to the effect of the wet-dry cycles on the mechanical properties of the textile itself.

Wet-dry cycles had a noticeable effect SRG-masonry joint, where the number of the specimens that developed a debonding in the matrix-substrate interface was significantly increased after conditioning. Furthermore, the average peak load was decreased by 27% and the scatter of the data was increased.

The results of the carbon and PBO FRCM were modeled using an analytical approach based on the solution of the bond differential equation using a trilinear cohesive material law. The analytical load response had a decent agreement with the experimental response up to the peak load, whereas differences were observed in the descending branch due to the presence of a snap-back in the analytical response.

5.4 Recommendations for future studies

FRP and FRCM have been increasingly used for the renovation and strengthening of the deteriorated structures. Nonetheless, limited information is available on their long-term performance and especially in the case of FRCM. The results presented in this thesis are part of ongoing research aiming to provide more information about the durability of these techniques. Several open issues were identified by the author. For instance, more studies are advised to evaluate the effect of the hygrothermal environment on the mechanical properties of PBO textiles. Furthermore, some studies have reported that the durability of the lime-based matrix could be influenced by its porosity, yet this finding needs to be

supported with studies correlating the physical nature of the FRCM matrix and its durability in different environments. More studies evaluating bond durability of the FRCM-substrate interface under the synergic effect of sustain loading and environmental conditioning are also advised. Finally, studies on the effect of freeze-thaw, alkaline environments, sulfate attacks, and other exposures are needed to gain a clear and reliable understanding of the long-term behavior of externally bonded FRCM and SRG composites.

References

Abanilla, M. A., Karbhari, V. M., & Li, Y. (2006). Interlaminar and intralaminar durability characterization of wet layup carbon/epoxy used in external strengthening. *Composites Part B: Engineering*, *37*(7–8), 650–661. https://doi.org/10.1016/j.compositesb.2006.02.023

Abanilla, M. A., Li, Y., & Karbhari, V. M. (2005). Durability characterization of wet layup graphite/epoxy composites used in external strengthening. *Composites Part B: Engineering*, *37*(2–3), 200–212. https://doi.org/10.1016/j.compositesb.2005.05.016

Abaqus Documentation. (2018). Retrieved March 23, 2021, from http://130.149.89.49:2080/v6.14/

Abid, S. R., & Al-lami, K. (2018). Critical review of strength and durability of concrete beams externally bonded with FRP. *Cogent Engineering*, *5*(1). https://doi.org/10.1080/23311916.2018.1525015

ACI Committee 440.2R-8. (2008). Guide for the design and construction of externally bonded FRP systems for strengthening existing structures. *Technical Documents*, 144.

Adamson, M. J. (1980). Thermal expansion and swelling of cured epoxy resin used in graphite/epoxy composite materials. *Journal of Materials Science*, *15*(7), 1736–1745. https://doi.org/10.1007/BF00550593

Al-Khafaji, H. L. (2016). Experimental Investigation of CFRP Wrapped Square Non-ductile Reinforced Concrete Columns.

Al-Lami, K., D'Antino, T., & Colombi, P. (2020). Durability of fabric-reinforced cementitious matrix (FRCM) composites: A review. *Applied Sciences (Switzerland)*, *10*(5). https://doi.org/10.3390/app10051714

Al-Tamimi, A. K., Hawileh, R. A., Abdalla, J. A., Rasheed, H. A., Al-Mahaidi, R., Asce, M., … Asce, M. (2015). Durability of the bond between CFRP plates and concrete exposed to harsh environments. *Journal of Materials in Civil Engineering*, *27*(9), 1–11. https://doi.org/10.1061/(ASCE)MT.1943-5533.0001226

Ali-ahmad, M., Subramaniam, K., & Ghosn, M. (2006). Experimental Investigation and Fracture Analysis of Debonding between Concrete and FRP Sheets, *132*(September), 914–923.

American Concrete Institute. (2017). *Guide for the design and construction of externally bonded FRP systems for strengthening concrete structures*. *Aci 440.2R-17*.

Arboleda, D. (2014). Fabric Reinforced Cementitious Matrix (FRCM) Composites for Infrastructure Strengthening and Rehabilitation : Characterization Methods. *PhD Thesis*, 1–131.

Arruda, M. R. T., Firmo, J. P., Correia, J. R., & Tiago, C. (2016). Numerical modelling of the bond between concrete and CFRP laminates at elevated temperatures. *Engineering Structures*, *110*, 233–243. https://doi.org/10.1016/j.engstruct.2015.11.036

ASTM C666. (2015). Resistance of concrete to freeze and thaw. *ASTM Standards*, 1–7. https://doi.org/10.1520/C0666

ASTM D4541 – 09. (2009). *Standard Test Method for Pull-Off Strength of Coatings Using Portable Adhesion*.

ASTM D638-03. (2004). Standard Test Method for Tensile Properties of Plastics 1, *12*(2), 1–8. Retrieved from https://doi.org/10.1520/D0638-03

Au, C. (2005). Moisture degradation in FRP bonded concrete systems: An interface fracture approach. Massachusetts Institute of Technology.

Au, C., & Büyüköztürk, O. (2006). Debonding of FRP plated concrete: A tri-layer fracture treatment. *Engineering Fracture Mechanics*, *73*(3), 348–365. https://doi.org/10.1016/j.engfracmech.2005.07.007

Au, C., Büyüköztürk, O., Asce, A. M., Büyüköztürk, O., & Asce, M. (2006). Peel and Shear Fracture Characterization of Debonding in FRP Plated Concrete Affected by Moisture. *Journal of Composites for Construction*, *10*(1), 35–47. https://doi.org/10.1061/(ASCE)1090-0268(2006)10:1(35)

Bakis, C. E., Bank, L. C., Brown, V. L., Cosenza, E., Davalos, J. F., Lesko, J. J., …

Triantafillou, T. C. (2003). Fiber-Reinforced Polymer Composites for Construction - State-of-the-Art Review. *Perspectives in Civil Engineering: Commemorating the 150th Anniversary of the American Society of Civil Engineers*, *6*(May), 369–383. https://doi.org/10.1061/(asce)1090-0268(2002)6:2(73)

Bencardino, F., Condello, A., & Ashour, A. F. (2017). Single-lap shear bond tests on Steel Reinforced Geopolymeric Matrix-concrete joints. *Composites Part B: Engineering*, *110*, 62–71. https://doi.org/10.1016/j.compositesb.2016.11.005

Benvenuti, E., Orlando, N., Ferretti, D., & Tralli, A. (2016). A new 3D experimentally consistent XFEM to simulate delamination in FRP-reinforced concrete. *Composites Part B: Engineering*, *91*, 346–360. https://doi.org/10.1016/j.compositesb.2016.01.024

Benzarti, K., Chataigner, S., Quiertant, M., Marty, C., & Aubagnac, C. (2011). Accelerated ageing behaviour of the adhesive bond between concrete specimens and CFRP overlays. *Construction and Building Materials*, *25*(2), 523–538. https://doi.org/10.1016/j.conbuildmat.2010.08.003

Benzarti, K., Freddi, F., & Frémond, M. (2011). A damage model to predict the durability of bonded assemblies. Part I: Debonding behavior of FRP strengthened concrete structures. *Construction and Building Materials*, *25*(2), 547–555. https://doi.org/10.1016/j.conbuildmat.2009.10.018

Blackburn, B. P., Tatar, J., Douglas, E. P., & Hamilton, H. R. (2015). Effects of hygrothermal conditioning on epoxy adhesives used in FRP composites. *Construction and Building Materials*, *96*, 679–689. https://doi.org/10.1016/j.conbuildmat.2015.08.056

Blontrock, H. (2003). *Analysis and modeling of the fire resistance of concrete elements with externally bonded FRP reinforcement*. Ghent University.

BS EN 12467, E. S. (2004). Fibre-cement flat sheets — Product specification and test methods. *Shock*. Brussels, Belgium.

BS EN 2561. (1995). 2561,". *Aerospace Series-Carbon Fibre Reinforced Plastics-Unidirectional Laminates-Tensile Test Parallel to the Fibre Direction," European*

Committee for Standardization, Brussels, Belgium.

Butler, M., Mechtcherine, V., & Hempel, S. (2009). Experimental investigations on the durability of fibre-matrix interfaces in textile-reinforced concrete. *Cement and Concrete Composites*, *31*(4), 221–231. https://doi.org/10.1016/j.cemconcomp.2009.02.005

Butler, M., Mechtcherine, V., & Hempel, S. (2010). Durability of textile reinforced concrete made with AR glass fibre: Effect of the matrix composition. *Materials and Structures/Materiaux et Constructions*, *43*(10), 1351–1368. https://doi.org/10.1617/s11527-010-9586-8

Cabral-fonseca, S., Correia, J. R., Custódio, J., Silva, H. M., Machado, A. M., & Sousa, J. (2018). Durability of FRP - concrete bonded joints in structural rehabilitation: A review. *International Journal of Adhesion and Adhesives*, *83*(March), 153–167. https://doi.org/10.1016/j.ijadhadh.2018.02.014

Calabrese, A. S., Colombi, P., & D'Antino, T. (2019). Analytical solution of the bond behavior of FRCM composites using a rigid-softening cohesive material law. *Composites Part B: Engineering*, *174*(May), 107051. https://doi.org/10.1016/j.compositesb.2019.107051

Calabrese, A. S., D'Antino, T., Colombi, P., & Poggi, C. (2020). Study of the influence of interface normal stresses on the bond behavior of FRCM composites using direct shear and modified beam tests. *Construction and Building Materials*, *262*, 120029. https://doi.org/10.1016/j.conbuildmat.2020.120029

Carloni, C., D'Antino, T., Sneed, L. H., & Pellegrino, C. (2015). Role of the matrix layers in the stress-transfer mechanism of FRCM composites bonded to a concrete substrate. *Journal of Engineering Mechanics*, *141*(6), 1–10. https://doi.org/10.1061/(ASCE)EM.1943-7889.0000883

Carloni, Christian, D'Antino, T., Sneed, L. H., & Pellegrino, C. (2018). Three-Dimensional Numerical Modeling of Single-Lap Direct Shear Tests of FRCM-Concrete Joints Using a Cohesive Damaged Contact Approach. *Journal of Composites for Construction*, *22*(1). https://doi.org/10.1061/(ASCE)CC.1943-

5614.0000827

Carloni, Santandrea, M., & Imohamed, I. A. O. (2017). Determination of the interfacial properties of SRP strips bonded to concrete and comparison between single-lap and notched beam tests. *Engineering Fracture Mechanics*, *186*, 80–104. https://doi.org/10.1016/j.engfracmech.2017.09.020

Carrara, P., & Ferretti, D. (2013). A finite-difference model with mixed interface laws for shear tests of FRP plates bonded to concrete. *Composites Part B: Engineering*, *54*(1), 329–342. https://doi.org/10.1016/j.compositesb.2013.05.030

CEB-FIP. (2010). *Model Code 2010*. *fib Model Code for Concrete Structures 2010*. https://doi.org/10.1002/9783433604090.ch6

CEN, E. C. for S. (2011). Methods of test for mortar for masonry. 11: Determination of flexural and compressive strength of hardened mortar. Brussels, Belgium.

Ceroni, F., Bonati, A., Galimberti, V., & Occhiuzzi, A. (2018). Effects of environmental conditioning on the bond behavior of FRP and FRCM systems applied to concrete elements. *Journal of Engineering Mechanics*, *144*(1), 1–15. https://doi.org/10.1061/(ASCE)EM.1943-7889.0001375

Chen, G. M., Teng, J. G., & Chen, J. F. (2010). Finite-Element Modeling of Intermediate Crack Debonding in FRP-Plated RC Beams. *Journal of Composites for Construction*, *15*(3), 339–353. https://doi.org/10.1061/(asce)cc.1943-5614.0000157

Choi, S., Gartner, A. L., Etten, N. Van, Hamilton, H. R., & Douglas, E. P. (2012). Durability of concrete beams externally reinforced with CFRP composites exposed to various environments. *Journal of Composites for Construction*, *16*(1), 10–20. https://doi.org/10.1061/(ASCE)CC.1943-5614

CNR. (2013). Guide for the design and construction of externally bonded FRP systems for strengthening existing structures. *CNR - Advisory Committee on Technical Recommendations for Construction CNR-DT 200 R1/2013*, 154.

Colombo, I. G., Colombo, M., & Di Prisco, M. (2015). Tensile behavior of textile reinforced concrete subjected to freezing-thawing cycles in un-cracked and cracked regimes. *Cement and Concrete Research*, *73*, 169–183.

https://doi.org/10.1016/j.cemconres.2015.03.001

Consiglio Superiore dei Lavori Pubblici. (2018). Linea Guida per la identificazione, la qualificazione ed il controllo di accettazione di compositi fibrorinforzati a matrice inorganica (FRCM) da utilizzarsi per il consolidamento strutturale di costruzioni esistenti, 1–5. https://doi.org/10.1109/ChiCC.2015.7260208

Cromwell, J. R., Harries, K. A., & Shahrooz, B. M. (2011). Environmental durability of externally bonded FRP materials intended for repair of concrete structures. *Construction and Building Materials*, *25*(5), 2528–2539. https://doi.org/10.1016/j.conbuildmat.2010.11.096

CSLLPP. (2015). *Servizio Tecnico Centrale. Linea Guida per la identificazione, la qualificazione ed il controllo di accettazione di compositi fibrorinforzati a matrice polimerica (FRP) da utilizzarsi per il consolidamento strutturale di costruzioni esistenti*. Rome, Italy.

D'Ambrisi, A., Feo, L., & Focacci, F. (2013). Experimental analysis on bond between PBO-FRCM strengthening materials and concrete. *Composites Part B: Engineering*, *44*(1), 524–532. https://doi.org/10.1016/j.compositesb.2012.03.011

D'Antino, T., Carloni, C., Sneed, L. H., & Pellegrino, C. (2014). Matrix-fiber bond behavior in PBO FRCM composites: A fracture mechanics approach. *Engineering Fracture Mechanics*, *117*, 94–111. https://doi.org/10.1016/j.engfracmech.2014.01.011

D'Antino, T., Pisani, M. A., & Poggi, C. (2018). Effect of the environment on the performance of GFRP reinforcing bars. *Composites Part B: Engineering*, *141*, 123–136. https://doi.org/10.1016/j.compositesb.2017.12.037

D'antino, T., Santandrea, M., & Carloni, C. (2020). Advances in Knowledge of the Fracture Properties of Cohesive Materials: Fired-Clay and Tuff Bricks. *Journal of Engineering Mechanics*, *146*(8), 4020079. https://doi.org/10.1061/(ASCE)EM.1943-7889.0001815

D'Antino, Tommaso, Colombi, P., Carloni, C., & Sneed, L. H. (2018). Estimation of a matrix-fiber interface cohesive material law in FRCM-concrete joints. *Composite*

Structures, *193*, 103–112. https://doi.org/10.1016/j.compstruct.2018.03.005

Dai, Jian-guo, Yokota, H., Iwanami, M., & Kato, E. (2010). Experimental Investigation of the Influence of Moisture on the Bond Behavior of FRP to Concrete Interfaces, *14*(December), 834–844.

Dai, Jianguo, Ueda, T., & Sato, Y. (2005). Development of the Nonlinear Bond Stress – Slip Model of Fiber Reinforced Plastics Sheet – Concrete Interfaces with a Simple Method, *9*(February), 52–62.

Dai, Jianguo, Ueda, T., & Sato, Y. (2006). Unified analytical approaches for determining shear bond characteristics of FRP-concrete interfaces through pullout tests. *Journal of Advanced Concrete Technology*, *4*(1), 133–145. https://doi.org/10.3151/jact.4.133

de Felice, G., D'Antino, T., De Santis, S., Meriggi, P., & Roscini, F. (2020). Lessons Learned on the Tensile and Bond Behavior of Fabric Reinforced Cementitious Matrix (FRCM) Composites. *Frontiers in Built Environment*, *6*(February), 1–15. https://doi.org/10.3389/fbuil.2020.00005

De Munck, M., El Kadi, M., Tsangouri, E., Vervloet, J., Verbruggen, S., Wastiels, J., … Remy, O. (2018). Influence of environmental loading on the tensile and cracking behaviour of textile reinforced cementitious composites. *Construction and Building Materials*, *181*, 325–334. https://doi.org/10.1016/j.conbuildmat.2018.06.045

Djouani, F., Connan, C., Delamar, M., Chehimi, M. M., & Benzarti, K. (2011). Cement paste-epoxy adhesive interactions. *Construction and Building Materials*, *25*(2), 411–423. https://doi.org/10.1016/j.conbuildmat.2010.02.035

Donnini, J. (2019). Durability of glass FRCM systems: Effects of different environments on mechanical properties. *Composites Part B: Engineering*, *174*. https://doi.org/10.1016/j.compositesb.2019.107047

Elarbi, A. M. (2011). *Durability performance of frp strenghtened concrete beams and columns exposed to hygrothermal environment*. Wayne State University. Retrieved from http://digitalcommons.wayne.edu/do/search/?q=Durability performance of frp strenghtened concrete beams and columns exposed to hygrothermal environment&start=0&context=1397974&facet=

EN 1015-11. (2019). BSI Standards Publication Methods of test for mortar for masonry.

EN, B. S. (2009). Testing hardened concrete–Part 3: compressive strength of test specimens. *British Standard Institution, London, England*.

EN, B. S. (2012). 12390-1: Testing hardened concrete Shape, dimensions and other requirements for specimens and moulds. *British Standards Institute, London*.

FASSA BORTOLO. (2019). MS 20, Malta cementizia fibrorinforzata per muratura ed intonaco, per interni ed esterni. *Technical Document*, 2–3. https://doi.org/https://www.fassabortolo.it/it/prodotti/-/p/6/56/prodotti-tradizionali/ms-20-malta-cementizia-per-muratura-ed-intonaco-da-utilizzare-a-mano-per-interni-ed-esterni

Fayala, I., Dhouibi, L., Nóvoa, X. R., & Ben Ouezdou, M. (2013). Effect of inhibitors on the corrosion of galvanized steel and on mortar properties. *Cement and Concrete Composites*, *35*(1), 181–189. https://doi.org/10.1016/j.cemconcomp.2012.08.014

Ferrier, E., Rabinovitch, O., & Michel, L. (2015). Mechanical behavior of concrete-resin/adhesive-FRP structural assemblies under low and high temperatures. *Construction and Building Materials*, *127*, 1017–1028. https://doi.org/10.1016/j.conbuildmat.2015.12.127

Ferrier, E., Rabinovitch, O., & Michel, L. (2016). Mechanical behavior of concrete – resin / adhesive – FRP structural assemblies under low and high temperatures, *127*, 1017–1028. https://doi.org/10.1016/j.conbuildmat.2015.12.127

Firmo, J. P., Correia, J. R., Pitta, D., Tiago, C., & Arruda, M. R. T. (2015). Experimental characterization of the bond between externally bonded reinforcement (EBR) CFRP strips and concrete at elevated temperatures. *Cement and Concrete Composites*, *60*, 44–54. https://doi.org/10.1016/j.cemconcomp.2015.02.008

Firmo, J P, Correia, J. R., Pitta, D., Tiago, C., & Arruda, M. R. T. (2015). Cement & Concrete Composites Experimental characterization of the bond between externally bonded reinforcement (EBR) CFRP strips and concrete at elevated temperatures, *60*, 44–54. https://doi.org/10.1016/j.cemconcomp.2015.02.008

Firmo, João P., Correia, J. R., & Bisby, L. A. (2015). Fire behaviour of FRP-strengthened

reinforced concrete structural elements: A state-of-the-art review. *Composites Part B: Engineering*, *80*, 198–216. https://doi.org/10.1016/j.compositesb.2015.05.045

Focacci, F., & Carloni, C. (2015). Periodic variation of the transferable load at the FRP-masonry interface. *Composite Structures*, *129*, 90–100. https://doi.org/10.1016/j.compstruct.2015.03.008

Franzoni, E., Gentilini, C., Santandrea, M., & Carloni, C. (2018). Effects of rising damp and salt crystallization cycles in FRCM-masonry interfacial debonding: Towards an accelerated laboratory test method. *Construction and Building Materials*, *175*, 225–238. https://doi.org/10.1016/j.conbuildmat.2018.04.164

Franzoni, E., Gentilini, C., Santandrea, M., Zanotto, S., & Carloni, C. (2017). Durability of steel FRCM-masonry joints: effect of water and salt crystallization. *Materials and Structures/Materiaux et Constructions*, *50*(4). https://doi.org/10.1617/s11527-017-1070-2

Frigione, M., Aiello, M. A., & Naddeo, C. (2006). Water effects on the bond strength of concrete/concrete adhesive joints. *Construction and Building Materials*, *20*(10), 957–970. https://doi.org/https://doi.org/10.1016/j.conbuildmat.2005.06.015

Goglio, L., & Rezaei, M. (2014). Variations in mechanical properties of an epoxy adhesive on exposure to warm moisture. *Journal of Adhesion Science and Technology*, *28*(14–15), 1394–1404. https://doi.org/10.1080/01694243.2012.697392

Grave, C., Mcewan, I., & Pethrick, R. A. (1998). Influence of stoichiometric ratio on water absorption in epoxy resins. *Journal of Applied Polymer Science*, *69*(12), 2369–2376. https://doi.org/10.1002/(SICI)1097-4628(19980919)69:12<2369::AID-APP8>3.0.CO;2-6

Hawileh, R. A., Abu-Obeidah, A., Abdalla, J. A., & Al-Tamimi, A. (2015). Temperature effect on the mechanical properties of carbon, glass and carbon-glass FRP laminates. *Construction and Building Materials*, *75*, 342–348. https://doi.org/10.1016/j.conbuildmat.2014.11.020

Helbling, C., Abanilla, M., Lee, L., & Karbhari, V. M. (2006). Issues of variability and durability under synergistic exposure conditions related to advanced polymer

composites in the civil infrastructure. *Composites Part A: Applied Science and Manufacturing*, *37*(8), 1102–1110. https://doi.org/10.1016/j.compositesa.2005.05.039

Hristozov, D., Wroblewski, L., & Sadeghian, P. (2016). Long-term tensile properties of natural fibre-reinforced polymer composites: Comparison of flax and glass fibres. *Composites Part B: Engineering*, *95*, 82–95. https://doi.org/10.1016/j.compositesb.2016.03.079

International Code Council (ICC). (2014). *Acceptance criteria for concrete and reinforced and unreinforced masonry strengthening using externally bonded FRP composite systems, in: ICC AC125, ICC Evaluation Service, .* Whittier, CA.

International Standard Organaziation ISO, & 527-1. (2012). *Plastics Determination of tensile properties – Part 1: General principles*. Geneva, Switzerland.

ISO 10406-1. (n.d.). ISO10406-1,Fibre-reinforcedpolymer(FRP)reinforcement of concrete – Test Methods, Part 1:FRPbarsandgrids,InternationalOrganizationfor Standar-dization, Switzerland,2008. - Google Search. Retrieved November 6, 2019, from https://www.google.com/search?rlz=1C1CHBF_enIT790IT790&sxsrf=ACYBGNQakLVMuOq-PqPUjbKK-rD5JnLDOA:1573058264301&q=ISO10406-1,Fibre-reinforcedpolymer(FRP)reinforcement+of+concrete+–+Test+Methods,+Part+1:FRPbarsandgrids,InternationalOrganizationfor+Standar-+d

Kabir, M. I., Ph, D., Samali, B., Ph, D., Shrestha, R., & Ph, D. (2016). Fracture Properties of CFRP – Concrete Bond Subjected to Three Environmental Conditions, *20*(4), 1–15. https://doi.org/10.1061/(ASCE)CC.1943-5614.0000665.

Kabir, M. I., Shrestha, R., Samali, B., Ikramul, M., Shrestha, R., & Samali, B. (2016). Effects of applied environmental conditions on the pull-out strengths of CFRP-concrete bond. *Construction and Building Materials*, *114*, 817–830. https://doi.org/10.1016/j.conbuildmat.2016.03.195

Kabir, M., Samali, B., & Shrestha, R. (2016). Fracture Properties of CFRP–Concrete Bond Subjected to Three Environmental Conditions. *Journal of Composites for Construction*, *20*(4), 4016010. https://doi.org/10.1061/(ASCE)CC.1943-5614.0000665

Kafodya, I., Xian, G., & Li, H. (2015). Durability study of pultruded CFRP plates immersed in water and seawater under sustained bending: Water uptake and effects on the mechanical properties. *Composites Part B: Engineering*, *70*, 138–148. https://doi.org/10.1016/j.compositesb.2014.10.034

Karbhari, V. M., Chin, J. W., Hunston, D., Benmokrane, B., Juska, T., Morgan, R., … Reynaud, D. (2003). Durability Gap Analysis for Fiber-Reinforced Polymer Composites in Civil Infrastructure. *Journal of Composites for Construction*, *7*(3), 238–247. https://doi.org/10.1061/(ASCE)1090-0268(2003)7:3(238)

Karbhari, V. M., Rivera, J., & Zhang, J. (2002). Low-temperature hygrothermal degradation of ambient cured E-glass/vinylester composites. *Journal of Applied Polymer Science*, *86*(9), 2255–2260. https://doi.org/10.1002/app.11205

Kong, J. S., & Frangopol, D. M. (2003). Life-Cycle Reliability-Based Maintenance Cost Optimization of Deteriorating Structures with Emphasis on Bridges. *Journal of Structural Engineering*, *129*(6), 818–828. https://doi.org/10.1061/(asce)0733-9445(2003)129:6(818)

Kouris, L. A. S., & Triantafillou, T. C. (2018). State-of-the-art on strengthening of masonry structures with textile reinforced mortar (TRM). *Construction and Building Materials*, *188*, 1221–1233. https://doi.org/10.1016/j.conbuildmat.2018.08.039

Koutas, L. N., Tetta, Z., Bournas, D. A., & Triantafillou, T. C. (2019). Strengthening of Concrete Structures with Textile Reinforced Mortars: State-of-the-Art Review. *Journal of Composites for Construction*, *23*(1), 1–20. https://doi.org/10.1061/(ASCE)CC.1943-5614.0000882

Lai, W. L., Kou, S. C., Poon, C. S., Tsang, W. F., & Lai, C. C. (2009). Effects of elevated water temperatures on interfacial delaminations, failure modes and shear strength in externally-bonded CFRP-concrete beams using infrared thermography, gray-scale images and direct shear test. *Construction and Building Materials*, *23*(10), 3152–3160. https://doi.org/10.1016/j.conbuildmat.2009.06.012

Leone, M., Matthys, S., & Aiello, M. A. (2009). Effect of elevated service temperature on bond between FRP EBR systems and concrete. *Composites Part B: Engineering*,

40(1), 85–93. https://doi.org/10.1016/j.compositesb.2008.06.004

Lettieri, M., & Frigione, M. (2012). Effects of humid environment on thermal and mechanical properties of a cold-curing structural epoxy adhesive. *Construction and Building Materials*, *30*, 753–760. https://doi.org/10.1016/j.conbuildmat.2011.12.077

Lin, Y. C., & Chen, X. (2005). Moisture sorption-desorption-resorption characteristics and its effect on the mechanical behavior of the epoxy system. *Polymer*, *46*(25), 11994–12003. https://doi.org/10.1016/j.polymer.2005.10.002

Lomboy, G., International, K. W.-J. of A., & 2009, undefined. (n.d.). Effects of strength, permeability, and air void parameters on freezing-thawing resistance of concrete with and without air entrainment. *Astm.Org*. Retrieved from http://www.astm.org/DIGITAL_LIBRARY/JOURNALS/JAI/PAGES/JAI102454.htm

Lopez de Murphy, M. del M., & Krishnawamy, R. (2006). *Time Performance of Concrete-CFRP Bond Under Effects of Freeze-Thaw Cycles and Sustained Loading*.

Luque, A., Ruiz-Agudo, E., Cultrone, G., Sebastián, E., & Siegesmund, S. (2011). Direct observation of microcrack development in marble caused by thermal weathering. *Environmental Earth Sciences*, *62*(7), 1375–1386. https://doi.org/10.1007/s12665-010-0624-1

Maljaee, H., Ghiassi, B., & Lourenço, P. B. (2017). Effect of synergistic environmental conditions on thermal properties of a cold curing epoxy resin. *Composites Part B: Engineering*, *113*, 152–163. https://doi.org/10.1016/j.compositesb.2017.01.027

Maljaee, H., Ghiassi, B., Lourenço, P. B., & Oliveira, D. V. (2016). FRP-brick masonry bond degradation under hygrothermal conditions. *Composite Structures*, *147*, 143–154. https://doi.org/10.1016/j.compstruct.2016.03.037

Maxwell, I. D., & Pethrick, R. A. (1983). Dielectric studies of water in epoxy resins. *Journal of Applied Polymer Science*, *28*(7), 2363–2379. https://doi.org/10.1002/app.1983.070280719

Micelli, F., Mazzotta, R., Leone, M., & Aiello, M. A. (2015). Review Study on the Durability of FRP-Confined Concrete. *Journal of Composites for Construction*,

19(3), 04014056. https://doi.org/10.1061/(ASCE)CC.1943-5614.0000520

Mikami, C., Wu, H. C., & Elarbi, A. (2015). Effect of hot temperature on pull-off strength of FRP bonded concrete. *Construction and Building Materials*, *91*, 180–186. https://doi.org/10.1016/j.conbuildmat.2015.05.013

Nishizaki, I., & Kato, Y. (2011). Durability of the adhesive bond between continuous fibre sheet reinforcements and concrete in an outdoor environment. *Construction and Building Materials*, *25*(2), 515–522. https://doi.org/10.1016/j.conbuildmat.2010.04.067

Nobili, A. (2016). Durability assessment of impregnated Glass Fabric Reinforced Cementitious Matrix (GFRCM) composites in the alkaline and saline environments. *Construction and Building Materials*, *105*, 465–471. https://doi.org/10.1016/j.conbuildmat.2015.12.173

Pekmezci, B. Y., Arabaci, E., & Ustundag, C. (2019). Freeze-Thaw Durability of Lime Based FRCM Systems for Strengthening Historical Masonry. *Key Engineering Materials*, *817*, 174–181. https://doi.org/10.4028/www.scientific.net/kem.817.174

Pendhari, S. S., Kant, T., & Desai, Y. M. (2008). Application of polymer composites in civil construction: A general review. *Composite Structures*, *84*(2), 114–124. https://doi.org/10.1016/J.COMPSTRUCT.2007.06.007

Ramirez, F. A., Carlsson, L. A., & Acha, B. A. (2008). Evaluation of water degradation of vinylester and epoxy matrix composites by single fiber and composite tests. *Journal of Materials Science*, *43*(15), 5230–5242. https://doi.org/10.1007/s10853-008-2766-z

Robert, M., Wang, P., Cousin, P., & Benmokrane, B. (2010). Temperature as an Accelerating Factor forLong-Term Durability Testing of FRPs:\nShould There Be Any Limitations? *Journal of Composites for Construction*, *14*(4), 361–367. https://doi.org/10.1061//asce/cc.1943-5614.0000102

Roventi, G., Bellezze, T., Giuliani, G., & Conti, C. (2014). Corrosion resistance of galvanized steel reinforcements in carbonated concrete: Effect of wet-dry cycles in tap water and in chloride solution on the passivating layer. *Cement and Concrete Research*, *65*, 76–84. https://doi.org/10.1016/j.cemconres.2014.07.014

Ruregold. (2019a). C-MESH GOLD 84 / 84. *Technical Document*, 1–6. Retrieved from https://www.ruregold.com/

Ruregold. (2019b). PBO-Mesh Gold 70/18 & PBO-MX GOLD MURATURA. *Technical Document*. Retrieved from https://www.ruregold.com/

Saadatmanesh, H., Tavakkolizadeh, M., & Mostofinejad, D. (2010). Environmental effects on mechanical properties of wet lay-up fiber-reinforced polymer. *ACI Materials Journal*, *107*(3), 267.

Santandrea, M., Focacci, F., Mazzotti, C., Ubertini, F., & Carloni, C. (2020). Determination of the interfacial cohesive material law for SRG composites bonded to a masonry substrate. *Engineering Failure Analysis*, *111*, 104322. https://doi.org/10.1016/j.engfailanal.2019.104322

Savvilotidou, M., Vassilopoulos, A. P., Frigione, M., & Keller, T. (2017). Effects of aging in dry environment on physical and mechanical properties of a cold-curing structural epoxy adhesive for bridge construction. *Construction and Building Materials*, *140*, 552–561. https://doi.org/10.1016/j.conbuildmat.2017.02.063

Scheffler, C., Förster, T., Mäder, E., Heinrich, G., Hempel, S., & Mechtcherine, V. (2009). Aging of alkali-resistant glass and basalt fibers in alkaline solutions: Evaluation of the failure stress by Weibull distribution function. *Journal of Non-Crystalline Solids*, *355*(52–54), 2588–2595. https://doi.org/10.1016/j.jnoncrysol.2009.09.018

Sen, R. (2015). Developments in the durability of FRP-concrete bond. *Construction and Building Materials*, *78*, 112–125. https://doi.org/10.1016/j.conbuildmat.2014.12.106

Serbescu, A., Guadagnini, M., & Pilakoutas, K. (2013). Standardised double-shear test for determining bond of FRP to concrete and corresponding model development. *Composites Part B: Engineering*, *55*, 277–297. https://doi.org/10.1016/j.compositesb.2013.06.019

Sethi, S., & Ray, B. C. (2015). Environmental effects on fibre reinforced polymeric composites: Evolving reasons and remarks on interfacial strength and stability. *Advances in Colloid and Interface Science*, *217*, 43–67. https://doi.org/10.1016/j.cis.2014.12.005

Shrestha, J., Ueda, T., & Zhang, D. (2015). Durability of FRP Concrete Bonds and Its Constituent Properties under the Influence of Moisture Conditions. *Journal of Materials in Civil Engineering*, *27*(2), A4014009. https://doi.org/10.1061/(asce)mt.1943-5533.0001093

Sika. (2017a). Sikadur®-330. *Technical Document*, 2–5. Retrieved from https://ita.sika.com/it/edilizia/rinforzi-e-incollaggistrutturali/strutture-in-calcestruzzo/incollaggio-strutturaleeiniezioni/sikadur-330.html

Sika. (2017b). SikaWrap ® -300 C. *Technical Document*, 1–4. Retrieved from https://ita.sika.com/it/edilizia/rinforzi-e-incollaggistrutturali/strutture-in-calcestruzzo/tessuti-in-carbonio/sikawrap-300-c.html

Sika. (2019). Sika MonoTop ® -722 Mur. *Technical Document*, 1–4. Retrieved from https://ita.sika.com/it/edilizia/rinforzi-e-incollaggistrutturali/sistemi-antisfondellamentopersolai/sika-monotop-722mur.html

Silva, M. A. G., & Biscaia, H. (2008). Degradation of bond between FRP and RC beams. *Composite Structures*, *85*(2), 164–174. https://doi.org/10.1016/j.compstruct.2007.10.014

Silva, P., Fernandes, P., Sena-Cruz, J., Xavier, J., Castro, F., Soares, D., & Carneiro, V. (2016). Effects of different environmental conditions on the mechanical characteristics of a structural epoxy. *Composites Part B: Engineering*, *88*, 55–63. https://doi.org/10.1016/j.compositesb.2015.10.036

Sneed, L. H., D'Antino, T., & Carloni, C. (2014). Investigation of bond behavior of polyparaphenylene benzobisoxazole fiber-reinforced cementitious matrix composite-concrete interface. *ACI Materials Journal*, *111*(5), 569–580. https://doi.org/10.14359/51686604

Soles, C. L., & Yee, A. F. (2000). Discussion of the molecular mechanisms of moisture transport in epoxy resins. *Journal of Polymer Science, Part B: Polymer Physics*, *38*(5), 792–802. https://doi.org/10.1002/(SICI)1099-0488(20000301)38:5<792::AID-POLB16>3.0.CO;2-H

Stefania, S. M., Mariaenrica, F., & Antonietta, A. M. (2010). Wet Lay-Up Manufactured

FRPs for Concrete and Masonry Repair: Influence of Water on the Properties of Composites and on Their Epoxy Components. *Journal of Composites for Construction*, *14*(6), 823–833. https://doi.org/10.1061/(ASCE)CC.1943-5614.0000132

Sun, W., Zhang, Y. M., Yan, H. D., & Mu, R. (1999). Damage and damage resistance of high strength concrete under the action of load and freeze-thaw cycles. *Cement and Concrete Research*, *29*(9), 1519–1523. https://doi.org/10.1016/S0008-8846(99)00097-6

Täljsten, B., Journal, I., Publishers, K. A., Engineering, S., & Engineering, C. (1996). Strengthening of concrete prisms using the plate-bonding technique. *International Journal of Fracture*, *82*(3), 253–266. https://doi.org/10.1007/BF00013161

Tao, Y., & Chen, J. F. (2014). Concrete Damage Plasticity Model for Modeling FRP-to-Concrete Bond Behavior. *Journal of Composites for Construction*, *19*(1), 04014026. https://doi.org/10.1061/(asce)cc.1943-5614.0000482

Tatar, J, Weston, C., Blackburn, P., & Hamilton, H. R. (2013). Direct Shear Adhesive Bond Test, 1–10.

Tatar, Jovan, & Hamilton, H. R. (2016). Comparison of laboratory and field environmental conditioning on FRP-concrete bond durability. *Construction and Building Materials*, *122*, 525–536. https://doi.org/10.1016/j.conbuildmat.2016.06.074

TCS. (2020a). B-STRUCTURA. *Technical Document*, (January). Retrieved from https://www.tcscalce.it/en/prodotto/b-structura

TCS. (2020b). Steel X800-A4. *Technical Document*, (July), 1–3. Retrieved from https://www.tcscalce.it/en/prodotto/tcs-steel-x800-a4

Teng, J. G., Zhang, S. S., Dai, J. G., & Chen, J. F. (2013). Three-dimensional meso-scale finite element modeling of bonded joints between a near-surface mounted FRP strip and concrete. *Computers and Structures*, *117*, 105–117. https://doi.org/10.1016/j.compstruc.2012.12.002

Terreal Italia San Marco. (2018). Vivo Red Bricks. *Technical Documents*. Retrieved from https://www.sanmarco.it/scheda-prodotto.php?id-categoria=2&id-prodotto=36

Tuakta, C., & Büyüköztürk, O. (2011). Deterioration of FRP/concrete bond system under variable moisture conditions quantified by fracture mechanics. *Composites Part B: Engineering*, *42*(2), 145–154. https://doi.org/10.1016/j.compositesb.2010.11.002

Uomoto, T., Mutsuyoshi, H., Katsuki, F., & Misra, S. (2002). Use of fiber reinforced polymer composites as reinforcing material for concrete. *Journal of Materials in Civil Engineering*, *14*(3), 191–209. https://doi.org/10.1061/(ASCE)0899-1561(2002)14:3(191)

VanLandingham, M. R., Eduljee, R. F., & Gillespie, J. W. (1999). Moisture Diffusion in Epoxy Systems. *Journal of Applied Polymer Science*, *71*(5), 787–798. https://doi.org/10.1002/(SICI)1097-4628(19990131)71:5<787::AID-APP12>3.0.CO;2-A

Williams Portal, N., Flansbjer, M., Johannesson, P., Malaga, K., & Lundgren, K. (2016). Tensile behaviour of textile reinforcement under accelerated ageing conditions. *Journal of Building Engineering*, *5*, 57–66. https://doi.org/10.1016/j.jobe.2015.11.006

Woo, M. S. W., & Piggott, M. R. (1987). WATER ABSORPTION OF RESINS AND COMPOSITES: II. DIFFUSION IN CARBON AND GLASS REINFORCED EPOXIES. *Journal of Composites Technology and Research*, *9*(4), 162–166.

Wu, Z., Yuan, H., Niu, H., Zhishen, W., Hong, Y., & Hedong, N. (2002). Stress transfer and fracture propagation in different kinds of adhesive joints. *Journal of Engineering Mechanics*, *128*(5), 562–573. https://doi.org/10.1061/(ASCE)0733-9399(2002)128:5(562)

Yadav, A. P., Nishikata, A., & Tsuru, T. (2004). Degradation mechanism of galvanized steel in wet-dry cyclic environment containing chloride ions. *Corrosion Science*, *46*(2), 361–376. https://doi.org/10.1016/S0010-938X(03)00153-7

Yalim, B., Kalayci, A. S., & Mirmiran, A. (2008). Performance of FRP-strengthened RC beams with different concrete surface profiles. *Journal of Composites for Construction*, *12*(6), 626–634. https://doi.org/10.1061/(ASCE)1090-0268(2008)12:6(626)

Yang, Q., Xian, G., & Karbhari, V. M. (2008). Hygrothermal ageing of an epoxy adhesive used in FRP strengthening of concrete. *Journal of Applied Polymer Science*, *107*(4), 2607–2617. https://doi.org/10.1002/app.27287

Yin, S., Jing, L., Yin, M., & Wang, B. (2019). Mechanical properties of textile reinforced concrete under chloride wet-dry and freeze-thaw cycle environments. *Cement and Concrete Composites*, *96*(November 2018), 118–127. https://doi.org/10.1016/j.cemconcomp.2018.11.020

Yuan, H., Teng, J. G., Seracino, R., Wu, Z. S., & Yao, J. (2004). Full-range behavior of FRP-to-concrete bonded joints. *Engineering Structures*, *26*(5), 553–565. https://doi.org/10.1016/j.engstruct.2003.11.006

Zhou, A., Büyüköztürk, O., & Lau, D. (2017). Debonding of concrete-epoxy interface under the coupled effect of moisture and sustained load. *Cement and Concrete Composites*, *80*, 287–297. https://doi.org/10.1016/j.cemconcomp.2017.03.019

Zhou, J., & Lucas, J. P. (1999a). Hygrothermal effects of epoxy resin. Part I: The nature of water in epoxy. *Polymer*, *40*(20), 5505–5512. https://doi.org/10.1016/S0032-3861(98)00790-3

Zhou, J., & Lucas, J. P. (1999b). Hygrothermal effects of epoxy resin. Part II: Variations of glass transition temperature. *Polymer*, *40*(20), 5513–5522. https://doi.org/10.1016/S0032-3861(98)00791-5

Abanilla, M. A., Karbhari, V. M., & Li, Y. (2006). Interlaminar and intralaminar durability characterization of wet layup carbon/epoxy used in external strengthening. *Composites Part B: Engineering*, *37*(7–8), 650–661. https://doi.org/10.1016/j.compositesb.2006.02.023

Abanilla, M. A., Li, Y., & Karbhari, V. M. (2005). Durability characterization of wet layup graphite/epoxy composites used in external strengthening. *Composites Part B: Engineering*, *37*(2–3), 200–212. https://doi.org/10.1016/j.compositesb.2005.05.016

Abaqus Documentation. (2018). Retrieved March 23, 2021, from http://130.149.89.49:2080/v6.14/

Abid, S. R., & Al-lami, K. (2018). Critical review of strength and durability of concrete

beams externally bonded with FRP. *Cogent Engineering*, *5*(1). https://doi.org/10.1080/23311916.2018.1525015

ACI Committee 440.2R-8. (2008). Guide for the design and construction of externally bonded FRP systems for strengthening existing structures. *Technical Documents*, 144.

Adamson, M. J. (1980). Thermal expansion and swelling of cured epoxy resin used in graphite/epoxy composite materials. *Journal of Materials Science*, *15*(7), 1736–1745. https://doi.org/10.1007/BF00550593

Al-Khafaji, H. L. (2016). Experimental Investigation of CFRP Wrapped Square Non-ductile Reinforced Concrete Columns.

Al-Lami, K., D'Antino, T., & Colombi, P. (2020). Durability of fabric-reinforced cementitious matrix (FRCM) composites: A review. *Applied Sciences (Switzerland)*, *10*(5). https://doi.org/10.3390/app10051714

Al-Tamimi, A. K., Hawileh, R. A., Abdalla, J. A., Rasheed, H. A., Al-Mahaidi, R., Asce, M., … Asce, M. (2015). Durability of the bond between CFRP plates and concrete exposed to harsh environments. *Journal of Materials in Civil Engineering*, *27*(9), 1–11. https://doi.org/10.1061/(ASCE)MT.1943-5533.0001226

Ali-ahmad, M., Subramaniam, K., & Ghosn, M. (2006). Experimental Investigation and Fracture Analysis of Debonding between Concrete and FRP Sheets, *132*(September), 914–923.

American Concrete Institute. (2017). *Guide for the design and construction of externally bonded FRP systems for strengthening concrete structures*. *Aci 440.2R-17*.

Arboleda, D. (2014). Fabric Reinforced Cementitious Matrix (FRCM) Composites for Infrastructure Strengthening and Rehabilitation : Characterization Methods. *PhD Thesis*, 1–131.

Arruda, M. R. T., Firmo, J. P., Correia, J. R., & Tiago, C. (2016). Numerical modelling of the bond between concrete and CFRP laminates at elevated temperatures. *Engineering Structures*, *110*, 233–243. https://doi.org/10.1016/j.engstruct.2015.11.036

ASTM C666. (2015). Resistance of concrete to freeze and thaw. *ASTM Standards*, 1–7. https://doi.org/10.1520/C0666

ASTM D4541 – 09. (2009). *Standard Test Method for Pull-Off Strength of Coatings Using Portable Adhesion*.

ASTM D638-03. (2004). Standard Test Method for Tensile Properties of Plastics 1, *12*(2), 1–8. Retrieved from https://doi.org/10.1520/D0638-03

Au, C. (2005). Moisture degradation in FRP bonded concrete systems: An interface fracture approach. Massachusetts Institute of Technology.

Au, C., & Büyüköztürk, O. (2006). Debonding of FRP plated concrete: A tri-layer fracture treatment. *Engineering Fracture Mechanics*, *73*(3), 348–365. https://doi.org/10.1016/j.engfracmech.2005.07.007

Au, C., Büyüköztürk, O., Asce, A. M., Büyüköztürk, O., & Asce, M. (2006). Peel and Shear Fracture Characterization of Debonding in FRP Plated Concrete Affected by Moisture. *Journal of Composites for Construction*, *10*(1), 35–47. https://doi.org/10.1061/(ASCE)1090-0268(2006)10:1(35)

Bakis, C. E., Bank, L. C., Brown, V. L., Cosenza, E., Davalos, J. F., Lesko, J. J., … Triantafillou, T. C. (2003). Fiber-Reinforced Polymer Composites for Construction - State-of-the-Art Review. *Perspectives in Civil Engineering: Commemorating the 150th Anniversary of the American Society of Civil Engineers*, *6*(May), 369–383. https://doi.org/10.1061/(asce)1090-0268(2002)6:2(73)

Bencardino, F., Condello, A., & Ashour, A. F. (2017). Single-lap shear bond tests on Steel Reinforced Geopolymeric Matrix-concrete joints. *Composites Part B: Engineering*, *110*, 62–71. https://doi.org/10.1016/j.compositesb.2016.11.005

Benvenuti, E., Orlando, N., Ferretti, D., & Tralli, A. (2016). A new 3D experimentally consistent XFEM to simulate delamination in FRP-reinforced concrete. *Composites Part B: Engineering*, *91*, 346–360. https://doi.org/10.1016/j.compositesb.2016.01.024

Benzarti, K., Chataigner, S., Quiertant, M., Marty, C., & Aubagnac, C. (2011). Accelerated ageing behaviour of the adhesive bond between concrete specimens and

CFRP overlays. *Construction and Building Materials*, *25*(2), 523–538. https://doi.org/10.1016/j.conbuildmat.2010.08.003

Benzarti, K., Freddi, F., & Frémond, M. (2011). A damage model to predict the durability of bonded assemblies. Part I: Debonding behavior of FRP strengthened concrete structures. *Construction and Building Materials*, *25*(2), 547–555. https://doi.org/10.1016/j.conbuildmat.2009.10.018

Blackburn, B. P., Tatar, J., Douglas, E. P., & Hamilton, H. R. (2015). Effects of hygrothermal conditioning on epoxy adhesives used in FRP composites. *Construction and Building Materials*, *96*, 679–689. https://doi.org/10.1016/j.conbuildmat.2015.08.056

Blontrock, H. (2003). *Analysis and modeling of the fire resistance of concrete elements with externally bonded FRP reinforcement*. Ghent University.

BS EN 12467, E. S. (2004). Fibre-cement flat sheets — Product specification and test methods. *Shock*. Brussels, Belgium.

BS EN 2561. (1995). 2561,". *Aerospace Series-Carbon Fibre Reinforced Plastics-Unidirectional Laminates-Tensile Test Parallel to the Fibre Direction," European Committee for Standardization, Brussels, Belgium*.

Butler, M., Mechtcherine, V., & Hempel, S. (2009). Experimental investigations on the durability of fibre-matrix interfaces in textile-reinforced concrete. *Cement and Concrete Composites*, *31*(4), 221–231. https://doi.org/10.1016/j.cemconcomp.2009.02.005

Butler, M., Mechtcherine, V., & Hempel, S. (2010). Durability of textile reinforced concrete made with AR glass fibre: Effect of the matrix composition. *Materials and Structures/Materiaux et Constructions*, *43*(10), 1351–1368. https://doi.org/10.1617/s11527-010-9586-8

Cabral-fonseca, S., Correia, J. R., Custódio, J., Silva, H. M., Machado, A. M., & Sousa, J. (2018). Durability of FRP - concrete bonded joints in structural rehabilitation: A review. *International Journal of Adhesion and Adhesives*, *83*(March), 153–167. https://doi.org/10.1016/j.ijadhadh.2018.02.014

Calabrese, A. S., Colombi, P., & D'Antino, T. (2019). Analytical solution of the bond behavior of FRCM composites using a rigid-softening cohesive material law. *Composites Part B: Engineering*, *174*(May), 107051. https://doi.org/10.1016/j.compositesb.2019.107051

Calabrese, A. S., D'Antino, T., Colombi, P., & Poggi, C. (2020). Study of the influence of interface normal stresses on the bond behavior of FRCM composites using direct shear and modified beam tests. *Construction and Building Materials*, *262*, 120029. https://doi.org/10.1016/j.conbuildmat.2020.120029

Carloni, C., D'Antino, T., Sneed, L. H., & Pellegrino, C. (2015). Role of the matrix layers in the stress-transfer mechanism of FRCM composites bonded to a concrete substrate. *Journal of Engineering Mechanics*, *141*(6), 1–10. https://doi.org/10.1061/(ASCE)EM.1943-7889.0000883

Carloni, Christian, D'Antino, T., Sneed, L. H., & Pellegrino, C. (2018). Three-Dimensional Numerical Modeling of Single-Lap Direct Shear Tests of FRCM-Concrete Joints Using a Cohesive Damaged Contact Approach. *Journal of Composites for Construction*, *22*(1). https://doi.org/10.1061/(ASCE)CC.1943-5614.0000827

Carloni, Santandrea, M., & Imohamed, I. A. O. (2017). Determination of the interfacial properties of SRP strips bonded to concrete and comparison between single-lap and notched beam tests. *Engineering Fracture Mechanics*, *186*, 80–104. https://doi.org/10.1016/j.engfracmech.2017.09.020

Carrara, P., & Ferretti, D. (2013). A finite-difference model with mixed interface laws for shear tests of FRP plates bonded to concrete. *Composites Part B: Engineering*, *54*(1), 329–342. https://doi.org/10.1016/j.compositesb.2013.05.030

CEB-FIP. (2010). *Model Code 2010*. *fib Model Code for Concrete Structures 2010*. https://doi.org/10.1002/9783433604090.ch6

CEN, E. C. for S. (2011). Methods of test for mortar for masonry. 11: Determination of flexural and compressive strength of hardened mortar. Brussels, Belgium.

Ceroni, F., Bonati, A., Galimberti, V., & Occhiuzzi, A. (2018). Effects of environmental

conditioning on the bond behavior of FRP and FRCM systems applied to concrete elements. *Journal of Engineering Mechanics*, *144*(1), 1–15. https://doi.org/10.1061/(ASCE)EM.1943-7889.0001375

Chen, G. M., Teng, J. G., & Chen, J. F. (2010). Finite-Element Modeling of Intermediate Crack Debonding in FRP-Plated RC Beams. *Journal of Composites for Construction*, *15*(3), 339–353. https://doi.org/10.1061/(asce)cc.1943-5614.0000157

Choi, S., Gartner, A. L., Etten, N. Van, Hamilton, H. R., & Douglas, E. P. (2012). Durability of concrete beams externally reinforced with CFRP composites exposed to various environments. *Journal of Composites for Construction*, *16*(1), 10–20. https://doi.org/10.1061/(ASCE)CC.1943-5614

CNR. (2013). Guide for the design and construction of externally bonded FRP systems for strengthening existing structures. *CNR - Advisory Committee on Technical Recommendations for Construction CNR-DT 200 R1/2013*, 154.

Colombo, I. G., Colombo, M., & Di Prisco, M. (2015). Tensile behavior of textile reinforced concrete subjected to freezing-thawing cycles in un-cracked and cracked regimes. *Cement and Concrete Research*, *73*, 169–183. https://doi.org/10.1016/j.cemconres.2015.03.001

Consiglio Superiore dei Lavori Pubblici. (2018). Linea Guida per la identificazione, la qualificazione ed il controllo di accettazione di compositi fibrorinforzati a matrice inorganica (FRCM) da utilizzarsi per il consolidamento strutturale di costruzioni esistenti, 1–5. https://doi.org/10.1109/ChiCC.2015.7260208

Cromwell, J. R., Harries, K. A., & Shahrooz, B. M. (2011). Environmental durability of externally bonded FRP materials intended for repair of concrete structures. *Construction and Building Materials*, *25*(5), 2528–2539. https://doi.org/10.1016/j.conbuildmat.2010.11.096

CSLLPP. (2015). *Servizio Tecnico Centrale. Linea Guida per la identificazione, la qualificazione ed il controllo di accettazione di compositi fibrorinforzati a matrice polimerica (FRP) da utilizzarsi per il consolidamento strutturale di costruzioni esistenti*. Rome, Italy.

D'Ambrisi, A., Feo, L., & Focacci, F. (2013). Experimental analysis on bond between PBO-FRCM strengthening materials and concrete. *Composites Part B: Engineering*, *44*(1), 524–532. https://doi.org/10.1016/j.compositesb.2012.03.011

D'Antino, T., Carloni, C., Sneed, L. H., & Pellegrino, C. (2014). Matrix-fiber bond behavior in PBO FRCM composites: A fracture mechanics approach. *Engineering Fracture Mechanics*, *117*, 94–111. https://doi.org/10.1016/j.engfracmech.2014.01.011

D'Antino, T., Pisani, M. A., & Poggi, C. (2018). Effect of the environment on the performance of GFRP reinforcing bars. *Composites Part B: Engineering*, *141*, 123–136. https://doi.org/10.1016/j.compositesb.2017.12.037

D'antino, T., Santandrea, M., & Carloni, C. (2020). Advances in Knowledge of the Fracture Properties of Cohesive Materials: Fired-Clay and Tuff Bricks. *Journal of Engineering Mechanics*, *146*(8), 4020079. https://doi.org/10.1061/(ASCE)EM.1943-7889.0001815

D'Antino, Tommaso, Colombi, P., Carloni, C., & Sneed, L. H. (2018). Estimation of a matrix-fiber interface cohesive material law in FRCM-concrete joints. *Composite Structures*, *193*, 103–112. https://doi.org/10.1016/j.compstruct.2018.03.005

Dai, Jian-guo, Yokota, H., Iwanami, M., & Kato, E. (2010). Experimental Investigation of the Influence of Moisture on the Bond Behavior of FRP to Concrete Interfaces, *14*(December), 834–844.

Dai, Jianguo, Ueda, T., & Sato, Y. (2005). Development of the Nonlinear Bond Stress – Slip Model of Fiber Reinforced Plastics Sheet – Concrete Interfaces with a Simple Method, *9*(February), 52–62.

Dai, Jianguo, Ueda, T., & Sato, Y. (2006). Unified analytical approaches for determining shear bond characteristics of FRP-concrete interfaces through pullout tests. *Journal of Advanced Concrete Technology*, *4*(1), 133–145. https://doi.org/10.3151/jact.4.133

de Felice, G., D'Antino, T., De Santis, S., Meriggi, P., & Roscini, F. (2020). Lessons Learned on the Tensile and Bond Behavior of Fabric Reinforced Cementitious Matrix (FRCM) Composites. *Frontiers in Built Environment*, *6*(February), 1–15.

https://doi.org/10.3389/fbuil.2020.00005

De Munck, M., El Kadi, M., Tsangouri, E., Vervloet, J., Verbruggen, S., Wastiels, J., … Remy, O. (2018). Influence of environmental loading on the tensile and cracking behaviour of textile reinforced cementitious composites. *Construction and Building Materials*, *181*, 325–334. https://doi.org/10.1016/j.conbuildmat.2018.06.045

Djouani, F., Connan, C., Delamar, M., Chehimi, M. M., & Benzarti, K. (2011). Cement paste-epoxy adhesive interactions. *Construction and Building Materials*, *25*(2), 411–423. https://doi.org/10.1016/j.conbuildmat.2010.02.035

Donnini, J. (2019). Durability of glass FRCM systems: Effects of different environments on mechanical properties. *Composites Part B: Engineering*, *174*. https://doi.org/10.1016/j.compositesb.2019.107047

Elarbi, A. M. (2011). *Durability performance of frp strenghtened concrete beams and columns exposed to hygrothermal environment*. Wayne State University. Retrieved from http://digitalcommons.wayne.edu/do/search/?q=Durability performance of frp strenghtened concrete beams and columns exposed to hygrothermal environment&start=0&context=1397974&facet=

EN 1015-11. (2019). BSI Standards Publication Methods of test for mortar for masonry.

EN, B. S. (2009). Testing hardened concrete–Part 3: compressive strength of test specimens. *British Standard Institution, London, England*.

EN, B. S. (2012). 12390-1: Testing hardened concrete Shape, dimensions and other requirements for specimens and moulds. *British Standards Institute, London*.

FASSA BORTOLO. (2019). MS 20, Malta cementizia fibrorinforzata per muratura ed intonaco, per interni ed esterni. *Technical Document*, 2–3. https://doi.org/https://www.fassabortolo.it/it/prodotti/-/p/6/56/prodotti-tradizionali/ms-20-malta-cementizia-per-muratura-ed-intonaco-da-utilizzare-a-mano-per-interni-ed-esterni

Fayala, I., Dhouibi, L., Nóvoa, X. R., & Ben Ouezdou, M. (2013). Effect of inhibitors on the corrosion of galvanized steel and on mortar properties. *Cement and Concrete Composites*, *35*(1), 181–189. https://doi.org/10.1016/j.cemconcomp.2012.08.014

Ferrier, E., Rabinovitch, O., & Michel, L. (2015). Mechanical behavior of concrete-resin/adhesive-FRP structural assemblies under low and high temperatures. *Construction and Building Materials*, *127*, 1017–1028. https://doi.org/10.1016/j.conbuildmat.2015.12.127

Ferrier, E., Rabinovitch, O., & Michel, L. (2016). Mechanical behavior of concrete – resin / adhesive – FRP structural assemblies under low and high temperatures, *127*, 1017–1028. https://doi.org/10.1016/j.conbuildmat.2015.12.127

Firmo, J. P., Correia, J. R., Pitta, D., Tiago, C., & Arruda, M. R. T. (2015). Experimental characterization of the bond between externally bonded reinforcement (EBR) CFRP strips and concrete at elevated temperatures. *Cement and Concrete Composites*, *60*, 44–54. https://doi.org/10.1016/j.cemconcomp.2015.02.008

Firmo, J P, Correia, J. R., Pitta, D., Tiago, C., & Arruda, M. R. T. (2015). Cement & Concrete Composites Experimental characterization of the bond between externally bonded reinforcement (EBR) CFRP strips and concrete at elevated temperatures, *60*, 44–54. https://doi.org/10.1016/j.cemconcomp.2015.02.008

Firmo, João P., Correia, J. R., & Bisby, L. A. (2015). Fire behaviour of FRP-strengthened reinforced concrete structural elements: A state-of-the-art review. *Composites Part B: Engineering*, *80*, 198–216. https://doi.org/10.1016/j.compositesb.2015.05.045

Focacci, F., & Carloni, C. (2015). Periodic variation of the transferable load at the FRP-masonry interface. *Composite Structures*, *129*, 90–100. https://doi.org/10.1016/j.compstruct.2015.03.008

Franzoni, E., Gentilini, C., Santandrea, M., & Carloni, C. (2018). Effects of rising damp and salt crystallization cycles in FRCM-masonry interfacial debonding: Towards an accelerated laboratory test method. *Construction and Building Materials*, *175*, 225–238. https://doi.org/10.1016/j.conbuildmat.2018.04.164

Franzoni, E., Gentilini, C., Santandrea, M., Zanotto, S., & Carloni, C. (2017). Durability of steel FRCM-masonry joints: effect of water and salt crystallization. *Materials and Structures/Materiaux et Constructions*, *50*(4). https://doi.org/10.1617/s11527-017-1070-2

Frigione, M., Aiello, M. A., & Naddeo, C. (2006). Water effects on the bond strength of concrete/concrete adhesive joints. *Construction and Building Materials*, *20*(10), 957–970. https://doi.org/https://doi.org/10.1016/j.conbuildmat.2005.06.015

Goglio, L., & Rezaei, M. (2014). Variations in mechanical properties of an epoxy adhesive on exposure to warm moisture. *Journal of Adhesion Science and Technology*, *28*(14–15), 1394–1404. https://doi.org/10.1080/01694243.2012.697392

Grave, C., Mcewan, I., & Pethrick, R. A. (1998). Influence of stoichiometric ratio on water absorption in epoxy resins. *Journal of Applied Polymer Science*, *69*(12), 2369–2376. https://doi.org/10.1002/(SICI)1097-4628(19980919)69:12<2369::AID-APP8>3.0.CO;2-6

Hawileh, R. A., Abu-Obeidah, A., Abdalla, J. A., & Al-Tamimi, A. (2015). Temperature effect on the mechanical properties of carbon, glass and carbon-glass FRP laminates. *Construction and Building Materials*, *75*, 342–348. https://doi.org/10.1016/j.conbuildmat.2014.11.020

Helbling, C., Abanilla, M., Lee, L., & Karbhari, V. M. (2006). Issues of variability and durability under synergistic exposure conditions related to advanced polymer composites in the civil infrastructure. *Composites Part A: Applied Science and Manufacturing*, *37*(8), 1102–1110. https://doi.org/10.1016/j.compositesa.2005.05.039

Hristozov, D., Wroblewski, L., & Sadeghian, P. (2016). Long-term tensile properties of natural fibre-reinforced polymer composites: Comparison of flax and glass fibres. *Composites Part B: Engineering*, *95*, 82–95. https://doi.org/10.1016/j.compositesb.2016.03.079

International Code Council (ICC). (2014). *Acceptance criteria for concrete and reinforced and unreinforced masonry strengthening using externally bonded FRP composite systems, in: ICC AC125, ICC Evaluation Service,* . Whittier, CA.

International Standard Organaziation ISO, & 527-1. (2012). *Plastics Determination of tensile properties – Part 1: General principles*. Geneva, Switzerland.

ISO 10406-1. (n.d.). ISO10406-1,Fibre-reinforcedpolymer(FRP)reinforcement of concrete – Test Methods, Part 1:FRPbarsandgrids,InternationalOrganizationfor Standar-

dization, Switzerland,2008. - Google Search. Retrieved November 6, 2019, from https://www.google.com/search?rlz=1C1CHBF_enIT790IT790&sxsrf=ACYBGNQakLVMuOq-PqPUjbKK-rD5JnLDOA:1573058264301&q=ISO10406-1,Fibre-reinforcedpolymer(FRP)reinforcement+of+concrete+–+Test+Methods,+Part+1:FRPbarsandgrids,InternationalOrganizationfor+Standar-+d

Kabir, M. I., Ph, D., Samali, B., Ph, D., Shrestha, R., & Ph, D. (2016). Fracture Properties of CFRP – Concrete Bond Subjected to Three Environmental Conditions, *20*(4), 1–15. https://doi.org/10.1061/(ASCE)CC.1943-5614.0000665.

Kabir, M. I., Shrestha, R., Samali, B., Ikramul, M., Shrestha, R., & Samali, B. (2016). Effects of applied environmental conditions on the pull-out strengths of CFRP-concrete bond. *Construction and Building Materials*, *114*, 817–830. https://doi.org/10.1016/j.conbuildmat.2016.03.195

Kabir, M., Samali, B., & Shrestha, R. (2016). Fracture Properties of CFRP–Concrete Bond Subjected to Three Environmental Conditions. *Journal of Composites for Construction*, *20*(4), 4016010. https://doi.org/10.1061/(ASCE)CC.1943-5614.0000665

Kafodya, I., Xian, G., & Li, H. (2015). Durability study of pultruded CFRP plates immersed in water and seawater under sustained bending: Water uptake and effects on the mechanical properties. *Composites Part B: Engineering*, *70*, 138–148. https://doi.org/10.1016/j.compositesb.2014.10.034

Karbhari, V. M., Chin, J. W., Hunston, D., Benmokrane, B., Juska, T., Morgan, R., … Reynaud, D. (2003). Durability Gap Analysis for Fiber-Reinforced Polymer Composites in Civil Infrastructure. *Journal of Composites for Construction*, *7*(3), 238–247. https://doi.org/10.1061/(ASCE)1090-0268(2003)7:3(238)

Karbhari, V. M., Rivera, J., & Zhang, J. (2002). Low-temperature hygrothermal degradation of ambient cured E-glass/vinylester composites. *Journal of Applied Polymer Science*, *86*(9), 2255–2260. https://doi.org/10.1002/app.11205

Kong, J. S., & Frangopol, D. M. (2003). Life-Cycle Reliability-Based Maintenance Cost Optimization of Deteriorating Structures with Emphasis on Bridges. *Journal of*

Structural Engineering, *129*(6), 818–828. https://doi.org/10.1061/(asce)0733-9445(2003)129:6(818)

Kouris, L. A. S., & Triantafillou, T. C. (2018). State-of-the-art on strengthening of masonry structures with textile reinforced mortar (TRM). *Construction and Building Materials*, *188*, 1221–1233. https://doi.org/10.1016/j.conbuildmat.2018.08.039

Koutas, L. N., Tetta, Z., Bournas, D. A., & Triantafillou, T. C. (2019). Strengthening of Concrete Structures with Textile Reinforced Mortars: State-of-the-Art Review. *Journal of Composites for Construction*, *23*(1), 1–20. https://doi.org/10.1061/(ASCE)CC.1943-5614.0000882

Lai, W. L., Kou, S. C., Poon, C. S., Tsang, W. F., & Lai, C. C. (2009). Effects of elevated water temperatures on interfacial delaminations, failure modes and shear strength in externally-bonded CFRP-concrete beams using infrared thermography, gray-scale images and direct shear test. *Construction and Building Materials*, *23*(10), 3152–3160. https://doi.org/10.1016/j.conbuildmat.2009.06.012

Leone, M., Matthys, S., & Aiello, M. A. (2009). Effect of elevated service temperature on bond between FRP EBR systems and concrete. *Composites Part B: Engineering*, *40*(1), 85–93. https://doi.org/10.1016/j.compositesb.2008.06.004

Lettieri, M., & Frigione, M. (2012). Effects of humid environment on thermal and mechanical properties of a cold-curing structural epoxy adhesive. *Construction and Building Materials*, *30*, 753–760. https://doi.org/10.1016/j.conbuildmat.2011.12.077

Lin, Y. C., & Chen, X. (2005). Moisture sorption-desorption-resorption characteristics and its effect on the mechanical behavior of the epoxy system. *Polymer*, *46*(25), 11994–12003. https://doi.org/10.1016/j.polymer.2005.10.002

Lomboy, G., International, K. W.-J. of A., & 2009, undefined. (n.d.). Effects of strength, permeability, and air void parameters on freezing-thawing resistance of concrete with and without air entrainment. *Astm.Org*. Retrieved from http://www.astm.org/DIGITAL_LIBRARY/JOURNALS/JAI/PAGES/JAI102454.htm

Lopez de Murphy, M. del M., & Krishnawamy, R. (2006). *Time Performance of*

Concrete-CFRP Bond Under Effects of Freeze-Thaw Cycles and Sustained Loading.

Luque, A., Ruiz-Agudo, E., Cultrone, G., Sebastián, E., & Siegesmund, S. (2011). Direct observation of microcrack development in marble caused by thermal weathering. *Environmental Earth Sciences*, *62*(7), 1375–1386. https://doi.org/10.1007/s12665-010-0624-1

Maljaee, H., Ghiassi, B., & Lourenço, P. B. (2017). Effect of synergistic environmental conditions on thermal properties of a cold curing epoxy resin. *Composites Part B: Engineering*, *113*, 152–163. https://doi.org/10.1016/j.compositesb.2017.01.027

Maljaee, H., Ghiassi, B., Lourenço, P. B., & Oliveira, D. V. (2016). FRP-brick masonry bond degradation under hygrothermal conditions. *Composite Structures*, *147*, 143–154. https://doi.org/10.1016/j.compstruct.2016.03.037

Maxwell, I. D., & Pethrick, R. A. (1983). Dielectric studies of water in epoxy resins. *Journal of Applied Polymer Science*, *28*(7), 2363–2379. https://doi.org/10.1002/app.1983.070280719

Micelli, F., Mazzotta, R., Leone, M., & Aiello, M. A. (2015). Review Study on the Durability of FRP-Confined Concrete. *Journal of Composites for Construction*, *19*(3), 04014056. https://doi.org/10.1061/(ASCE)CC.1943-5614.0000520

Mikami, C., Wu, H. C., & Elarbi, A. (2015). Effect of hot temperature on pull-off strength of FRP bonded concrete. *Construction and Building Materials*, *91*, 180–186. https://doi.org/10.1016/j.conbuildmat.2015.05.013

Nishizaki, I., & Kato, Y. (2011). Durability of the adhesive bond between continuous fibre sheet reinforcements and concrete in an outdoor environment. *Construction and Building Materials*, *25*(2), 515–522. https://doi.org/10.1016/j.conbuildmat.2010.04.067

Nobili, A. (2016). Durability assessment of impregnated Glass Fabric Reinforced Cementitious Matrix (GFRCM) composites in the alkaline and saline environments. *Construction and Building Materials*, *105*, 465–471. https://doi.org/10.1016/j.conbuildmat.2015.12.173

Pekmezci, B. Y., Arabaci, E., & Ustundag, C. (2019). Freeze-Thaw Durability of Lime

Based FRCM Systems for Strengthening Historical Masonry. *Key Engineering Materials*, *817*, 174–181. https://doi.org/10.4028/www.scientific.net/kem.817.174

Pendhari, S. S., Kant, T., & Desai, Y. M. (2008). Application of polymer composites in civil construction: A general review. *Composite Structures*, *84*(2), 114–124. https://doi.org/10.1016/J.COMPSTRUCT.2007.06.007

Ramirez, F. A., Carlsson, L. A., & Acha, B. A. (2008). Evaluation of water degradation of vinylester and epoxy matrix composites by single fiber and composite tests. *Journal of Materials Science*, *43*(15), 5230–5242. https://doi.org/10.1007/s10853-008-2766-z

Robert, M., Wang, P., Cousin, P., & Benmokrane, B. (2010). Temperature as an Accelerating Factor forLong-Term Durability Testing of FRPs:\nShould There Be Any Limitations? *Journal of Composites for Construction*, *14*(4), 361–367. https://doi.org/10.1061//asce/cc.1943-5614.0000102

Roventi, G., Bellezze, T., Giuliani, G., & Conti, C. (2014). Corrosion resistance of galvanized steel reinforcements in carbonated concrete: Effect of wet-dry cycles in tap water and in chloride solution on the passivating layer. *Cement and Concrete Research*, *65*, 76–84. https://doi.org/10.1016/j.cemconres.2014.07.014

Ruregold. (2019a). C-MESH GOLD 84 / 84. *Technical Document*, 1–6. Retrieved from https://www.ruregold.com/

Ruregold. (2019b). PBO-Mesh Gold 70/18 & PBO-MX GOLD MURATURA. *Technical Document*. Retrieved from https://www.ruregold.com/

Saadatmanesh, H., Tavakkolizadeh, M., & Mostofinejad, D. (2010). Environmental effects on mechanical properties of wet lay-up fiber-reinforced polymer. *ACI Materials Journal*, *107*(3), 267.

Santandrea, M., Focacci, F., Mazzotti, C., Ubertini, F., & Carloni, C. (2020). Determination of the interfacial cohesive material law for SRG composites bonded to a masonry substrate. *Engineering Failure Analysis*, *111*, 104322. https://doi.org/10.1016/j.engfailanal.2019.104322

Savvilotidou, M., Vassilopoulos, A. P., Frigione, M., & Keller, T. (2017). Effects of aging in dry environment on physical and mechanical properties of a cold-curing structural

epoxy adhesive for bridge construction. *Construction and Building Materials*, *140*, 552–561. https://doi.org/10.1016/j.conbuildmat.2017.02.063

Scheffler, C., Förster, T., Mäder, E., Heinrich, G., Hempel, S., & Mechtcherine, V. (2009). Aging of alkali-resistant glass and basalt fibers in alkaline solutions: Evaluation of the failure stress by Weibull distribution function. *Journal of Non-Crystalline Solids*, *355*(52–54), 2588–2595. https://doi.org/10.1016/j.jnoncrysol.2009.09.018

Sen, R. (2015). Developments in the durability of FRP-concrete bond. *Construction and Building Materials*, *78*, 112–125. https://doi.org/10.1016/j.conbuildmat.2014.12.106

Serbescu, A., Guadagnini, M., & Pilakoutas, K. (2013). Standardised double-shear test for determining bond of FRP to concrete and corresponding model development. *Composites Part B: Engineering*, *55*, 277–297. https://doi.org/10.1016/j.compositesb.2013.06.019

Sethi, S., & Ray, B. C. (2015). Environmental effects on fibre reinforced polymeric composites: Evolving reasons and remarks on interfacial strength and stability. *Advances in Colloid and Interface Science*, *217*, 43–67. https://doi.org/10.1016/j.cis.2014.12.005

Shrestha, J., Ueda, T., & Zhang, D. (2015). Durability of FRP Concrete Bonds and Its Constituent Properties under the Influence of Moisture Conditions. *Journal of Materials in Civil Engineering*, *27*(2), A4014009. https://doi.org/10.1061/(asce)mt.1943-5533.0001093

Sika. (2017a). Sikadur®-330. *Technical Document*, 2–5. Retrieved from https://ita.sika.com/it/edilizia/rinforzi-e-incollaggistrutturali/strutture-in-calcestruzzo/incollaggio-strutturaleeiniezioni/sikadur-330.html

Sika. (2017b). SikaWrap ® -300 C. *Technical Document*, 1–4. Retrieved from https://ita.sika.com/it/edilizia/rinforzi-e-incollaggistrutturali/strutture-in-calcestruzzo/tessuti-in-carbonio/sikawrap-300-c.html

Sika. (2019). Sika MonoTop ® -722 Mur. *Technical Document*, 1–4. Retrieved from https://ita.sika.com/it/edilizia/rinforzi-e-incollaggistrutturali/sistemi-antisfondellamentopersolai/sika-monotop-722mur.html

Silva, M. A. G., & Biscaia, H. (2008). Degradation of bond between FRP and RC beams. *Composite Structures*, *85*(2), 164–174. https://doi.org/10.1016/j.compstruct.2007.10.014

Silva, P., Fernandes, P., Sena-Cruz, J., Xavier, J., Castro, F., Soares, D., & Carneiro, V. (2016). Effects of different environmental conditions on the mechanical characteristics of a structural epoxy. *Composites Part B: Engineering*, *88*, 55–63. https://doi.org/10.1016/j.compositesb.2015.10.036

Sneed, L. H., D'Antino, T., & Carloni, C. (2014). Investigation of bond behavior of polyparaphenylene benzobisoxazole fiber-reinforced cementitious matrix composite-concrete interface. *ACI Materials Journal, 111*(5), 569–580. https://doi.org/10.14359/51686604

Soles, C. L., & Yee, A. F. (2000). Discussion of the molecular mechanisms of moisture transport in epoxy resins. *Journal of Polymer Science, Part B: Polymer Physics*, *38*(5), 792–802. https://doi.org/10.1002/(SICI)1099-0488(20000301)38:5<792::AID-POLB16>3.0.CO;2-H

Stefania, S. M., Mariaenrica, F., & Antonietta, A. M. (2010). Wet Lay-Up Manufactured FRPs for Concrete and Masonry Repair: Influence of Water on the Properties of Composites and on Their Epoxy Components. *Journal of Composites for Construction*, *14*(6), 823–833. https://doi.org/10.1061/(ASCE)CC.1943-5614.0000132

Sun, W., Zhang, Y. M., Yan, H. D., & Mu, R. (1999). Damage and damage resistance of high strength concrete under the action of load and freeze-thaw cycles. *Cement and Concrete Research*, *29*(9), 1519–1523. https://doi.org/10.1016/S0008-8846(99)00097-6

Täljsten, B., Journal, I., Publishers, K. A., Engineering, S., & Engineering, C. (1996). Strengthening of concrete prisms using the plate-bonding technique. *International Journal of Fracture*, *82*(3), 253–266. https://doi.org/10.1007/BF00013161

Tao, Y., & Chen, J. F. (2014). Concrete Damage Plasticity Model for Modeling FRP-to-Concrete Bond Behavior. *Journal of Composites for Construction*, *19*(1), 04014026.

https://doi.org/10.1061/(asce)cc.1943-5614.0000482

Tatar, J, Weston, C., Blackburn, P., & Hamilton, H. R. (2013). Direct Shear Adhesive Bond Test, 1–10.

Tatar, Jovan, & Hamilton, H. R. (2016). Comparison of laboratory and field environmental conditioning on FRP-concrete bond durability. *Construction and Building Materials*, *122*, 525–536. https://doi.org/10.1016/j.conbuildmat.2016.06.074

TCS. (2020a). B-STRUCTURA. *Technical Document*, (January). Retrieved from https://www.tcscalce.it/en/prodotto/b-structura

TCS. (2020b). Steel X800-A4. *Technical Document*, (July), 1–3. Retrieved from https://www.tcscalce.it/en/prodotto/tcs-steel-x800-a4

Teng, J. G., Zhang, S. S., Dai, J. G., & Chen, J. F. (2013). Three-dimensional meso-scale finite element modeling of bonded joints between a near-surface mounted FRP strip and concrete. *Computers and Structures*, *117*, 105–117. https://doi.org/10.1016/j.compstruc.2012.12.002

Terreal Italia San Marco. (2018). Vivo Red Bricks. *Technical Documents*. Retrieved from https://www.sanmarco.it/scheda-prodotto.php?id-categoria=2&id-prodotto=36

Tuakta, C., & Büyüköztürk, O. (2011). Deterioration of FRP/concrete bond system under variable moisture conditions quantified by fracture mechanics. *Composites Part B: Engineering*, *42*(2), 145–154. https://doi.org/10.1016/j.compositesb.2010.11.002

Uomoto, T., Mutsuyoshi, H., Katsuki, F., & Misra, S. (2002). Use of fiber reinforced polymer composites as reinforcing material for concrete. *Journal of Materials in Civil Engineering*, *14*(3), 191–209. https://doi.org/10.1061/(ASCE)0899-1561(2002)14:3(191)

VanLandingham, M. R., Eduljee, R. F., & Gillespie, J. W. (1999). Moisture Diffusion in Epoxy Systems. *Journal of Applied Polymer Science*, *71*(5), 787–798. https://doi.org/10.1002/(SICI)1097-4628(19990131)71:5<787::AID-APP12>3.0.CO;2-A

Williams Portal, N., Flansbjer, M., Johannesson, P., Malaga, K., & Lundgren, K. (2016).

Tensile behaviour of textile reinforcement under accelerated ageing conditions. *Journal of Building Engineering*, *5*, 57–66. https://doi.org/10.1016/j.jobe.2015.11.006

Woo, M. S. W., & Piggott, M. R. (1987). WATER ABSORPTION OF RESINS AND COMPOSITES: II. DIFFUSION IN CARBON AND GLASS REINFORCED EPOXIES. *Journal of Composites Technology and Research*, *9*(4), 162–166.

Wu, Z., Yuan, H., Niu, H., Zhishen, W., Hong, Y., & Hedong, N. (2002). Stress transfer and fracture propagation in different kinds of adhesive joints. *Journal of Engineering Mechanics*, *128*(5), 562–573. https://doi.org/10.1061/(ASCE)0733-9399(2002)128:5(562)

Yadav, A. P., Nishikata, A., & Tsuru, T. (2004). Degradation mechanism of galvanized steel in wet-dry cyclic environment containing chloride ions. *Corrosion Science*, *46*(2), 361–376. https://doi.org/10.1016/S0010-938X(03)00153-7

Yalim, B., Kalayci, A. S., & Mirmiran, A. (2008). Performance of FRP-strengthened RC beams with different concrete surface profiles. *Journal of Composites for Construction*, *12*(6), 626–634. https://doi.org/10.1061/(ASCE)1090-0268(2008)12:6(626)

Yang, Q., Xian, G., & Karbhari, V. M. (2008). Hygrothermal ageing of an epoxy adhesive used in FRP strengthening of concrete. *Journal of Applied Polymer Science*, *107*(4), 2607–2617. https://doi.org/10.1002/app.27287

Yin, S., Jing, L., Yin, M., & Wang, B. (2019). Mechanical properties of textile reinforced concrete under chloride wet-dry and freeze-thaw cycle environments. *Cement and Concrete Composites*, *96*(November 2018), 118–127. https://doi.org/10.1016/j.cemconcomp.2018.11.020

Yuan, H., Teng, J. G., Seracino, R., Wu, Z. S., & Yao, J. (2004). Full-range behavior of FRP-to-concrete bonded joints. *Engineering Structures*, *26*(5), 553–565. https://doi.org/10.1016/j.engstruct.2003.11.006

Zhou, A., Büyüköztürk, O., & Lau, D. (2017). Debonding of concrete-epoxy interface under the coupled effect of moisture and sustained load. *Cement and Concrete*

Composites, *80*, 287–297. https://doi.org/10.1016/j.cemconcomp.2017.03.019

Zhou, J., & Lucas, J. P. (1999a). Hygrothermal effects of epoxy resin. Part I: The nature of water in epoxy. *Polymer*, *40*(20), 5505–5512. https://doi.org/10.1016/S0032-3861(98)00790-3

Zhou, J., & Lucas, J. P. (1999b). Hygrothermal effects of epoxy resin. Part II: Variations of glass transition temperature. *Polymer*, *40*(20), 5513–5522. https://doi.org/10.1016/S0032-3861(98)00791-5